University of Alabama at Birmingham
UAB Digital Commons

All ETDs from UAB | UAB Theses & Dissertations

2023

# Renal Proximal Tubule Tissue Chips for Disease Modeling and Drug Toxicity Testing

Leslie Donoghue
*University of Alabama at Birmingham*

Follow this and additional works at: https://digitalcommons.library.uab.edu/etd-collection

 Part of the Engineering Commons

## Recommended Citation

Donoghue, Leslie, "Renal Proximal Tubule Tissue Chips for Disease Modeling and Drug Toxicity Testing" (2023). *All ETDs from UAB*. 41.
https://digitalcommons.library.uab.edu/etd-collection/41

This content has been accepted for inclusion by an authorized administrator of the UAB Digital Commons, and is provided as a free open access item. All inquiries regarding this item or the UAB Digital Commons should be directed to the UAB Libraries Office of Scholarly Communication.

# RENAL PROXIMAL TUBULE TISSUE CHIPS FOR DISEASE MODELING AND DRUG TOXICITY TESTING

by

LESLIE DONOGHUE

PALANIAPPAN SETHU, COMMITTEE CHAIR
TIMMY LEE
MARGARET LIU
JENNIFER POLLOCK
MARY KATHRYN SEWELL-LOFTIN

A DISSERTATION

Submitted to the graduate faculty of The University of Alabama at Birmingham,
in partial fulfillment of the requirements for the degree of
Doctor of Philosophy

BIRMINGHAM, ALABAMA

2023

RENAL PROXIMAL TUBULE TISSUE CHIPS FOR DISEASE MODELING AND DRUG TOXICITY TESTING

LESLIE DONOGHUE

BIOMEDICAL ENGINEERING

## ABSTRACT

The current pathway for drug discovery is associated with costs of $2.55 billion and between 10-15 years of development for a single drug to reach the market. The challenges in predicting drug toxicities and efficacies are attributed to inherent species differences in drug-metabolizing enzyme activities and cell-type-specific sensitivities to toxicants. Organs-on-a-chip are an emerging technology in disease modeling and screening therapeutics to address discrepancies between animal models and human clinical trials. They utilize tissue engineering, fluid mechanics, and biomaterials to replicate in vivo architectures and functions of complex organs and tissues. Herein, the effect of pressure and stretch on bioengineered cardiac tissue and a spectrum fluidic shear stress on the renal proximal tubule epithelium are evaluated to elucidate how these stimuli play an important role in maintaining cellular phenotype and homeostasis. Additionally, human renal proximal tubule cells were cultured under physiological shear and pressure with known nephrotoxic or non-nephrotoxic compounds. Lastly, a more complex and novel bioengineered platform was developed of a 3D PT tubule and associated vascular networks. The organ-on-a-chips developed in this study will provide a technology that has broad applications in basic and translational research to model disease states, study interactions with other tissue chips, and accurately predict drug toxicity.

Keywords: tissue engineering, cardiac remodeling, proximal tubule, nephrotoxicity

# DEDICATION

*To my husband, parents, sister, grandparents, in-laws, friends, and mentors, this work is as much yours as it is mine.*

ACKNOWLEDGEMENTS

I would first like to thank my graduate mentor and committee chair, Dr. Palaniappan Sethu, for the years of mentorship and guidance you have provided me. You are incredibly kind and patient and trusted me to navigate research projects new to the lab's portfolio. Since day one, your vibrant enthusiasm and optimism have balanced my innate skepticism. In a way, the lab that I joined in January 2018 is drastically different than it is today. From exponentially growing in the number of personnel, from the physical move that was many years in the making, and your success of research funding that is incredibly deserving—all were navigated through your leadership, endless creativity, and inherent ability to mentor students.

In the same sentiment, I would like to thank all Sethu lab members, especially my undergraduate mentees: Arushi Kotru, Emma Stevenson, Alfredo Guzman, and Chase Newton, among others. I sincerely enjoyed being a part of your research growth and assisting me when the work became too much on my own. Through each of you, I excavated just a strong passion for mentorship. As I move forward with my career of mentoring others, I will always appreciate and look back at these graduate years spent with you all.

Arushi, little did I know that a recent high-school graduate joining the lab for the summer (and someone many years my junior) would become genuinely one of my closest friends. You were always there for me when an experiment failed, we had a repetitive

PDMS and device manufacturing day, or when more work was supposed to be done, but our endless conversations got in the way. My graduate school experience is intrinsically tied to my time and friendship with you—and I would not have it any other way.

To Khanh Nguyen, Caleb Graham, and Ian Berg—I want to thank you for putting up with my goofy humor and always supporting me professionally and personally. We have all learned so much these last few years, and the challenges were always navigated with each of you by my side.

I want to thank my committee for playing such a distinct role in this dissertation and my professional growth. To Dr. Jennifer Pollock, thank you for taking a chance on me—a chemical engineering graduate with minuscule experience with kidney physiology. That chance has changed my career trajectory in many ways, and I can attribute it to both you and Dr. Sethu. Since starting graduate school, I have always looked up to you. Through the T32 and kidney summer programs, the opportunities and mentorship you have provided to hundreds of students now are one of the most admirable elements a researcher can provide. I am thankful to be among one of them. Dr. Timmy Lee, your lab, and its trainees provided me with a second lab home. As I progressed in my training, I required a greater understanding and experience with many biomolecular assays. You, Maheshika Somarathna, and Tatyana Isayeva provided tremendous guidance and strengthened my skillset as a researcher in these areas. To my University of Alabama-related committee members, Dr. Margaret Liu and Dr. MK Sewell-Loftin, I am thankful to have committee members that have shared experiences and always helped me to get to the next stage. Dr. Liu, I have known you for about ten years, and you are still one of the nicest people I have ever met. Additionally, your story of being in the industry but coming back to academia is something

I related to, and it offered just a tremendous insight that not all researchers possess. Dr. MK Sewell-Loftin, since the day you joined the UAB BME department, the parallel of your research interests offered such a welcoming and collaborative atmosphere that was previously absent (despite being in a pandemic). Your perspective on the engineering aspects of my projects always came with a deep understanding of the difficulties experienced when creating organs-on-a-chip.

To my biomedical engineering, cardiovascular disease, and nephrology departments, thank you for enriching my experience and each offering opportunities for growth. From the administrative staff, leadership, and fellow trainees, I am lucky to have worked with you all.

To my Donoghue and Seeley family members, I cannot thank you enough for your support and for getting me to where I am today. And lastly, to my husband, Ryan Seeley, thank you for being the biggest supporter during my time at graduate school and beyond. We will always remember these years of training for the intense hustle. But I hope it can remind us that we just need each other and a passion for learning to have a life full of joy and laughter and meaningful careers. As our aspirations and careers grow, I am lucky to be growing by your side. I love you very much.

To everyone mentioned previously and beyond— the best years of my life are congruent with my time at UAB. I wholeheartedly cherish the relationships I have developed personally and professionally. Since I have been a student here, I had two surgeries, four apartment moves, an engagement, a wedding, and lived through pandemic. But through it all and at this university, I have found lifelong mentors that are always eager to help and collaborate and I will always be appreciative to have received my training here.

TABLE OF CONTENTS

*Page*

ABSTRACT ..... ii

DEDICATION ..... iii

ACKNOWLEDGMENTS ..... iv

LIST OF TABLES ..... xi

LIST OF FIGURES ..... xii

CHAPTER 1: TISSUE CHIPS AND MICROPHYSIOLOGICAL SYSTEMS FOR DISEASE MODELING AND DRUG TESTING ..... 1

Introduction ..... 3
Cardiac Tissue Chips ..... 9
Function ..... 9
Cell Types and Extracellular Matrix ..... 10
Cellular Organization ..... 10
Physical Stresses, Fluid Flow, and Electrical Signals ..... 10
Examples of Cardiac Tissue Chips ..... 11
Limitations ..... 21

Kidney Tissue Chips ..... 21
Function ..... 21
Cell Types and Extracellular Matrix ..... 22
Cellular Organization ..... 22
Physical Stresses, Fluid Flow ..... 23
Examples of Kidney Tissue Chips ..... 24
Limitations ..... 30

Microphysiological Systems ..... 31

Challenges Associated with the Design and Construction of Microphysiological Systems ..... 35
Communication ..... 35
Nondestructive Monitoring ..... 38

Material Selection and Fabrication of TCs and MPS ..... 39
Summary…..... 40
Reference…..... 41

CHAPTER 2: ACUTE RESPONSE OF ENGINEERED CARDIAC TISSUE TO PRESSURE AND STRETCH..... 49

Introduction ..... 52
Material and Methods..... 53
Cardiac Cell Culture Chamber Fabrication ..... 53
Cell Culture and Collagen I-Matrigel Hydrogel Encapsulation ..... 55
Hemodynamic Experimental Setup ..... 56
Histology and Immunohistochemistry..... 58
RT-qPCR ..... 58
Soluble Factor Analysis..... 59
Statistical Analysis ..... 60
Results…… ..... 60
Generation of Decoupled Pressure and Stretch ..... 60
Tissue Morphology and Organization ..... 60
Gene Expression Profiling..... 63
Soluble Factor Analysis..... 65
Discussion…..... 67
Conclusion..... 70
Reference…..... 71

CHAPTER 3: PROINFLAMMATORY AND PROFIBROTIC PROFILES OF HUMAN RENAL PROXIMAL EPITHELIAL CELLS IN RESPONSE TO DRUGS AND FLUIDIC SHEAR STRESS..... 72

Specific Aim 1 ..... 73
Abstract..... 74
Introduction ..... 76
Material and Methods..... 78
Planar Proximal Tubule Device Fabrication ..... 78
Cell Culture and Collagen-IV..... 79
Perfusion Experimental Setup ..... 80
Computational Fluid Dynamics..... 81
Immunofluorescence ..... 81
RNA Isolation and Sample Preparation for Nanostring ..... 82
ROSALIND® Nanostring Gene Expression Methods..... 83
Principal Component Analysis ..... 84
Drug Nephrotoxicity Concentrations and Lactase Dehydrogenase Cytotoxicity Analyses..... 84
Transepithelial Electrical Resistance..... 85
NGAL ELISA..... 86
Soluble Factor Analysis..... 87

Statistical Analysis ..... 87
Results…… ..... 88
Device Design and Perfusion Parameters to Evaluate Shear Stresses to hRPTEC-hTERT1 Cells ..... 88
Fluid Flow Promotes Expression of Functional and Structural Markers of hRPTEC-hTERT1s when Compared to Culture in Static Conditions ..... 90
Nanostring and Principal Component Analysis Show Distinct Gene Expression Profiles Between Static, Low Shear, and High Shear Conditions ..... 92
Nephrotoxic and Non-Nephrotoxic Drugs and hRPTEC-hTERT1 Soluble Factor Analysis ..... 97
Additional Findings: In vitro Human Proximal Tubule Cells in Static Culture Experience Up-Regulation of Mediators in the Fibrotic Pathway ..... 109
Discussion and Conclusions ..... 111
Reference…... ..... 116

CHAPTER 4: NOVEL HUMAN RENAL PROXIMAL TUBULE TISSUE CHIPS CONTAINING 3D TUBULES WITH SURROUNDING PERITUBULAR MICROVASCULAR NETWORKS ..... 120

Specific Aim 2 ..... 121
Introduction ..... 122
Material and Methods ..... 124
Cell Culture ..... 124
Plasmid Construction and Validation ..... 125
Generation of Fluorescence and Stable Cell Lines ..... 128
Computer-Aided-Design (CAD) for 3D Renal Proximal Tubule Tissue Chip ..... 129
Computational Fluid Dynamics ..... 129
3D Printed SLA Devices and Post-Processing ..... 130
Microvascular Fibrinogen-Gelatin Hydrogel ..... 131
Perfusion Experimental Setup ..... 133
Proximal Tubule Seeding ..... 134
Confocal Microscopy ..... 135
Results…… ..... 135
Generation of Stable Cell Lines for Utilization in Tissue-Engineered Peritubular Microvascular Networks ..... 135
Engineering Technologies to Generate Human Renal Proximal Tubule Tissue Chips ..... 137
Protocol and Timeline Considerations to Co-Culture hRPTEC-hTERT, hMEC-1, and hDFs in Gelatin-Fibrin Hydrogel ..... 139
Imaging Studies of Human Renal Proximal Tubule Tissue Chips Indicate Microvascular Networks and Confluent Lumens ..... 140
Discussion and Conclusions ..... 143

Reference…... 148

CHAPTER 5: CONCLUSIONS, FUTURE DIRECTIONS, & PUBLIC HEALTH RELEVANCE ..... 149

Greater Public Health Relevance ..... 150
Impact of Organs-on-a-Chip on Legislation: Modernization Act 2.0… ..... 150
Impact of Organs-on-a-Chip and Mechanobiology: Pharmaceutical Perspectives ..... 152
Future Directions ..... 156
Acute Response of Engineered Cardiac Tissue to Pressure and Stretch ..... 156
Shear Stress 2D Renal Proximal Tubule Tissue Chip ..... 157
3D Renal Proximal Tubule Tissue Chip with Associated Microvascular ..... 159
Discussion and Conclusions ..... 161
Reference…... 162

LIST OF TABLES

*Table* *Page*

CHAPTER 1

1 Microphysiological Systems ..... 34

CHAPTER 2

1 Parameters for Experimental Setups..... 60

LIST OF FIGURES

*Figures* *Page*

CHAPTER 1

1 Schematic of Modular Microphysiological system ..... 7

2 Cardiac Tissue Chips ..... 14

3 Renal Tissue Chips ..... 27

CHAPTER 2

1 Overview of 3D Cardiac Tissue Chips ..... 56

2 Immunofluorescence Microscopy of Engineered Constructs Following Static, Pressure, or Stretch Stimuli for 24 hours ..... 61

3 Tissue Morphology and Alignment ..... 63

4 Molecular Characterization of Engineered Cardiac Tissues ..... 64

5 Soluble Factor Analysis ..... 66

CHAPTER 3

1 Device Design and Perfusion Parameters ..... 89

2 Immunofluorescence Microscopy of hRPTEC-hTERT1s Grown in Either Static or Dynamic Physiological Shear Stress Conditions ..... 91

3 Meta-Analysis Using ROSALIND Software to Investigate 758 Genes Detected in Nanostring Data Comparing Static, Low, Shear, and High Shear Conditions ..... 93

4 Principal Component Analysis of Nanostring Gene Expression

Comparing Static, Low Shear, and High Shear Conditions ..... 94

5 In Vitro Culture of hRPTEC-hTERT1 with Nephrotoxic Drug Cisplatin Non-Nephrotoxic Drugs Probenecid Using Static LDH Assay at Varying Drug Concentrations, TEER Using Transwell Plates, and LDH Following 48 Hours of Perfusion ..... 96

6 LDH Relative Absorbance was Measured After Perfusion Without Drugs and With Probenecid, Dexamethasone, or Probenecid ..... 97

7 Chemokine CC Family Cytokine Production and Gene Expression ..... 99

8 Chemokine CXC Family Cytokine Production and Gene Expression ..... 100

9 Colony Stimulating Factor (CSF) Family Cytokine Production and Gene Expression ..... 101

10 Tumor Necrosis Factor (TNF) Family Cytokine Production and Gene Expression ..... 102

11 Interferon (IFN) Family Cytokine Production and Gene Expression..... 104

12 Interleukin (IL) Family Cytokine Production and Gene Expression..... 106

13 Growth Factor (GF) Family Cytokine Production and Gene Expression ..... 108

14 Epithelial-to-Mesenchymal Transition and Proximal Tubule Fibrosis-Related Transcription Factors Upregulated in Static Conditions ..... 110

CHAPTER 4

1 Overview of the process and validation of Stable Cell Lines Generated for Tissue Engineered Peritubular Microvascular Networks ..... 137

2 Computer-Aided Design (CAD), 3D Printing Technologies, and Computational Fluid Dynamics (CFD) modeling software to Generate Human Renal Proximal Tubule Chips ..... 138

3 Workflow to encapsulate hRPTEC-hTERT, hMEC-1, and hDFs in Gelatin-Fibrin Hydrogel ..... 140

4 Visualizations of microvascular peritubular networks consisting of Co-Culture of hRPTEC-hTERT-EGFP, hMET-1, and hDFs in Gelatin-Fibrin Hydrogel ..... 142

5 hRPTEC-hTERTs Forming Confluent Tubules after Five Days of Fluidic Shear Stress ..... 143

CHAPTER 5

1 Pictorial representation of the key aspects of the roadmap ..... 154

2 Illustration of the Purpose of Early Drug Development Phases and How the Context of the Use of a Tissue Chip Will Vary Depending upon the Phase in Which it is Intended to be Used ..... 155

# CHAPTER 1

# TISSUE CHIPS AND MICROPHYSIOLOGICAL SYSTEMS FOR DISEASE MODELING AND DRUG TESTING

by

LESLIE DONOGHUE, KHANH T. NGUYEN, CALEB GRAHAM, AND PALANIAPPAN SETHU

*Micromachines, 12(2), 139.* https://doi.org/10.3390/mi12020139
Copyright
2021
by
MDPI
Used by permission

Format adapted for dissertation

## Highlights

- Tissue chips and microphysiological system to screen drugs and model disease are relatively new bioengineering technologies (< 25 years old) that incorporate human cells organized in tissue type specific architectures and biomechanical forces to more accurately represent tissues in the body.
- Design considerations vary based on the type of tissue or organ that will be modeled and the intended research question (i.e. toxicity, pathophysiology model, cell to cell interaction, etc.).
- This chapter highlights cardiac and renal tissue chips and microphysiological systems focusing on recent advancements and current limitations.
- Cardiac tissue chip models require the use of stem cell derived cardiomyocytes to overcome limitations associated with non-proliferating adult cardiomyocyte and the inclusion of hemodynamic and electrical stimuli associated with heart function.
- Renal tissue chips are relatively new (< 10 years), as there are significant complexities associated with integrating the vast number of cell types and specific transport mechanisms to accurately model various functions of the kidneys.

Abstract

Tissue chips (TCs) and microphysiological systems (MPSs) that incorporate human cells are novel platforms to model disease and screen drugs and provide an alternative to traditional animal studies. This chapter highlights the basic definitions of TCs and MPSs, examines two major organs/tissues, identifies critical parameters for organization and function (tissue organization, blood flow, and physical stresses), reviews current microfluidic approaches to recreate tissues, and discusses current shortcomings and future directions for the development and application of these technologies. The renal and cardiovascular systems are emphasized as they are involved in the metabolism or excretion of drugs and are sensitive to drug toxicity. Furthermore, the review discusses microfluidic/microfabrication approaches and identifies specific examples of TCs. Together, they will provide a starting point for understanding, designing, and constructing novel TCs for possible integration within MPS; and highlight their broader implications in existing drug discovery and disease modeling fields.

## 1. Introduction

For decades, our understanding of essential cellular functions and how they relate to human health has relied on model systems investigating the molecular basis of normal physiology and pathophysiology. Cellular-level models provide a high degree of biological specificity that permits the study of specific cellular signaling pathways without noise or crosstalk due to interactions among other tissues and organs. However, the physiological relevance of cellular-level models could be higher, as they fail to recreate the systemic interactions seen in whole organisms. For this reason, while identifying therapeutic targets

typically begins at the cellular level, drugs require subsequent pre-clinical validation in higher-level animal models before progressing to human studies. The cost and time of obtaining regulatory approval following pre-clinical studies and clinical trials for a single drug are upwards of USD 2.55 billion and between 10–15 years, respectively [1-3]. A significant contributor to this expensive and time-consuming drug discovery pathway is the reliance on animal models, which often are not accurate predictors of the efficacy and toxicity of drugs in humans. Nearly 30% of drugs deemed safe in animal studies are toxic to humans, and around 60% of drugs that are effective in animals provide no discernible benefit to humans [4]. These discrepancies are due, in large part, to interspecies differences in the activities of drug-metabolizing enzymes. Thus, there is a critical need for alternatives to animal models that closely replicate human physiology to predict candidate therapeutics' efficacy, safety, bioavailability, and toxicity.

A potential solution for increasing the predictive power of pre-clinical studies is using in vitro model systems constructed with human cells. However, such model systems' clinical relevance relies on their ability to mimic human physiology and function accurately. Breakthroughs in developmental and stem cell biology have resulted in the availability of human induced pluripotent stem cells (hiPSCs), representing the renewable and patient-specific source of cells for constructing complex, multicellular in vitro models. Recent advancements in tissue engineering, biomaterial science, three-dimensional (3D) fabrication techniques, and microfluidic technologies have enabled new methods for creating 3D tissue constructs or tissue chips (TCs). TCs, also frequently referred to as organ chips (OCs), replicate essential aspects of human organ structure and function, and their development has received strong support from federal funding agencies. In 2010, the

National Institutes of Health (NIH) Common Fund, in collaboration with the Food and Drug Administration (FDA), started the Regulatory Science Program to make medical product development and evaluation more efficient. The first TC project, which sought to develop a heart-lung model to test the safety and efficacy of drugs, was funded as part of this program [4]. This initiative was further strengthened via additional collaborations with the Defense Advanced Research Projects Agency (DARPA), leading to a coordinated effort to launch the “Tissue Chips for Drug Screening” program in 2012. More recently, their application has broadened to a multitude of disciplines. Researchers have since developed microphysiological systems (MPSs), also known as multi-organ tissue chips (MOTCs), established Tissue Chip Testing Centers to validate their efficacy for disease modeling, and have sent TCs to the International Space Station U.S. National Laboratory to study the effects of microgravity on human cells [5]. (To avoid confusion, the terms "tissue chips" and "microphysiological systems" will be used exclusively throughout the rest of this review, except in cases where the original authors used the alternate terminology.)

With TCs and MPSs (Figure 1) poised to become integral components of the drug discovery and regulatory process, the working definitions of the terms "tissue chips" and "microphysiological systems" need to be established. "Tissue chips" can be defined as “engineered in vitro devices that can be used to model both structure and function of working units in the body, including organs such as the brain, heart, lungs, liver, gut, pancreas, and kidneys and tissues such as skeletal muscle, adipose tissue, and bone.” Typically, such models utilize cells (preferably of human origin, to avoid interspecies differences), extracellular matrix (ECM), and biomaterials to fabricate 3D multicellular

constructs in environments where cellular interactions (cell–cell, cell–ECM), biomechanical stresses (shear, pressure, stretch), bioelectrical signals, and soluble factor signaling (certain hormones, growth factors, cytokines) are all replicated to model in vivo-like responses accurately. "Microphysiological systems" can be defined as “engineered multi-tissue/organ systems constructed using two or more tissue chips or by incorporating multiple interconnected “tissue”/”organ” chambers on one chip to recreate communications among different tissues, organs, and/or organ systems to model systemic interactions in the context of normal physiology, disease, or testing of candidate therapeutics.” Communication among “tissues” or “organs” incorporated in MPSs can be established through multiple approaches, depending upon the specific relationships of interest. For instance, aspects of the cardiovascular system can be recapitulated by employing flexible tubing (if connecting multiple TCs) or microfluidic channels (if all “tissues” or “organs” are housed on one chip) in combination with pumps to provide for the perfusion of media among different chambers, thus allowing soluble factor signaling to take place as it would in vivo. Additional or alternative modes of communication can be enabled by incorporating aspects of the nervous, immune, endocrine, and lymphatic systems.

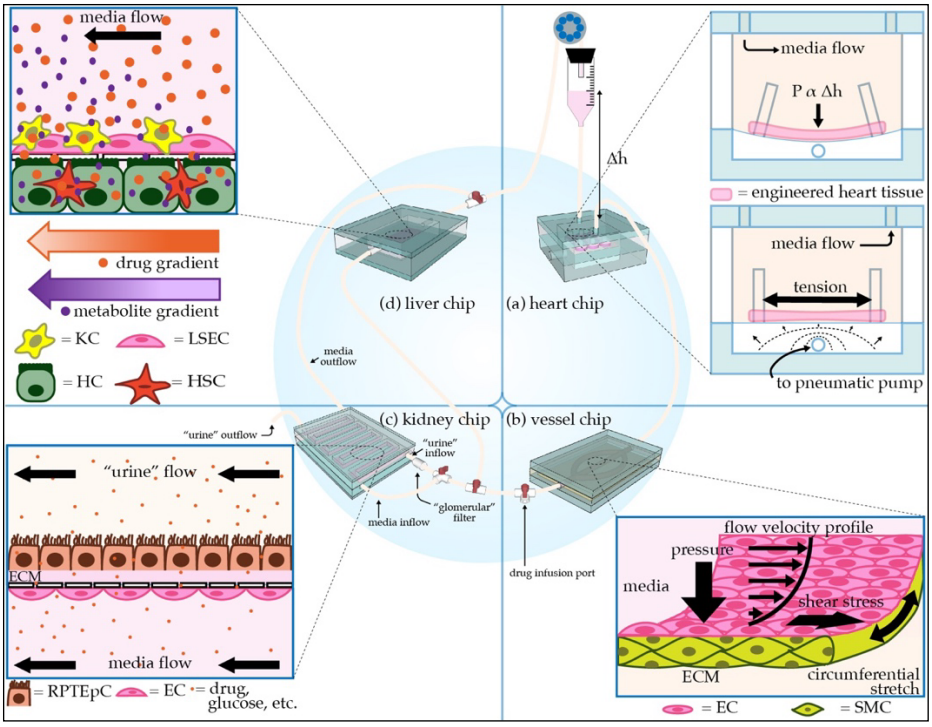


**Figure 1. Schematic of Modular Microphysiological System.** (a) Three-dimensional heart chip with cardiomyocytes (CMs) and stromal cells suspended in hydrogel between posts. The chip mimics the pressure-volume changes seen in the left ventricle. The "diastolic filling pressure," which is directly proportional to the fluid reservoir's height, pushes the flexible polydimethylsiloxane (PDMS) membrane downward, stretching the cardiac fiber. A pneumatic pump then generates "systolic pressure" in the lower air-filled chamber, returning the membrane and cardiac fiber to the baseline stretch. (b) Perfusable 3D vessel chip with microvessels composed of endothelial cells (ECs) and smooth muscle cells (SMCs) surrounded by an extracellular matrix (ECM), with key tunable parameters indicated. (c) Three-dimensional kidney chip mimicking the proximal tubule and adjacent peritubular capillary. To mimic the proximal tubule, renal proximal tubule epithelial cells (RPTEpCs) are cultured upon a bed of ECM. RPTEpCs have a prominent brush border, as they would in vivo. The underlying porous membrane recapitulates the selective barrier

function of the tubule wall. In addition to the upstream drug infusion port, there is a valve allowing for media to bypass the kidney chip, as well as a valve splitting the kidney chip media inflow. One inflow branch passes through a "glomerular" filter and enters the proximal tubule chamber as "urine." The remaining unfiltered media flows into the bottom vascular chamber, the superior aspect of which is lined with ECs. Other applications of this chip include modeling transport phenomena related to drugs or other key molecules. (d) Liver chip with liver sinusoidal endothelial cells (LSECs) and Kupffer cells (KCs) lining the "sinusoid," a porous membrane mimicking the perisinusoidal space, and hepatocytes (HCs) and hepatic stellate cells (HSCs) cultured below the membrane. HCs have microvilli projecting towards the "perisinusoidal space," as they would in vivo.

Both TCs and MPSs represent miniaturized versions of the human body and require microscale bioengineering technologies to organize cells into "tissues" and facilitate fluid flow. Therefore, microfabrication techniques and microfluidic technologies play an essential role in constructing and operating TCs and MPSs. Each tissue type requires efficient design consideration to enable proper functionality. Design parameters include tissue architecture (cell types and organization, ECM composition), blood flow (oxygen and nutrient delivery, waste removal), and physical stresses (shear, pressure, stretch) associated with the target organ/tissue. This chapter provides a basic understanding of the tissue-level organization and function of four critical organs involved in metabolizing or excreting drugs (liver and kidney) or are frequently damaged by off-target drug toxicity (heart and blood vessels). Essential design considerations in developing TC models of each organ/tissue are examined, and current efforts and past successes in TC models' development are summarized. While this chapter focuses on the heart and kidneys, more

information on other organ systems can be found in the following excellent articles focused on the liver and vasculature (the original publication of this chapter), brain [6], lungs [7], GI system [8], pancreas [9], and reproductive system [10]. The following review articles also provide comprehensive overviews of TCs and their use in the drug testing [11, 12] and disease modeling [13].

## 2. Cardiac Tissue Chips

### *2.1. Function*

The heart is a complex organ that pumps blood throughout the body and comprises four chambers: the right atrium, right ventricle, left atrium and left ventricle. The atria are thin-walled cavities that receive blood from large veins (the vena cavae on the right and the pulmonary veins on the left) and act as reservoirs for the ventricles, the muscular chambers that abut the atria and contract after filling to propel blood forward [14]. The heart can be considered as two pumps that work in synchrony, with the right side of the heart involved in pumping deoxygenated blood from the systemic circulation into the lungs for oxygenation and release of carbon dioxide and the left side of the heart receiving that oxygen-rich blood and pumping it forward to the rest of the body. Cardiomyocytes (CMs) contain actin, myosin, and other contractile proteins organized into sarcomeres, which contract and relax under the influence of ion gradients and membrane potentials [15]. While the primary function of the heart is to pump blood, atrial CMs also produce atrial natriuretic peptide (ANP), and ventricular CMs produce brain natriuretic peptide (BNP), hormones that both play roles in normal homeostasis of blood pressure and extracellular fluid volume [16].

### *2.2. Cell Types and Extracellular Matrix*

Cardiac tissue is composed of many cell types, with the most abundant being CMs, fibroblasts (FBs), endothelial cells (ECs), and perivascular cells (which include pericytes and smooth muscle cells) [17-19]. The heart also contains two pacemakers, a conduction system composed of specialized CMs, and a robust intracardial nervous system [20]. The primary ECM proteins include collagens, fibronectin, and elastin [21].

### *2.3. Cellular Organization*

Cardiac TCs focus mainly on modeling the myocardium. In the native myocardium, CMs are organized in layers 2–5 cells thick and are surrounded by cardiac FBs within an ECM that contains mainly collagen. CMs assume a rod shape with predominantly end-to-end connections with neighboring CMs, called intercalated discs, and circumferentially distributed connections with the surrounding ECM [15, 22]. Endothelial networks within the myocardium serve as conduits for blood to provide oxygen and nutrients and to remove carbon dioxide and waste.

### *2.4. Physical Stresses, Fluid Flow, and Electrical Signals*

The heart constantly pumps blood and is continually exposed to blood flow. However, the endocardium is the only layer that comes in direct contact with blood and experiences fluid shear. During the cardiac cycle, cells associated with all three layers of the heart (endocardium, myocardium, and epicardium) experience pressure and stretch. Pressure and stretch within a physiological range can promote physiological hypertrophy and enhance cardiac function. If applied in the pathological range, though, these stimuli frequently result in structural remodeling of the heart, which can ultimately lead to heart

failure. Electrical signals generated in the sinoatrial (SA) node are propagated rapidly through the heart via the atrioventricular (AV) node and cardiac conduction system (CCS). Additionally, due to numerous gap junctions at intercalated discs, the myocardium functions as a syncytium, allowing for the rapid propagation of action potentials from depolarized CMs to adjacent resting CMs downstream, which leads to organized, nearly synchronous heart contractions [23].

*2.5. Examples of Cardiac Tissue Chips*

In vivo, CMs assume a rod-like morphology with predominantly end-to-end contacts to neighboring CMs (intercalated discs) and circumferentially distributed costameres which connect the CM in tandem with integrins contractile machinery to the surrounding ECM [15, 22]. Several groups have used methods, such as microcontact printing [24] and nano topographical surface cues [25], to direct the patterning of CMs in two-dimensional (2D) culture. 2D CM culture is relatively straightforward and amenable to high throughput applications, but it is much less physiologically relevant than 3D culture. Native cardiac muscle is thick and composed of CMs interconnected in an intricate functional syncytium. Three-dimensional culture techniques can more faithfully replicate the cell-cell and cell-ECM contacts, and associated mechanotransduction signaling is seen in vivo than 2D CM culture models, which inherently lack many of these interactions [26-28]. Different spatial organizations of CMs in 3D can be accomplished via spheroid culture (without exogenous ECM) or seeding the cells in hydrogels, such as collagen I, fibrin, Gelatin Methacryloyl (GelMa), or alginate. CMs cultured as spheroids do not align longitudinally and frequently do not assume a rod-shaped morphology [28], while those cultured in hydrogels (primarily unidirectionally anchored hydrogels) self-assemble and

align similarly to those in native cardiac tissue [29]. Cellular alignment and the formation of intercalated discs are facilitated by the uniaxial reorganization of the underlying ECM that occurs as the hydrogel compacts along the lines of tension. While these 3D culture techniques capture more aspects of the in vivo CM niche and can be adapted for co-culture with other cell types, the user has little control over how the cells organize themselves. Three-dimensional printing techniques provide new opportunities for defining cellular organization at high densities and incorporating multiple cell types at pre-determined locations, allowing for higher control over the cellular organization than methods relying on self-assembly.

Native cardiac tissue undergoes a filling (diastole) and pumping (systole) cycle during each heartbeat. The amount of blood ejected during each cycle (stroke volume) depends upon the degree of stretch-induced in the left ventricle at the end of diastole (preload) and the load the heart must pump against to propel blood through the aortic valve (afterload). Increases in pressure and stretch often result in CM hypertrophy (increase in cell size) over time. Physiological hypertrophy is the increase in the size of the heart that occurs in the settings of development and exercise, whereas pathological hypertrophy (mainly affecting the left ventricular wall and, sometimes, the interventricular septum) occurs in the context of disease and is frequently associated with cardiac dysfunction [30]. Therefore, the culture of CMs under pressure and stretch regimens like those during the cardiac cycle may be essential for reproducing some in vivo-like phenotypes and functions.

As mentioned above, passive mechanical loads can be induced in 3D cultures by seeding cells in hydrogels, which are uniaxially anchored, usually between VELCRO® fasteners (Velcro Companies, Manchester, NH, USA), other hook-and-loop adhesive

strips, or posts of some variety. Over time, CMs will contract, compact the surrounding hydrogel, and generate increasing tension levels [29]. There are also several examples of efforts to deliver mechanical loads actively. In 2016, Marsano et al. introduced a microfluidic device with various hanging posts supporting fibrin gels. They used a pneumatic actuation system to induce uniform cyclic strain on 3D constructs of neonatal CMs and hiPSC-derived CMs (hiPSC-CMs) [31]. In 2010, Giridharan et al., as a part of our Sethu research group, developed a microfluidic cardiac cell culture model (μCCCM) that mimicked the hemodynamic stresses incurred during pressure−volume changes in the left ventricle via the 2D culture of cardiac cells on a thin polydimethylsiloxane (PDMS) membrane situated at the bottom of a cell culture chamber (Figure 2a) [32]. The model enabled in vitro investigations of the effects of mechanical forces, similar to those seen during different stages of gestational development, on the functional maturation of CMs [33]. Within the μCCCM, a peristaltic pump filled the chamber with media, with the resultant downward pressure stretching the membrane and overlying cells (simulating diastole). An external pulsatile pneumatic pump generated an upward pressure, returning the stretched cell layer and membrane to their original position and transmitting much of this pressure into the culture chamber itself (simulating systole). In 2016, we modified this setup with an additional collagen I/Matrigel coating to adapt hiPSC-CMs to physiological hemodynamic stresses by gradually increasing the filling volume and “systolic” pressure over the course of 72 h [34]. In 2019, this biomimetic cardiac tissue model (BCTM) was further adapted in our lab to culture cardiac cells in 3D using fibrin gels suspended between two posts anchored on top of a PDMS membrane (Figure 2b) [35]. Using this setup, the

researchers demonstrated that pressure–volume changes associated with cardiovascular development and disease could be accurately replicated in vitro.

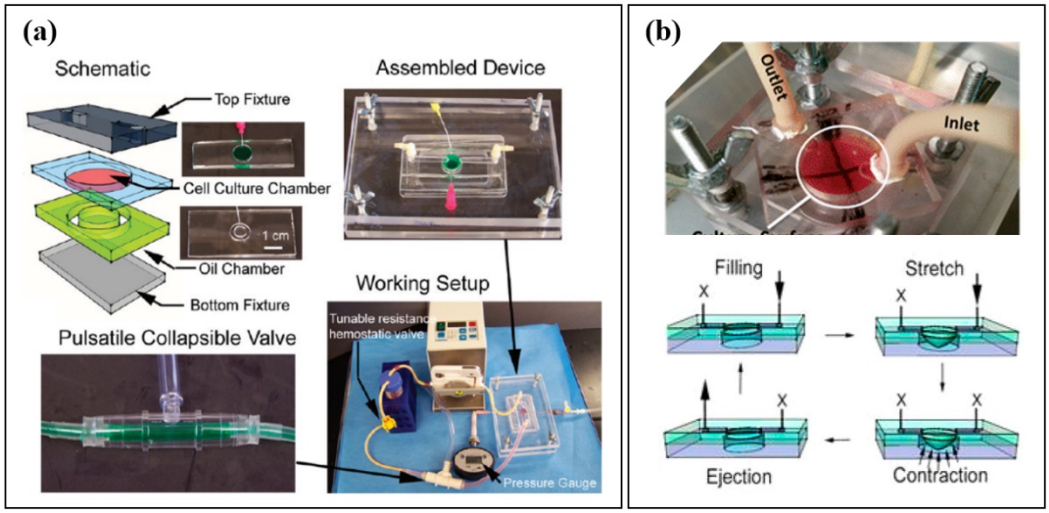


**Figure 2. Cardiac Tissue Chips.** (a) Microfluidic Cardiac Cell Culture Model developed by Giridharan et al., along with a schematic diagram, images of an assembled device, pulsatile collapsible valve, and the complete working setup. Reproduced with permission from the American Chemical Society [32]. (b) Biomimetic Cardiac Tissue Model (BCTM), developed by Rogers et al., depicting the cardiac cell culture chamber and schematic diagrams representing how the BCTM reproduces the cardiac cycle. Arrows represent the direction of fluid flow and membrane stretch. Reproduced with permission from the American Chemical Society [34].

Hansen et al. used a similar approach to generate engineered heart tissues (EHTs) of unpurified neonatal rat heart cells suspended in fibrin/Matrigel in rectangular casting molds in 2010 [36]. During gelation, a pair of PDMS posts suspended from above was lowered into the EHT, to which the construct then adhered while setting, allowing for its transfer out of the casting mold and into a medium-filled well. The researchers exposed the EHTs to known arrhythmogenic and cardiotoxic drugs, and the tissue strips demonstrated

expected responses. For example, quinidine and erythromycin caused increases in relaxation time, and doxorubicin led to gradual decreases in contractile force. This EHT model has been validated for several applications with hiPSC-CMs and commercialized by EHT Technologies GmbH (University Medical Center Hamburg-Eppendorf, Hamburg, Germany) [37, 38]. In 2016, Aung et al. developed a model capable of assessing CM contractile stress in real-time using soft lithography and microfluidic techniques [39]. In this TC, CMs labeled with a fluorescent marker were encapsulated in GelMa and seeded into a microfluidic device between two layers of non-degradable polyacrylamide gel filled with fluorescent tracking beads. The seeded device was then patterned via UV light exposure through a mask, eliminating CM-laden GelMa within microfluidic channels and other unwanted spaces. Deflected fluorescent signals from the bead-filled polyacrylamide gels served as "stress sensors" for the contractile stresses generated by the CMs' contraction.

In addition to mechanical loading, electrical stimulation is another critical design consideration in cardiac TCs. In vivo, CMs contract in response to action potentials generated by SA node [40]. Initially, these impulses spread through atrial CMs, leading to a slow contractile wave, as well as to the AV node. The action potential is briefly stalled at the AV node (allowing the atria to complete contraction, thus emptying as much blood as possible into the ventricles before they contract), and is then propagated to the ventricular myocardium through the cardiac conduction system (CCS), which is composed of specialized CMs that conduct electrical signals much more quickly than normal CMs [41]. Thus, the ventricular CMs contract in near synchrony. Recently, progress has been made in differentiating SA nodal cells from hiPSCs [42] and generating pacemaker cells

via the transfection of human mesenchymal cells with HCN1 [43]. However, the faithful recreation of the entire CCS will be challenging to achieve, and most cardiac TCs stimulate CM contraction via electrical pacing. Field stimulation is the most common method for pacing CMs, where the stimulating current is applied uniformly to the tissue using a pair of carbon or platinum electrodes [44]. In 2018, Ronaldson-Bouchard et al. developed a platform incorporating field stimulation via carbon electrodes to induce the maturation of hiPSC-CMs in a 3D culture [45]. They seeded hiPSC-CMs and FBs into a fibrin gel and cast the suspension into a mold between two flexible posts, which provided a passive mechanical load. By subjecting early-stage hiPSC-CMs (i.e., those which had just completed differentiation and begun spontaneously contracting) to progressively increasing frequencies of electrical stimulation, the researchers generated adult-like cardiac muscle over a month.

Some groups have developed optical stimulation techniques to avoid the hassle of integrating bulky electrodes, which present more straightforward options for pacing CMs. CM contraction is ultimately dependent upon the influx and efflux of specific ions. Therefore, researchers have designed and incorporated light-sensitive ion channels (channelrhodopsins), allowing for pacing via an optical illumination [46].

As an alternative, in 2018, Savchenko et al. developed graphene-based interfaces to optically stimulate CMs without any modification to the cells [47]. This approach utilizes graphene sheets or flakes in proximity to CMs, which cause membrane depolarization in response to light stimulation.

Additional methods allow for the direct electrical stimulation of CMs without incorporating bulky electrodes. For instance, Tandon et al. introduced surface-patterned

electrodes to electrically stimulate CMs in 2010 [48]. They employed excimer laser ablation to microfabricate patterned microelectrode arrays (MEAs) using indium tin oxide (ITO), which is non-toxic, for the electrical stimulation of neonatal rat CMs and human adipose tissue-derived stem cells (hASCs). Their technique allowed for high-resolution patterning of virtually flat electrodes so that cells could be cultured on top of them in a monolayer. In 2012, Ma et al. incorporated an ITO-based MEA, along with a microfluidic device created via soft lithography, to investigate the electrical conduction between neonatal rat CMs and rat mesenchymal stem cells from bone marrow (rMSCs-bm), in comparison to conduction between CMs and control cells (CMs or FBs) [49]. After seeding CMs in the device channel and allowing them to mature into a 2D cardiac muscle fiber, the fiber's central portion was scraped away with a glass pipet tip. rMSCs-bm or control cells were seeded into the now barren central portion of the fiber via laser patterning to allow single-cell resolution. Qian et al. also used a similar MEA TC design in 2017 and an additional interdigitated electrode array to fabricate a device to assess cellular electrophysiology, adhesion, and contractility in hiPSC-CMs [50]. In addition to the fine control over the electrical stimulation of cells, MEAs allow for measurements of extracellular field potentials. These measurements can approximate intracellular action potentials, obviating the need for low throughput, user-intensive single-cell patch clamps. Several lab groups have developed MEAs for recording action potentials from cells [50, 51], and several companies (e.g., Multi Channel Systems MCS GmbH, Reutlingen, Germany; Maxwell Biosystems, Zurich, Switzerland; Axion Biosystems, Atlanta, GA, USA) offer commercially available MEAs that can be integrated into multi-well plates for quantitative cardiac electrophysiology analyses to screen drugs for potential cardiotoxicity.

In 2014, Lin et al. developed a nanoelectrode array (NEA) that used nanoneedles to obtain intracellular patch-clamp recordings to increase these technologies' overall throughput [52]. Furthermore, an increasingly popular technique to monitor cardiomyocyte electrical activity is the use of voltage-sensitive dyes (VSDs) or potentiometric dyes. Voltage changes within the culture alter the measurable spectral properties. This electrode-free approach is compatible with high throughput imaging platforms and has advantages in both 2D and 3D cultures [53].

While the nodes and CCS are ultimately responsible for creating and distributing the electrical impulses that cause the heart to contract, the cardiac autonomous nervous system (CANS) significantly influences cardiac function [54]. Sympathetic and parasympathetic inputs to the SA node modulate heart rate. Meanwhile, inputs to the CMs affect parameters such as the force of contraction, the speed of relaxation, and the sensitivity to membrane polarization changes. The CANS has essential roles in normal physiology and is involved in numerous disease states, especially arrhythmias. Therefore, incorporating autonomic neurons into cardiac TC models increases their physiological relevance.

In 2017, Sakai et al. developed a cardiac chip containing hiPSC-CMs cultured atop an MEA in one chamber and rat sympathetic neurons (rSNs) cultured in a separate chamber, with microtunnels connecting the two [55]. After 3–4 days in culture, axons extended through these microtunnels and made physical contact with the hiPSC-CMs. The researchers demonstrated that, with increased neuronal firing frequency (via direct stimulation by electrodes in the microtunnels), the hiPSC-CMs had a higher contraction frequency. This increase in contraction rate was dependent upon both the presence of

sympathetic neurons and direct contact between these and the CMs. The addition of propranolol—a beta-adrenergic receptor blocker used clinically to slow the heart rate—to the CMs inhibited increases in beat frequency. This demonstrated that the neurons were influencing the CMs' behavior in a physiologically relevant manner, increasing the chip's applicability to disease modeling and screening proarrhythmic drugs.

In 2016, Oh et al. co-cultured neonatal mouse ventricular myocytes (NMVMs) and sympathetic neurons differentiated from hiPSCs in the same culture chamber to improve hiPSC-derived neuron maturation and to confirm that they functioned appropriately and formed cell–cell contacts with the CMs [56]. Immunofluorescence confirmed the formation of neuron–CM connections, the importance of which was demonstrated in two ways. First, when the co-culture was supplemented with nicotine, the CMs appropriately beat more rapidly and with greater force. This result was not observed in control groups lacking the sympathetic neurons. Second, the researchers transduced the neurons with a channelrhodopsin-coding gene, allowing them to be controlled via photostimulation. When the neurons were stimulated via light to fire more frequently, the CMs responded with an increased contraction frequency unless propranolol was also present, in which case most of the rate increase was blocked.

As discussed previously, all CMs in vivo typically contract in response to electrical impulses generated in the SA node, and ventricular CMs rely upon the CCS to receive these action potentials. When the organized action potential generation and propagation are disrupted, CMs contract spontaneously due to their heightened electrochemical sensitivity and fluxes in the intracellular calcium [57, 58]. While adult human primary CMs and many CM cell lines do not spontaneously contract in vitro, CMs derived from hiPSCs, embryonic

stem cells, and neonatal rodents retain this capacity [59]. Several research groups have sought to harness these CM populations' ability to spontaneously contract, developing models that replicate the 3D ventricular structure and demonstrate the ability to pump fluid without the need for external pumps or electrical stimulation.

Among the pioneers of this, Tanaka et al. developed a heart-on-a-chip pump that harnessed mechanical forces produced by spontaneously, synchronously contracting CMs to move fluid through a microfluidic channel in 2007 [60]. To achieve this, CMs were cultured as a monolayer until they demonstrated synchronous contractions generating significant force. The CM sheet was then detached and wrapped around a hollow elastomeric sphere containing inlet and outlet ports for the capillary channels and medium. In 2018, MacQueen et al. fabricated models of the left ventricle that more accurately mimicked ellipsoidal ventricular geometry via the pull-spinning of biocompatible, biodegradable polycaprolactone/gelatin nanofibers [61]. The ventricular scaffolds were seeded with either neonatal rat ventricular myocytes (NRVMs) or hiPSC-CMs, and both model types demonstrated synchronous chamber contractions 3–5 days after seeding. While the models had much lower cell densities than their in vivo counterparts and demonstrated relatively low ejection fractions and contractile work, they provided unrivaled geometric mimicry and synchronous contraction without the need for electrical stimulation. Additionally, when the researchers applied specific anatomical defects to the models, they observed stable pinned rotors and spiral waves, demonstrating their applicability for modeling arrhythmias secondary to structural defects.

### *2.6. Limitations*

Currently available cardiac TCs do a reasonable job of mimicking cardiac tissue architecture with appropriate cell types and ECM, replicating electrical and mechanical loads, and modeling both normal and disease states. However, to mimic heart function and cardiac tissue behavior, it is essential that the engineered cardiac TCs pump fluid against an afterload. For this to occur, the contractile forces generated by the engineered tissue need to be sufficiently large. With current technology, the maximum forces generated are orders of magnitude smaller than in native cardiac tissue [62]. Finally, modeling cardiovascular disease using cardiac TCs can significantly benefit from integrating aspects of the immune system.

## 3. Kidney Tissue Chips

### *3.1. Function*

The kidney's primary function is to remove waste products and excess fluid from the body, actively establishing and maintaining homeostasis. As blood from the afferent arteriole flows through the glomerular capillaries, Starling forces (hydrostatic pressure and oncotic pressure gradients) cause much of the plasma to pass into Bowman's space as glomerular filtrate [63]. Together, the capillary endothelium, basement membrane, and foot processes of the podocytes form the filtration barrier [64]. From here, the filtrate travels down the proximal tubule, where most water, salts, and organic solutes are reabsorbed into the peritubular capillaries. The filtrate then enters the loop of Henle, where more water and $Na^+$ and $Cl^-$ ions are reabsorbed, followed by the distal convoluted tubule. Although not technically part of the nephron, the collecting duct system follows the distal tubule, and it

is the site where $Ca^{2+}$, $Na^{+}$, and $Cl^{-}$ are actively reabsorbed. The remaining filtrate is excreted as urine through the renal calyces [65].

### *3.2. Cell Types and Extracellular Matrix*

The nephron is the kidney's functional unit, and each kidney contains approximately 1.2 million of them [64]. Each nephron consists of a plasma filtration unit called the renal corpuscle, which is composed of a specialized tuft of capillaries (the glomerulus) and the surrounding Bowman's capsule, and a segmented renal tubule, which includes a proximal tubule, the loop of Henle, a distal tubule, and a connecting tubule, which connects to the collecting tubules and ducts. The renal corpuscle consists of four different cell types, including the glomerular endothelial cells (GECs) and mesangial cells (MCs) found within the glomerulus, the podocytes of the visceral Bowman's capsule layer, and the parietal epithelial cells (PEpCs) of the parietal Bowman's capsule layer. The PEpCs are in continuity with the renal proximal tubular epithelial cells (RPTEpCs). The glomerular ECM primarily comprises collagen type IV, laminin, and heparan sulfate proteoglycans. The tubular ECM predominantly comprises different types of collagens, glycosaminoglycans, polysaccharides, and glycoproteins, such as fibronectin.

### *3.3. Cellular Organization*

The renal corpuscle is essentially a plasma filtration barrier. It consists of three layers, the fenestrated capillary ECs, the glomerular basement membrane (synthesized by the capillary ECs and podocytes), and the interdigitated pedicles of the podocytes. The renal tubule consists of sequential tubular segments composed of tubular epithelial cells (TEpCs) of varying morphologies. The proximal tubule is lined by cuboidal epithelium,

with an extensive brush border of microvilli. The loop of Henle contains a flat squamous epithelium, and the distal convoluted tubule and connecting tubule consist of cuboidal epithelium. The basal aspects of the TEpCs are anchored to a basement membrane. All epithelial cells within the nephron and collecting duct, except for the intercalated cells, have an apical single and nonmotile primary cilium that extends into the fluid [64]. These primary cilia work as mechanosensors and chemosensors, sensing changes in flow rate and chemical compound alterations, respectively. Though not strictly considered a portion of the nephron, the peritubular capillaries and vasa recta lie alongside the renal tubule and actively participate in the secretion and reabsorption [63].

*3.4. Physical Stresses and Fluid Flow*

The biomechanical forces within the nephron, including the pressure, circumferential stretch, and fluid shear stress, are integral to several distinct signaling pathways and transport phenomena. Furthermore, tubular flow rates are dynamic and vary dramatically between different nephron segments [66]. Alternations in flow rate occur in concert with changes in glomerular filtration rate (GFR), tubuloglomerular feedback (TGF) via the macula densa, pelvic wall contraction, and reabsorption rates [67-72]. In general, TEpCs experience a fluid shear stress an order of magnitude smaller than endothelial cells (less than 1.0 dyne/cm$^2$) [67, 73]. The average tubular pressure decreases along the nephron from approximately 13 mmHg in the proximal tubule to less than 7 mmHg in the collecting duct [73, 74]. Within the glomerulus, ultrafiltration from the glomerular capillaries into Bowman's space occurs due to Starling forces. The approximate net ultrafiltration pressures are 17 mmHg on the afferent end and 8 mmHg on the efferent end [64]. In

response to vasoconstrictors and vasodilators, the nephron will alter shear stress and stretch to ultimately influence the GFR and the renal blood flow [75, 76].

### *3.5. Examples of Kidney Tissue Chips*

One of the primary goals of kidney TC engineering is developing platforms for high-throughput, reliable assessment of drug toxicity affecting the renal proximal tubule. RPTEpCs are very metabolically active, thus requiring a near-constant energy supply. They are continuously exposed to high concentrations of drugs and their toxic metabolites, making them highly susceptible to damage. The first human kidney TC model developed by Jang et al., in 2013, consisted of a porous polyester membrane coated with collagen IV sandwiched between two PDMS slabs [77]. The upper PDMS slab contained inlet and outlet ports for media and cells and a flow channel directly atop, and in contact with, the collagen-coated porous membrane. The lower PDMS slab contained a media reservoir, with ports for sampling and adding media/compounds directly below and in contact with the porous membrane's unmodified basal surface. After seeding the membrane's apical (upper) side with RPTEpCs and allowing them to grow into a confluent monolayer, the cells were exposed to physiologic shear stress by flowing media through the upper PDMS channel. This device configuration mimics the in vivo architecture of the proximal tubule. The upper PDMS flow channel and underlying cell-covered porous membrane represent the tubule's lumen and wall, respectively, with the media reservoir in the lower slab acting as the interstitial space surrounding the tubule. Compared to static controls cultured in Transwell® (Corning Inc., Corning, NY, USA) systems, RPTEpCs subjected to physiologic flow showed enhanced epithelial polarization and primary cilia formation, indicating that cells were recapitulating in vivo organizational characteristics. RPTEpCs that experienced

flow demonstrated more significant albumin transport, glucose reabsorption, and brush border alkaline phosphatase activity. Furthermore, RPTEpCs exposed to cisplatin (via the "interstitial" lower media reservoir) in the flow model more closely mimicked in vivo responses to the drug than those in static culture. Though this model represented a significant advancement over traditional culture systems, it did not attempt to recapitulate the crosstalk between the proximal tubule and peritubular capillaries, which is integral to kidney function. Furthermore, these early designs employed cells in a monolayer format, rather than the tubular architecture found in vivo.

Jang et al.'s model and other 2D planar systems allowed for investigations of well-differentiated TEpCs in environments where shear, stretch, and pressure can be finely tuned, but they lack critical 3D components of the nephron and kidney that could impact the accuracy and relevance of resulting data. These 3D characteristics include open tubule lumens lined on all sides by TEpCs, surrounding interstitial ECM and peritubular capillaries, and architecture consisting of convoluted and straight segments, amongst others. Additionally, when compared to 2D models, 3D kidney TCs have demonstrated cellular responses to nephrotoxins that more closely resemble those seen in vivo [78], and they also maintain the viability and differentiation of TEpCs for longer periods of time [79]. In 2016, Weber et al., using a platform developed by Nortis Inc., characterized a 3D flow-directed human renal proximal tubule microfluidic model (Figure 3a) [80]. Microfiber inserts were first positioned to maintain a hollow tubular structure, and then collagen I was injected and allowed to gel. Subsequently, the microfiber inserts were removed, and the device was flooded with collagen IV, a significant constituent of the RPTEpC basement membrane. After this luminal coating gelled, the model was seeded

with primary human RPTEpCs, and media flow was initiated after 24 h. Researchers were able to generate a perfusable in vitro renal proximal tubule with dimensions comparable to its in vivo counterpart. The seeded RPTEpCs assumed appropriate polarity, demonstrating microvilli and the tight junction protein zonula occludens-1 at the apical aspects, and $Na^+/K^+$ ATPase and extensive membrane interdigitations at the basolateral aspects. RPTEpCs in this model did not express the kidney injury molecule-1 (KIM-1), an acute kidney injury marker that is expressed by kidney cells in 2D static culture. RPTEpCs in this model demonstrated glucose transport, ammoniagenesis, vitamin D bioactivation, and glutathione metabolic activity for over four weeks. The results suggested that 3D, flow-driven models of the proximal tubule offer advantages over 2D models beyond more accurate structural mimicry. In addition to recreating the proximal tubule, the device also had a "vascular" channel that, similar to the peritubular capillaries, could deliver solutes to the tubule's exterior surface. By introducing para-aminohippurate and indoxyl sulfate into media flowing through this channel, the researchers demonstrated significant transport of these solutes through the collagen-filled "interstitial space" and into the tubule lumen. These renal TC advancements allow for renal tubular drug secretion studies that are not possible with traditional Transwell® culture systems.

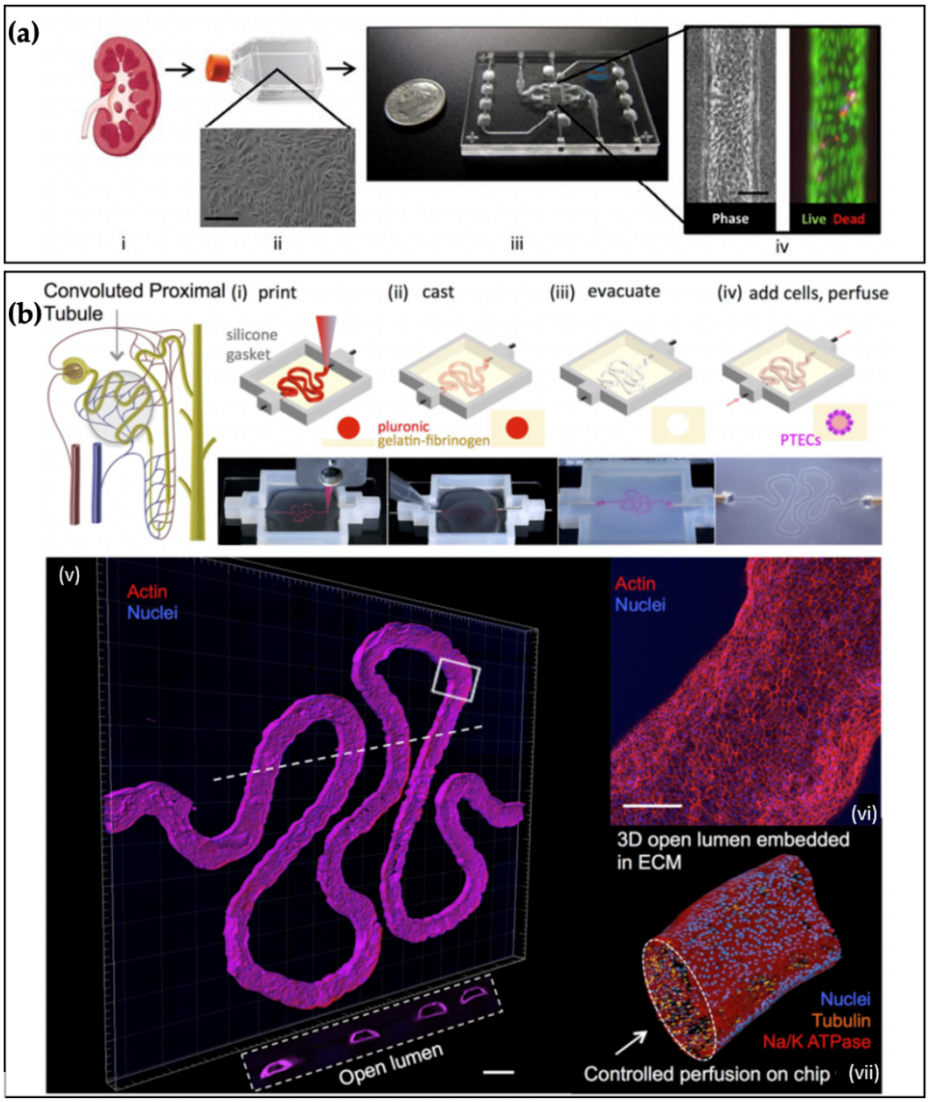


**Figure 3. Renal Tissue Chips.** (a) Schematics of isolated human kidney tissue (i–ii) seeded into Nortis Inc.'s single-channel 3D MPS platform (iii) with phase contrast and live/dead images of primary RPTEpCs at day 28 (iv). Reproduced with permission from Elsevier [80]. (b) Convoluted proximal tubule schematic and images of Homan et al.'s 3D bioprinting fabrication steps (i–iv) and confocal 3D renderings of their RPTEpCs organized into a tubule with an open lumen: actin (red), nuclei (blue), and tubulin (orange). Reproduced with permission from [81]. The work was published under a CC BY license

(Creative Commons Attribution 4.0 International License; https://creativecommons.org/licenses/by/4.0/).

In 2016, Homan et al. were the first to develop a protocol that combined bioprinting and 3D cell culture to create 3D perfusable proximal tubules that were fully embedded within an ECM (Figure 3b) [81]. Bioprinting allowed the researchers to more accurately replicate the initial portion of the proximal tubule's convoluted nature and generate tubule diameters of 150 to 700 μm. As in previous studies, the RPTEpCs subjected to fluid shear exhibited polarization, developed primary cilia and a robust microvilli brush border, and appropriately expressed $Na^+/K^+$ ATPase and AQP1. This TC could be used to qualitatively (via immunostaining) and quantitatively (via diffusional permeability measurements) assess acute and chronic drug-induced nephrotoxicity due to the 65-day-plus viability of the incorporated cells. In 2019, some of the same researchers expanded on this model by incorporating a peritubular capillary adjacent to the proximal tubule, with a thin layer of permeable ECM separating the two tubular structures. This 3D VasPT, as the researchers called it, was housed within a closed-loop perfusion system and used to investigate the renal reabsorption of albumin and glucose, as well as the effects of hyperglycemia [82]. The 3D VasPTs recapitulated the selective reabsorption capacity of RPTEpCs and the peritubular capillary-proximal tubule crosstalk seen in vivo. However, the tissue models were only around 20% as efficient as in vivo counterparts regarding glucose reabsorption. Therefore, while this TC made substantial improvements to the 2016 model, opportunities exist to further enhance the reabsorption and secretion capabilities of in vitro proximal tubules.

Rein et al., including researchers who worked on these bioprinted proximal tubule TCs, in 2020 created an in vitro model of the cortical collecting ducts (CCDs) [83], which contribute to the maintenance of the total body electrolyte, acid/base, and fluid homeostasis, and exert significant control over blood pressure [84-87]. This group of researchers used 3D printing to generate the TC's frame and provided a tubule lumen by inserting a 510 μm diameter pin through holes in opposite edges of the frame before filling the chamber with a gelatin/fibrin ECM. After allowing the ECM to solidify, the pin was removed, and the lumen seeded with immortalized mouse mpkCCD cells. This cell line exhibits phenotypes similar to principal cells (PCs), having the capacity to reabsorb $Na^+$ and water and secrete $K^+$. Within one week of initiating media perfusion, the researchers observed a tight epithelial barrier composed of differentiated and polarized PCs displaying apical epithelial $Na^+$ channels (ENaCs) and basolateral $Na^+/K^+$ ATPases. This model has the potential to explore the molecular mechanisms responsible for the regulation of transport within CCDs.

Until recently, glomerulus TCs have had limited success because immortalized podocytes readily dedifferentiate when cultured in vitro. In 2017, Musah et al. significantly advanced the field of kidney TC engineering by demonstrating an efficient (>90%) and chemically-defined protocol to differentiate hiPSCs into podocytes [88]. These researchers were able to show that the hiPSC-derived podocytes expressed markers of the mature phenotype (nephrin$^+$, WT1$^+$, podocin$^+$, Pax-2$^-$) and exhibited primary and secondary pedicles, which are largely absent in immortalized podocyte cell lines. The researchers then adapted this protocol to differentiate hiPSCs into podocytes within a microfluidic device. The hiPSCs were seeded into one channel of a microfluidic device separated by a

permeable membrane (mimicking the glomerular basement membrane) from another microfluidic channel coated with human glomerular ECs. Podocyte differentiation media was perfused through the hiPSC channel, and EC culture medium flowed through the other, and cyclic strain (mimicking that generated in the glomeruli with each cardiac cycle) was applied. Compared to podocytes differentiated under fluid flow alone, these hiPSC-derived podocytes demonstrated more intense nephrin staining and an increased cytoplasmic to nuclear nephrin staining pattern, indicating a more mature phenotype. The hiPSC-derived podocytes produced collagen IV within this glomerular TC, mimicked podocyte-capillary wall interactions, and demonstrated a differential filtration of albumin and inulin.

### *3.6. Limitations*

Over the past decade, there have been significant advancements within the field of kidney TCs. However, the kidney remains one of the most challenging organs to fully reconstruct in vitro because it comprises 26 cell types and is organized into such intricate functional units [89]. While current efforts mimic specific aspects of kidney function, such as glomerular filtration or tubular reabsorption, there has been little to no progress towards a single platform that combines these complex functions. Current models also do not accurately replicate fluid flow within different parts of the nephron. Fluid flow is associated with specific hemodynamic stresses, such as pressure, shear, and stretch, which affect cellular organization and function and could be critical in replicating in vivo-like tissue behavior. The greater characterization (and further development) of immortalized kidney cell lines, a more detailed understanding of renal tubular reabsorption and secretion functions, and the continued incorporation of associated vasculature will hopefully provide

low-cost and more accurate alternatives to the current methods employed in therapeutic studies and disease modeling.

## 4. Microphysiological Systems

While recent advances in TC engineering have allowed for more refined and reproducible approaches to tissue-/organ-specific drug toxicity screening, bridging the gap between pre-clinical studies and human trials without animal models requires recreating critical system-level interactions between interdependent organs and tissues with microphysiological systems (MPSs). Incorporating these multisystem interactions is necessary because drug toxicity is frequently not limited to a single organ or tissue. For instance, many patients receiving cancer treatment develop chemotherapy-induced cardiotoxicity (CIC), even when receiving targeted therapeutics [90]. While agents targeted at preventing CIC, such as dexrazoxane, exist, they frequently decrease the chemotherapy's effectiveness. MPSs that recreate interactions between the tumor microenvironment and cardiac tissue could be used to screen combinations of chemotherapeutics and cardioprotective therapies to evaluate both tumor regression and cardiotoxicity. More generally, in addition to the target organ/tissue, it may be beneficial to incorporate elements of the gastrointestinal (GI) system or skin to evaluate drug routes of entry; the circulatory system, to model the distribution of the drug; the liver, to understand metabolic breakdown of a prodrug or drug; and the kidneys, to determine the rate of clearance of the drug from the body. As with drug screening applications, TCs allow for the more precise modeling of tissue-/organ-specific disease processes than animal models, but their accuracy is limited by the lack of functional interactions between interdependent organ systems. One example of the type of multisystem disease process not captured by TCs is the pathophysiology of

secondary hyperparathyroidism (SHPT). SHPT frequently develops due to deformations in vitamin D metabolism and calcium-handling in dysfunctional kidneys, and the resultant abnormal elevation of parathyroid hormone leads to increased levels of intracellular calcium and oxidative stress, provoking pathological cardiac remodeling, conduction abnormalities, coronary artery and heart valve calcification, and hypertension [91]. Similarly, while TCs can incorporate immune cells, they lack lymphoid tissues, such as bone marrow, spleen, and lymph nodes, without which the activation, expansion, and recruitment of immune cells to different parts of the body in response to injury or infection cannot be modeled.

One of the earliest MPS platforms for drug toxicity studies was the microscale cell culture analog developed by Viravaidya et al. in 2004 (Figure 6a) [92]. This platform was designed to recreate interactions between the lungs and liver to model naphthalene metabolism and incorporated cell-free microfluidic channels of differing geometries to recapitulate fluid distribution dynamics in tissues perfused at different rates. Since then, multiple other examples of successful MPSs have integrated two or more tissue compartments. Several groups have developed heart-liver MPSs to study liver-metabolized drug effects on cardiomyocyte function [93, 94]. An example of a heart-liver-vascular MPS is the HeLiVa platform developed by Vunjak-Novakovic et al. in 2013, in which liver and cardiac micro-"tissues" were functionally connected by EC-lined vascular channels, with all incorporated cells having been derived from iPSCs [95]. These cells' origins are critical, as models incorporating iPSC-derived cells are suitable for patient-specific drug screening applications. In 2017, Skardal et al. published a model that successfully incorporated heart, lung, and liver TCs together in a closed circulatory system [96]. The researchers observed

in vivo-like drug responses from cells in this MPS, illustrating the value of integrating multiple TCs for drug testing. In 2020, Schimek et al. developed a lung-liver MPS to model the effects of inhaled substances metabolized by the liver, enabling the assessment of both toxicity and the bioavailability of respiratory agents [97]. Using this model, the researchers saw differing responses of bronchial epithelial cells exposed to aflatoxin $B_1$ when they were cultured with HCs in a separate chamber versus when the liver cells were excluded. This demonstrated that the device enabled crosstalk between the two cell populations analogous to that seen in vivo. This platform could become a powerful tool for pharmaceutical development and personalized medicine. Lastly, in 2015, Maschmeyer et al. developed a four-organ-chip MPS that connected the human intestine, liver, skin, and

kidney and provided physiologic fluid flow to each distinct "organ" (Figure 4b) [98]. Using this model, the researchers demonstrated the establishment of homeostasis between the organ chambers within 2 to 4 days. They observed cell viability and the barrier integrity of the kidney and intestine components for over 28 days, making the four-organ-chip MPS a suitable platform for absorption, distribution, metabolism, and excretion drug profiling studies, as well as repeated dose, long-term drug toxicity screens. For further reading on MPSs, please see Table 1.

**Table 1.** Microphysiological Systems.

| Year | Author | Organs/Tissues | Application |
|---|---|---|---|
| 2004 | Viravaidya et al. [92] | Lung–Liver–Fat | Napthalene toxicity |
| 2013 | Wagner et al. [99] | Liver–Skin | Drug Testing |
| 2013 | Vunjak-Novakovic et al. [95] | Heart–Liver–Vascular | Drug Testing |
| 2014 | Lin et al. [100] | Bone–Cartilage | Drug Testing |
| 2014 | Clark et al. [101] | Liver–Tumor | Testing Therapeutic Strategies |
| 2015 | Maschmayer et al. [102] | Liver–Skin/Intestine | Drug Testing |
| 2015 | Maschmayer et al. [98] | Intestine–Liver–Skin–Kidney | Drug Pharmacodynamics and Toxicity |
| 2016 | Esch et al. [103] | GI Tract–Liver | Disease Modeling |
| 2016 | Moura Rosa et al. [104] | Lymph Node–Immune Cell | Disease Modeling and Drug Testing |
| 2017 | Loskill et al. [105] | Adipose–Vascular | Disease Modeling |
| 2017 | Skardal et al. [96] | Liver–Heart–Lung | Drug Efficacy and Toxicity |
| 2017 | Tsamandouras et al. [106] | Gut–Liver | Drug Pharmacokinetics |
| 2018 | Oleaga et al. [94] | Heart–Liver | Cardiotoxicity |
| 2019 | McAleer et al. [93] | Heart–Liver | Terfenadine Pharmacokinetics |
| 2020 | Yin et al. [107] | Heart–Liver | Testing Anti-depressant Drugs |
| 2020 | Schimek et al. [97] | Lung–Liver | Toxicity of inhaled substances |
| 2020 | Baert et al. [108] | Liver–Testis | Reproductive toxicity |
| 2020 | de Mello et al. [109] | Heart–Liver–Skin | Topical Drug Delivery |
| 2020 | Kwak et al. [110] | Skin–Vasculature | Immune responses |
| 2020 | Sung et al. [111] | Gut–Liver | Drug Testing |
| 2020 | Clark et al. [112] | Liver–Tumor | Tumor Metastasis |
| 2020 | Jeon et al. [113] | Gut–Liver–Immune Cell | Modeling inflammatory responses |
| 2020 | Marin et al. [114] | Liver–Intestine | Drug pharmacological and toxicological assessment |
| 2021 | Giordano et al. [115] | Gut–Kidney | Chronic Kidney Disease Modeling |

# 5. Challenges Associated with the Design and Construction of Microphysiological Systems

## *5.1. Communication*

The primary challenge associated with integrating multiple TCs to form an MPS is establishing communication between two or more "tissues" or "organs" that accurately recreates the crosstalk experienced in vivo. As seen above, technologies, such as photolithography, soft lithography, micropatterning, 3D printing, bioprinting, and microfluidics, can be used to fabricate co-culture models that mimic in vivo tissue organization and cell–cell/cell–ECM contacts. This allows for direct communication between different "tissues" or "organs" and recapitulates critical parameters influencing mechanotransduction signaling pathways. Communication among tissues/organs that are not in direct contact with one another can be enabled. Devices engineered to house different tissue/organ models within separate chamber that are connected via microfluidic channels ensure soluble factor signaling via culture medium circulation. Microfluidic devices can also be adapted to facilitate more complex signaling in several ways, such as utilizing different microfluidic channel architectural features and micro/nanoscale pore structures to establish spatiotemporal molecular gradients [116, 117] and particle size exclusion [118, 119]. Functional physiologic barriers can also be generated by culturing appropriate cell types in architectures that mimic in vivo organization.

In vitro culture of cells and tissues involves specific cell culture media formulations to maintain viability and in vivo-like phenotype and function [120]. In the human body, blood plays the role of the cell culture medium with supporting tissues and cells producing the necessary growth factors. MPSs frequently do not include all of the supporting cells

necessary to provide the specific soluble factors for maintaining the viability, phenotypes, and functions of the incorporated “tissues”/”organs.” This is often by choice, as researchers are only seeking to model specific tissues and organs and want to minimize extraneous variables. However, in most cases, it is also difficult to incorporate all the requisite supporting cells (which differ based on the “tissue”/”organ” composition of the device). Thus, considerations must be made concerning what media formulations are necessary for various combinations of “tissues”/”organs.” To simplify device operation and simulate how different tissues and organs communicate in vivo, researchers frequently seek to use one medium supplemented with the various nutrients and soluble factors necessary to satisfy the incorporated “tissues”/”organs”. Formulating this sort of common medium can be very challenging, as specific soluble factors required by one cell type can negatively impact the function or phenotypic maintenance of another.

The manner in which the medium is perfused through MPSs is another important parameter to consider. Establishing and maintaining physiological fluid flow among multiple “tissues”/”organs” is challenging, as in vivo flow rates vary significantly in different tissues/organs. As discussed previously, fluid flow is associated with shear stress, pressure, and stretch. In vivo, most tissues/organs have extensive capillary networks through which blood flows very slowly, exposing ECs lining the microvessels to low shear stress and pressure and the surrounding cells of the tissues/organs to negligible stretch. Microfluidic technology allows for channels within MPSs that provide fluid flow within the main perfusion networks but do not directly interact with cells comprising the “tissues”/”organs,” thus utilizing primarily diffusive transport to deliver oxygen and nutrients to the cells [121]. However, one caveat to this approach is that microvascular

networks or other small lumens must be established within the “tissues”/”organs” if their thicknesses are scaled up beyond a couple of hundred μm, due to the diffusion limitation of oxygen [122, 123]. Unlike capillaries, arterial and venous vascular tissues are subject to non-negligible amounts of shear stress. As discussed previously, combinations of lithographic techniques and 3D printing can fabricate vascular channels that mimic the geometry of in vivo vasculature. One can reproduce physiologic shear stress, pressure, and stretch on the ECs lining the lumens by tuning the stiffness of whatever material surrounds these vascular channels and employing physiologic flow profiles. Microfluidic systems are compatible with various active and passive pumping techniques that can generate steady and pulsatile flow. The heart is a pulsatile pump and contains four valves that ensure blood moves in the forward direction. Likewise, in vitro, unidirectional flow control valves must be incorporated to ensure that the cyclic filling and contraction of the “heart” propels cell culture medium in the intended direction. Using microfluidic approaches, several groups have developed both active and passive flow control valves that can be used to ensure pulsatile pumping and unidirectional flow, similar to that seen in the body [124-126]. Microfabrication techniques can also create alternatives to cardiac tissue via the development of pumps to generate pulsatile flow, similar to the heart [35, 127]. In summary, fluidic circuits can be tailored via geometry, perfusion rate, and organization adjustments, along with incorporating components, such as actuators and valves (both in tubing connecting different TCs and within the TC devices themselves), to meet perfusion and transport requirements.

*5.2. Nondestructive Monitoring*

MPS platforms are functionally more complex and more challenging to construct than individual TCs. Therefore, the efficient utilization of these complex multi-organ MPSs is best accomplished if the monitoring of cellular/"tissue"/"organ" function can be performed in a non-destructive fashion, thereby enabling periodic or even continuous measurements of cellular responses. Non-destructive testing allows multiple drugs or therapeutic strategies to be tested with the same platform in a sequential fashion. Soft lithography microfabrication techniques are often employed to fabricate the structural housing for tissue culture, whereas conventional surface and bulk micromachining techniques, frequently used for semiconductor fabrication, have been utilized to enable on-chip biosensing. Biosensing includes the measurement of biophysical signals, such as cellular action potentials, intracellular calcium signaling, transepithelial electrical resistance (TEER), and cellular impedance [128], as well as biochemical measurements, including gene expression, intracellular and secreted proteins, biomarkers of injury, and measurements of local pH and oxygen levels. Several devices enable the non-destructive measurement of cellular action potentials via microelectrode arrays or nanoneedle arrays [129-131]. Additionally, endothelial and epithelial TCs have been fabricated with micro/nanoporous membranes coupled with electrodes to allow for non-destructive TEER measurements [132, 133]. Micromachined electrodes have also been used to measure cellular electrical resistance and impedance, which provide information regarding cell size and intracellular complexity [96, 134]. Sensors have been developed to measure local oxygen, pH, and signaling molecule levels, such as nitric oxide [84,191,192]. Antibody arrays have been integrated downstream of cell cultures to measure soluble factor

production, where the quantitative assessment of specific molecules is converted to optical or electrical signals that can be continuously monitored [135]. Overall, while some critical technical advances have enabled non-destructive readouts from MPSs, integrating simple and reliable readouts that can be used to evaluate changes that occur as a consequence of toxicity or disease is essential. Continued progress in biosensing will hopefully significantly increase the number of assayable signals and the sensitivity and specificity with which they can be measured. Such advancements will be critical to the widespread acceptance and usage of complex multi-cellular MPS in the greater scientific community.

### *5.3. Material Selection and Fabrication of TCs and MPS*

The selection of materials and fabrication techniques used to build TCs and MPSs requires careful consideration of the tissue/organ model of interest, culture conditions, desired electrical and mechanical stimuli, throughput of the system, biocompatibility issues, and methods used for monitoring and detection. TC and MPS platforms require biocompatible materials to provide structural support for engineered tissues and to promote healthy or diseased tissue phenotype and function. Desirable biomaterial properties include minimal cellular toxicity [136], minimal absorption of biomolecules and drugs [137], transparency to facilitate on-chip imaging, and sufficient gas permeability to ensure oxygen transport to cells in culture. PDMS fulfills many of these requirements and is widely used in the early-stage development and prototyping of TCs and MPSs [138]. More complex or advanced models may employ other polymers such as polycarbonate, polystyrene, and polymethyl methacrylate. These compounds are compatible with high-throughput fabrication techniques such as injection molding, embossing, and 3D printing. Glass is also frequently used in the construction of TCs and MPSs as it fulfills many of the requirements

for supporting cell/tissue culture and is compatible with the integration of active sensing and actuating elements. TCs and MPSs that require the integration of electrodes and electrochemical sensors have also utilized semiconductor materials, such as silicon, for their construction. The main drawback of glass and silicon is that complex fabrication techniques are necessary, and silicon is not an optically transparent material.

## 6. Summary

Overall, TCs and MPSs have great potential to revolutionize drug discovery, drug toxicity testing, and disease modeling by providing models of human health and disease. There has been significant progress in ensuring that TCs accurately replicate human physiology and in the engineering of complex interactions between different TCs. Despite this progress, TCs and MPSs have yet to find widespread application in establishing disease models and discovering and evaluating drugs. This can be attributed to limitations in the ability of TCs to completely replicate the in vivo environment and complexities associated with the construction and operation of TCs and MPSs. Microfluidics provides unique opportunities to address these issues and enable the design of a modular plug and play TCs that accurately mimic critical aspects of the in vivo environment in a simple and easy-to-use manner. Finally, we stress that, with advances in the complexity of engineered systems, it is also important to ensure that the developed platforms are also simple to use, inexpensive, and highly reproducible to ensure widespread adoption in research and industry.

Reference:


1. DiMasi, J.A., H.G. Grabowski, and R.W. Hansen, *Innovation in the pharmaceutical industry: New estimates of R&D costs.* J Health Econ, 2016. **47**: p. 20-33.
2. Dickson, M. and J.P. Gagnon, *Key factors in the rising cost of new drug discovery and development.* Nat Rev Drug Discov, 2004. **3**(5): p. 417-29.
3. DiMasi, J.A., R.W. Hansen, and H.G. Grabowski, *The price of innovation: new estimates of drug development costs.* J Health Econ, 2003. **22**(2): p. 151-85.
4. Tagle, D. *National Center for Advancing Translational Sciences: About Tissue Chip*. [cited 2020 November 28, 2020
]; Available from: https://ncats.nih.gov/tissuechip/about.
5. Tagle, D. *National Center for Advancing Translational Sciences: Tissue Chip Initiatives & Projects*. November 28, 2020]; Available from: https://ncats.nih.gov/tissuechip/projects.
6. Raimondi, I., et al., *Organ-On-A-Chip in vitro Models of the Brain and the Blood-Brain Barrier and Their Value to Study the Microbiota-Gut-Brain Axis in Neurodegeneration.* Front Bioeng Biotechnol, 2019. **7**: p. 435.
7. Doryab, A., G. Amoabediny, and A. Salehi-Najafabadi, *Advances in pulmonary therapy and drug development: Lung tissue engineering to lung-on-a-chip.* Biotechnol Adv, 2016. **34**(5): p. 588-596.
8. Bein, A., et al., *Microfluidic Organ-on-a-Chip Models of Human Intestine.* Cell Mol Gastroenterol Hepatol, 2018. **5**(4): p. 659-668.
9. Abadpour, S., et al., *Pancreas-on-a-Chip Technology for Transplantation Applications.* Curr Diab Rep, 2020. **20**(12): p. 72.
10. Heidari-Khoei, H., et al., *Organoid technology in female reproductive biomedicine.* Reprod Biol Endocrinol, 2020. **18**(1): p. 64.
11. Low, L.A., et al., *Organs-on-chips: into the next decade.* Nat Rev Drug Discov, 2020.
12. Zhang, B., et al., *Advances in organ-on-a-chip engineering.* Nat Rev Mater, 2018. **3**(8): p. 257-278.
13. Kashaninejad, N., et al., *Organ-Tumor-on-a-Chip for Chemosensitivity Assay: A Critical Review.* Micromachines (Basel), 2016. **7**(8).
14. Anderson, R.M., J.M. Fritz, and J.E. O'Hare, *The mechanical nature of the heart as a pump.* Am Heart J, 1967. **73**(1): p. 92-105.
15. Ehler, E., *Cardiac cytoarchitecture - why the "hardware" is important for heart function!* Biochim Biophys Acta, 2016. **1863**(7 Pt B): p. 1857-63.
16. Nakagawa, Y., T. Nishikimi, and K. Kuwahara, *Atrial and brain natriuretic peptides: Hormones secreted from the heart.* Peptides, 2019. **111**: p. 18-25.
17. Avolio, E., et al., *Perivascular cells and tissue engineering: Current applications and untapped potential.* Pharmacol Ther, 2017. **171**: p. 83-92.
18. Banerjee, I., et al., *Determination of cell types and numbers during cardiac development in the neonatal and adult rat and mouse.* Am J Physiol Heart Circ Physiol, 2007. **293**(3): p. H1883-91.
19. Zhou, P. and W.T. Pu, *Recounting Cardiac Cellular Composition.* Circ Res, 2016. **118**(3): p. 368-70.

20. Achanta, S., et al., *A Comprehensive Integrated Anatomical and Molecular Atlas of Rat Intrinsic Cardiac Nervous System.* iScience, 2020. **23**(6): p. 101140.
21. Lockhart, M., et al., *Extracellular matrix and heart development.* Birth Defects Res A Clin Mol Teratol, 2011. **91**(6): p. 535-50.
22. Samarel, A.M., *Costameres, focal adhesions, and cardiomyocyte mechanotransduction.* Am J Physiol Heart Circ Physiol, 2005. **289**(6): p. H2291-301.
23. Vaidya, D., et al., *Null mutation of connexin43 causes slow propagation of ventricular activation in the late stages of mouse embryonic development.* Circ Res, 2001. **88**(11): p. 1196-202.
24. Atmanli, A. and I.J. Domian, *Generation of aligned functional myocardial tissue through microcontact printing.* J Vis Exp, 2013(73): p. e50288.
25. Kim, D.H., et al., *Nanoscale cues regulate the structure and function of macroscopic cardiac tissue constructs.* Proc Natl Acad Sci U S A, 2010. **107**(2): p. 565-70.
26. Duval, K., et al., *Modeling Physiological Events in 2D vs. 3D Cell Culture.* Physiology (Bethesda), 2017. **32**(4): p. 266-277.
27. Savoji, H., et al., *Cardiovascular disease models: A game changing paradigm in drug discovery and screening.* Biomaterials, 2019. **198**: p. 3-26.
28. Zuppinger, C., *3D Cardiac Cell Culture: A Critical Review of Current Technologies and Applications.* Front Cardiovasc Med, 2019. **6**: p. 87.
29. Eschenhagen, T., et al., *Three-dimensional reconstitution of embryonic cardiomyocytes in a collagen matrix: a new heart muscle model system.* Faseb j, 1997. **11**(8): p. 683-94.
30. Shimizu, I. and T. Minamino, *Physiological and pathological cardiac hypertrophy.* J Mol Cell Cardiol, 2016. **97**: p. 245-62.
31. Marsano, A., et al., *Beating heart on a chip: a novel microfluidic platform to generate functional 3D cardiac microtissues.* Lab Chip, 2016. **16**(3): p. 599-610.
32. Giridharan, G.A., et al., *Microfluidic cardiac cell culture model (μCCCM).* Anal Chem, 2010. **82**(18): p. 7581-7.
33. Nguyen, M.D., et al., *Effects of physiologic mechanical stimulation on embryonic chick cardiomyocytes using a microfluidic cardiac cell culture model.* Anal Chem, 2015. **87**(4): p. 2107-13.
34. Rogers, A.J., V.G. Fast, and P. Sethu, *Biomimetic Cardiac Tissue Model Enables the Adaption of Human Induced Pluripotent Stem Cell Cardiomyocytes to Physiological Hemodynamic Loads.* Anal Chem, 2016. **88**(19): p. 9862-9868.
35. Rogers, A.J., et al., *Cardiac Tissue Chips (CTCs) for Modeling Cardiovascular Disease.* IEEE Trans Biomed Eng, 2019. **66**(12): p. 3436-3443.
36. Hansen, A., et al., *Development of a drug screening platform based on engineered heart tissue.* Circ Res, 2010. **107**(1): p. 35-44.
37. Mannhardt, I., et al., *Human Engineered Heart Tissue: Analysis of Contractile Force.* Stem Cell Rep., 2016. **7**(1): p. 29-42.
38. Breckwoldt, K., et al., *Differentiation of cardiomyocytes and generation of human engineered heart tissue.* Nat Protoc, 2017. **12**(6): p. 1177-1197.
39. Aung, A., et al., *3D cardiac μtissues within a microfluidic device with real-time contractile stress readout.* Lab Chip, 2016. **16**(1): p. 153-62.

40. van Weerd, J.H. and V.M. Christoffels, *The formation and function of the cardiac conduction system.* Development, 2016. **143**(2): p. 197-210.
41. Stephenson, R.S., et al., *High resolution 3-Dimensional imaging of the human cardiac conduction system from microanatomy to mathematical modeling.* Sci Rep, 2017. **7**(1): p. 7188.
42. Protze, S.I., et al., *Sinoatrial node cardiomyocytes derived from human pluripotent cells function as a biological pacemaker.* Nat Biotechnol, 2017. **35**(1): p. 56-68.
43. Zhou, Y.F., et al., *Genetically-engineered mesenchymal stem cells transfected with human HCN1 gene to create cardiac pacemaker cells.* J Int Med Res, 2013. **41**(5): p. 1570-6.
44. Zhang, Y.S., et al., *From cardiac tissue engineering to heart-on-a-chip: beating challenges.* Biomed Mater, 2015. **10**(3): p. 034006.
45. Ronaldson-Bouchard, K., et al., *Advanced maturation of human cardiac tissue grown from pluripotent stem cells.* Nature, 2018. **556**(7700): p. 239-243.
46. Ambrosi, C.M., et al., *Cardiac applications of optogenetics.* Prog Biophys Mol Biol, 2014. **115**(2-3): p. 294-304.
47. Savchenko, A., et al., *Graphene biointerfaces for optical stimulation of cells.* Sci Adv, 2018. **4**(5): p. eaat0351.
48. Tandon, N., et al., *Surface-patterned electrode bioreactor for electrical stimulation.* Lab Chip, 2010. **10**(6): p. 692-700.
49. Ma, Z., et al., *Laser-patterned stem-cell bridges in a cardiac muscle model for on-chip electrical conductivity analyses.* Lab Chip, 2012. **12**(3): p. 566-73.
50. Qian, F., et al., *Simultaneous electrical recording of cardiac electrophysiology and contraction on chip.* Lab Chip, 2017. **17**(10): p. 1732-1739.
51. Kujala, V.J., et al., *Laminar ventricular myocardium on a microelectrode array-based chip.* J Mater Chem B, 2016. **4**(20): p. 3534-3543.
52. Lin, Z.C., et al., *Iridium oxide nanotube electrodes for sensitive and prolonged intracellular measurement of action potentials.* Nat Commun, 2014. **5**: p. 3206.
53. Acker, C.D., P. Yan, and L.M. Loew, *Recent progress in optical voltage-sensor technology and applications to cardiac research: from single cells to whole hearts.* Prog Biophys Mol Biol, 2020. **154**: p. 3-10.
54. Fedele, L. and T. Brand, *The Intrinsic Cardiac Nervous System and Its Role in Cardiac Pacemaking and Conduction.* J Cardiovasc Dev Dis, 2020. **7**(4).
55. Sakai, K., et al., *Functional innervation of human induced pluripotent stem cell-derived cardiomyocytes by co-culture with sympathetic neurons developed using a microtunnel technique.* Biochem Biophys Res Commun, 2017. **494**(1-2): p. 138-143.
56. Oh, Y., et al., *Functional Coupling with Cardiac Muscle Promotes Maturation of hPSC-Derived Sympathetic Neurons.* Cell Stem Cell, 2016. **19**(1): p. 95-106.
57. Kagemoto, T., et al., *Spontaneous oscillatory contraction (SPOC) in cardiomyocytes.* Biophys Rev, 2015. **7**(1): p. 15-24.
58. Viatchenko-Karpinski, S., et al., *Intracellular Ca2+ oscillations drive spontaneous contractions in cardiomyocytes during early development.* Proc Natl Acad Sci U S A, 1999. **96**(14): p. 8259-64.

59. Peter, A.K., M.A. Bjerke, and L.A. Leinwand, *Biology of the cardiac myocyte in heart disease.* Mol Biol Cell, 2016. **27**(14): p. 2149-60.
60. Tanaka, Y., et al., *A micro-spherical heart pump powered by cultured cardiomyocytes.* Lab Chip, 2007. **7**(2): p. 207-12.
61. MacQueen, L.A., et al., *A tissue-engineered scale model of the heart ventricle.* Nat Biomed Eng, 2018. **2**(12): p. 930-941.
62. Shadrin, I.Y., et al., *Cardiopatch platform enables maturation and scale-up of human pluripotent stem cell-derived engineered heart tissues.* Nat Commun, 2017. **8**(1): p. 1825.
63. McMahon, A.P., *Development of the Mammalian Kidney.* Curr Top Dev Biol, 2016. **117**: p. 31-64.
64. Koeppen, B.M. and B.A. Stanton, *Structure and Function of the Kidneys*, in *Renal Physiology*. 2019, Elsevier: Philadelphia, PA, USA.
65. Alkan-Bozkaya, T., et al., *Impact of pulsatile perfusion on clinical outcomes of neonates and infants with complex pathologies undergoing cardiopulmonary bypass procedures.* Artificial organs, 2013. **37**(1): p. 82-86.
66. Verschuren, E.H.J., et al., *Sensing of tubular flow and renal electrolyte transport.* Nat Rev Nephrol, 2020. **16**(6): p. 337-351.
67. Gilmer, G.G., et al., *Flow resistance along the rat renal tubule.* Am J Physiol Renal Physiol, 2018. **315**(5): p. F1398-f1405.
68. Holstein-Rathlou, N.H. and D.J. Marsh, *Oscillations of tubular pressure, flow, and distal chloride concentration in rats.* Am J Physiol, 1989. **256**(6 Pt 2): p. F1007-14.
69. Reinking, L.N. and B. Schmidt-Nielsen, *Peristaltic flow of urine in the renal capillary collecting ducts of hamsters.* Kidney Int, 1981. **20**(1): p. 55-60.
70. Sakai, T., et al., *Fluid waves in renal tubules.* Biophys J, 1986. **50**(5): p. 805-13.
71. Schnermann, J., et al., *Regulation of superficial nephron filtration rate by tubulo-glomerular feedback.* Pflugers Arch, 1970. **318**(2): p. 147-75.
72. Vallon, V., *Tubuloglomerular feedback and the control of glomerular filtration rate.* News Physiol Sci, 2003. **18**: p. 169-74.
73. Weinbaum, S., et al., *Mechanotransduction in the renal tubule.* Am J Physiol Renal Physiol, 2010. **299**(6): p. F1220-36.
74. Sgouralis, I. and A.T. Layton, *Control and modulation of fluid flow in the rat kidney.* Bull Math Biol, 2013. **75**(12): p. 2551-74.
75. Cabral, P.D. and J.L. Garvin, *Luminal flow regulates NO and O2(-) along the nephron.* Am J Physiol Renal Physiol, 2011. **300**(5): p. F1047-53.
76. Loichot, C., et al., *Shear stress modulates vasopressin-induced renal vasoconstriction in rats.* Naunyn Schmiedebergs Arch Pharmacol, 2002. **366**(6): p. 555-61.
77. Jang, K.J., et al., *Human kidney proximal tubule-on-a-chip for drug transport and nephrotoxicity assessment.* Integr Biol (Camb), 2013. **5**(9): p. 1119-29.
78. Astashkina, A.I., et al., *A 3-D organoid kidney culture model engineered for high-throughput nephrotoxicity assays.* Biomaterials, 2012. **33**(18): p. 4700-11.
79. Subramanian, B., et al., *Tissue-engineered three-dimensional in vitro models for normal and diseased kidney.* Tissue Eng Part A, 2010. **16**(9): p. 2821-31.

80. Weber, E.J., et al., *Development of a microphysiological model of human kidney proximal tubule function.* Kidney Int, 2016. **90**(3): p. 627-37.
81. Homan, K.A., et al., *Bioprinting of 3D Convoluted Renal Proximal Tubules on Perfusable Chips.* Sci Rep, 2016. **6**: p. 34845.
82. Lin, N.Y.C., et al., *Renal reabsorption in 3D vascularized proximal tubule models.* Proc Natl Acad Sci U S A, 2019. **116**(12): p. 5399-5404.
83. Rein, J.L., et al., *Effect of luminal flow on doming of mpkCCD cells in a 3D perfusable kidney cortical collecting duct model.* Am J Physiol Cell Physiol, 2020. **319**(1): p. C136-c147.
84. Carrisoza-Gaytan, R., et al., *An unexpected journey: conceptual evolution of mechanoregulated potassium transport in the distal nephron.* Am J Physiol Cell Physiol, 2016. **310**(4): p. C243-59.
85. Palmer, L.G. and J. Schnermann, *Integrated control of Na transport along the nephron.* Clin J Am Soc Nephrol, 2015. **10**(4): p. 676-87.
86. Pearce, D., et al., *Collecting duct principal cell transport processes and their regulation.* Clin J Am Soc Nephrol, 2015. **10**(1): p. 135-46.
87. Roy, A., M.M. Al-bataineh, and N.M. Pastor-Soler, *Collecting duct intercalated cell function and regulation.* Clin J Am Soc Nephrol, 2015. **10**(2): p. 305-24.
88. Musah, S., et al., *Mature induced-pluripotent-stem-cell-derived human podocytes reconstitute kidney glomerular-capillary-wall function on a chip.* Nat Biomed Eng, 2017. **1**.
89. Al-Awqati, Q. and J.A. Oliver, *Stem cells in the kidney.* Kidney Int, 2002. **61**(2): p. 387-95.
90. Saleme, B. and G. Sutendra, *A Similar Metabolic Profile Between the Failing Myocardium and Tumor Could Provide Alternative Therapeutic Targets in Chemotherapy-Induced Cardiotoxicity.* Front Cardiovasc Med, 2018. **5**: p. 61.
91. Morsy, M.S., et al., *Secondary Hyperparathyroidism in Heart Failure.* Am J Med Sci, 2017. **354**(4): p. 335-338.
92. Viravaidya, K., A. Sin, and M.L. Shuler, *Development of a microscale cell culture analog to probe naphthalene toxicity.* Biotechnol Prog, 2004. **20**(1): p. 316-23.
93. McAleer, C.W., et al., *On the potential of in vitro organ-chip models to define temporal pharmacokinetic-pharmacodynamic relationships.* Sci Rep, 2019. **9**(1): p. 9619.
94. Oleaga, C., et al., *Investigation of the effect of hepatic metabolism on off-target cardiotoxicity in a multi-organ human-on-a-chip system.* Biomaterials, 2018. **182**: p. 176-190.
95. Vunjak-Novakovic, G., et al., *HeLiVa platform: integrated heart-liver-vascular systems for drug testing in human health and disease.* Stem Cell Res Ther, 2013. **4 Suppl 1**(Suppl 1): p. S8.
96. Skardal, A., et al., *Multi-tissue interactions in an integrated three-tissue organ-on-a-chip platform.* Sci Rep, 2017. **7**(1): p. 8837.
97. Schimek, K., et al., *Human multi-organ chip co-culture of bronchial lung culture and liver spheroids for substance exposure studies.* Sci Rep, 2020. **10**(1): p. 7865.
98. Maschmeyer, I., et al., *A four-organ-chip for interconnected long-term co-culture of human intestine, liver, skin and kidney equivalents.* Lab Chip, 2015. **15**(12): p. 2688-99.

99. Wagner, I., et al., *A dynamic multi-organ-chip for long-term cultivation and substance testing proven by 3D human liver and skin tissue co-culture.* Lab Chip, 2013. **13**(18): p. 3538-47.
100. Lin, H., et al., *Stem cell-based microphysiological osteochondral system to model tissue response to interleukin-1β.* Mol Pharm, 2014. **11**(7): p. 2203-12.
101. Clark, A.M., et al., *A microphysiological system model of therapy for liver micrometastases.* Exp Biol Med (Maywood), 2014. **239**(9): p. 1170-9.
102. Maschmeyer, I., et al., *Chip-based human liver-intestine and liver-skin co-cultures--A first step toward systemic repeated dose substance testing in vitro.* Eur J Pharm Biopharm, 2015. **95**(Pt A): p. 77-87.
103. Esch, M.B., et al., *Modular, pumpless body-on-a-chip platform for the co-culture of GI tract epithelium and 3D primary liver tissue.* Lab Chip, 2016. **16**(14): p. 2719-29.
104. Moura Rosa, P., et al., *The intercell dynamics of T cells and dendritic cells in a lymph node-on-a-chip flow device.* Lab Chip, 2016. **16**(19): p. 3728-40.
105. Loskill, P., et al., *WAT-on-a-chip: a physiologically relevant microfluidic system incorporating white adipose tissue.* Lab Chip, 2017. **17**(9): p. 1645-1654.
106. Tsamandouras, N., et al., *Integrated Gut and Liver Microphysiological Systems for Quantitative In Vitro Pharmacokinetic Studies.* Aaps j, 2017. **19**(5): p. 1499-1512.
107. Yin, F., et al., *HiPSC-derived multi-organoids-on-chip system for safety assessment of antidepressant drugs.* Lab Chip, 2020.
108. Baert, Y., et al., *A multi-organ-chip co-culture of liver and testis equivalents: a first step toward a systemic male reprotoxicity model.* Hum Reprod, 2020. **35**(5): p. 1029-1044.
109. Pires de Mello, C.P., et al., *Microphysiological heart-liver body-on-a-chip system with a skin mimic for evaluating topical drug delivery.* Lab Chip, 2020. **20**(4): p. 749-759.
110. Kwak, B.S., et al., *Microfluidic skin chip with vasculature for recapitulating the immune response of the skin tissue.* Biotechnol Bioeng, 2020. **117**(6): p. 1853-1863.
111. Sung, J.H., *A body-on-a-chip (BOC) system for studying gut-liver interaction.* Methods Cell Biol, 2020. **158**: p. 1-10.
112. Clark, A.M., N.L. Allbritton, and A. Wells, *Integrative microphysiological tissue systems of cancer metastasis to the liver.* Semin Cancer Biol, 2020.
113. Jeon, J.W., et al., *Three-tissue microphysiological system for studying inflammatory responses in gut-liver Axis.* Biomed Microdevices, 2020. **22**(4): p. 65.
114. Marin, T.M., et al., *An Intestine/Liver Microphysiological System for Drug Pharmacokinetic and Toxicological Assessment.* J Vis Exp, 2020(166).
115. Giordano, L., et al., *Microphysiological Systems to Recapitulate the Gut-Kidney Axis.* Trends Biotechnol, 2021.
116. Benedetto, A., et al., *Spatiotemporal control of gene expression using microfluidics.* Lab Chip, 2014. **14**(7): p. 1336-47.

117. O'Grady, B., et al., *Spatiotemporal control and modeling of morphogen delivery to induce gradient patterning of stem cell differentiation using fluidic channels.* Biomater Sci, 2019. **7**(4): p. 1358-1371.
118. Bhise, N.S., et al., *Organ-on-a-chip platforms for studying drug delivery systems.* J Control Release, 2014. **190**: p. 82-93.
119. Chiriacò, M.S., et al., *Lab-on-Chip for Exosomes and Microvesicles Detection and Characterization.* Sensors (Basel), 2018. **18**(10).
120. Ellis, B.W., et al., *Human iPSC-derived myocardium-on-chip with capillary-like flow for personalized medicine.* Biomicrofluidics, 2017. **11**(2): p. 024105.
121. Menon, N.V., et al., *Micro-engineered perfusable 3D vasculatures for cardiovascular diseases.* Lab Chip, 2017. **17**(17): p. 2960-2968.
122. Griffith, C.K., et al., *Diffusion limits of an in vitro thick prevascularized tissue.* Tissue Eng, 2005. **11**(1-2): p. 257-66.
123. Zandonella, C., *Tissue engineering: The beat goes on.* Nature, 2003. **421**(6926): p. 884-6.
124. Kuo, J.S. and D.T. Chiu, *Controlling mass transport in microfluidic devices.* Annu Rev Anal Chem (Palo Alto Calif), 2011. **4**: p. 275-96.
125. Velve-Casquillas, G., et al., *Microfluidic tools for cell biological research.* Nano Today, 2010. **5**(1): p. 28-47.
126. Zhang, X. and Z. Zhang, *Microfluidic Passive Flow Regulatory Device with an Integrated Check Valve for Enhanced Flow Control.* Micromachines (Basel), 2019. **10**(10).
127. Rogers, A.J., et al., *Hemodynamic Stimulation Using the Biomimetic Cardiac Tissue Model (BCTM) Enhances Maturation of Human Induced Pluripotent Stem Cell-Derived Cardiomyocytes.* Cells Tissues Organs, 2018. **206**(1-2): p. 82-94.
128. Kratz, S.R.A., et al., *Latest Trends in Biosensing for Microphysiological Organs-on-a-Chip and Body-on-a-Chip Systems.* Biosensors (Basel), 2019. **9**(3).
129. Ballini, M., et al., *A 1024-Channel CMOS Microelectrode Array With 26,400 Electrodes for Recording and Stimulation of Electrogenic Cells In Vitro.* IEEE J Solid-State Circuits, 2014. **49**(11): p. 2705-2719.
130. Grosberg, A., et al., *Ensembles of engineered cardiac tissues for physiological and pharmacological study: heart on a chip.* Lab Chip, 2011. **11**(24): p. 4165-73.
131. Sanchez-Bustamante, C.D., et al., *Modulation of cardiomyocyte electrical properties using regulated bone morphogenetic protein-2 expression.* Tissue Eng Part A, 2008. **14**(12): p. 1969-88.
132. Henry, O.Y.F., et al., *Organs-on-chips with integrated electrodes for trans-epithelial electrical resistance (TEER) measurements of human epithelial barrier function.* Lab Chip, 2017. **17**(13): p. 2264-2271.
133. Jones, C.G. and C. Chen, *An arduino-based sensor to measure transendothelial electrical resistance.* Sens. Actuators, A, 2020. **314**: p. 112216.
134. Gaio, N., et al. *A multiwell plate Organ-on-Chip (OOC) device for in-vitro cell culture stimulation and monitoring*. in *2018 IEEE Micro Electro Mechanical Systems (MEMS)*. 2018. IEEE.
135. Liao, Z., et al., *Recent advances in microfluidic chip integrated electronic biosensors for multiplexed detection.* Biosens Bioelectron, 2018. **121**: p. 272-280.

136. Bernard, M., et al., *Biocompatibility of polymer-based biomaterials and medical devices - regulations, in vitro screening and risk-management.* Biomater Sci, 2018. **6**(8): p. 2025-2053.
137. Shirure, V.S. and S.C. George, *Design considerations to minimize the impact of drug absorption in polymer-based organ-on-a-chip platforms.* Lab Chip, 2017. **17**(4): p. 681-690.
138. Torino, S., et al., *PDMS-Based Microfluidic Devices for Cell Culture.* Inventions, 2018. **3**(3): p. 65.

CHAPTER 2

# ACUTE RESPONSE OF ENGINEERED CARDIAC TISSUE TO PRESSURE AND STRETCH

by

LESLIE DONOGHUE, CALEB GRAHAM, AND PALANIAPPAN SETHU

*Cells Tissues Organs.* https://doi.org/10.1159/000525250
Copyright
2022
by
Karger
Used by permission

Format adapted for dissertation

## Highlights

- This chapter describes two unique in vitro model systems that we developed which allows for the evaluation of engineered cardiac tissue constructs to be subjected to conditions of isolated pressure or stretch stimulus.
- Using this system, we showed that engineered cardiac tissue can be acutely exposed to pressure-only and stretch-only conditions to investigate their relative contributions to morphological and biochemical changes in cardiac tissue chips.
- Both conditions elicited an acute phase injury response, which was similar between the two experimental states. Chronic exposure to pressure-only or stretch-only conditions may recreate pathophysiological hallmarks of conditions like pressure overload (PO) and volume overload (VO).

Abstract

The heart is a dynamic organ, and the cardiac tissue experiences changes in pressure and stretch during the cardiac cycle. Existing cell culture and animal models are limited in their capacity to decouple and tune specific hemodynamic stresses implicated in the development of physiological and pathophysiological cardiac tissue remodeling. This study focused on creating a system to subject engineered cardiac tissue to either pressure or stretch stimuli in isolation and the subsequent evaluation of acute tissue remodeling. We developed a cardiac tissue chip containing three-dimensional (3-D) cell-laden hydrogel constructs and cultured them within systems where we could expose them to either pressure changes or volume changes as seen in the left ventricle. Acute cellular remodeling with each condition was qualitatively and quantitatively assessed using histology, immunohistochemistry, gene expression studies, and soluble factor analysis. Using our unique model systems, we isolated the effects of pressure and stretch on engineered cardiac tissue. Our results confirm that both pressure and stretch mediate acute stress responses in the engineered cardiac tissue. However, both experimental conditions elicited a similar acute phase injury response within this timeframe. This study demonstrates our ability to subject engineered cardiac tissue to either pressure or stretch stimuli in isolation, both of which elicited acute tissue remodeling responses.

# 1. Introduction

The heart is a dynamic organ that behaves like a pulsatile pump, undergoing cyclical changes in intracardiac pressure and myocardial stretch due to the contraction and relaxation of cardiomyocytes. The magnitude of these mechanical stresses varies during developmental, healthy, and cardiovascular disease states, and alterations often result in physiological or pathological hypertrophic responses in the heart [1-3]. In general, cardiac hypertrophy is synonymous with increased cardiomyocyte cell size and thus heart mass rather than hyperplasia (i.e., an increase in cell number) [4]. Physiological hypertrophy is associated with development and exercise training, resulting in the maintenance of normal cardiac function or increases in specific functional parameters [5]. In contrast, pathological hypertrophy occurs in the context of disease and is almost always associated with maladaptive myocardial remodeling and dysfunction. Notably, pathological hypertrophy is an adverse response to either Pressure Overload (PO) or Volume Overload (VO). In PO, elevated systemic resistance due to conditions such as hypertension or aortic stenosis results in high left ventricular systolic pressure, resulting in predominantly concentric hypertrophy [6]. The hallmark PO phenotypes include increased extracellular matrix (ECM) deposition and myofibroblast differentiation, as well as cardiomyocytes growing in thickness due to parallel addition of sarcomeres, yielding myocardial wall thickening [7]. In VO, excess left ventricular filling volume due to conditions such as mitral and aortic valve regurgitation and septal defects results in eccentric hypertrophy [8, 9]. This phenotype exhibits wall thinning due to ECM degradation and cardiomyocytes extending in length due to the addition of sarcomeres in series.

Tissue chip models containing engineered cardiac tissue offer advantages in screening cardiotoxic compounds and elucidating mechanisms and signaling pathways

involved in disease development [10]. Since alterations in intraventricular pressure and myocardial stretch play significant roles in cardiovascular disease progression, incorporating these stresses is critical when constructing cardiac tissue chips aimed at modeling different cardiovascular disease states. Several groups have previously investigated the effects of stretch or pressure on cardiac myocytes or fibroblasts in 2D culture but have yet to perform side-by-side comparisons of the acute impact of these stimuli to examine their relative contributions to cardiac remodeling [11-15]. Complex coupled (pressure and stretch) loadings that mimic the cardiac cycle have been investigated previously by our lab and were found to replicate characteristics of clinical pressure and volume overload states [16]. Decoupling these stimuli with in vitro models could help delineate the relative contributions of pressure and stretch in mediating cardiac remodeling and allow for a greater understanding of the roles these stimuli play in normal and disease states. Unlike in animal models where the effects of pressure and stretch cannot be decoupled, in vitro models such as that described below allow for application of either stimulus in isolation. Thus, pressure-only or stretch-only cardiac tissue chips offer a unique ability to study the role of pressure and stretch in propagating physiologic and pathophysiologic cardiac remodeling.

## 2. Materials and Methods

### *2.1 Cardiac Cell Culture Chamber Fabrication*

The cell culture chambers were fabricated using standard soft lithography methods established in our lab [17]. First, polydimethylsiloxane (PDMS) (QSil 216, Quantum Silicones, Richmond, VA, USA) with a base-to-crosslinker ratio of 10:1 was thoroughly mixed, desiccated for 45 minutes to remove any bubbles, and poured into a square mold of 5 cm in length, 5 cm in width, and 1.5 cm in height. The PDMS was cured overnight in a 70 °C oven, and the inner section of the PDMS was cut away to

yield a 3 cm length by 3 cm width square cavity surrounded by a 2 cm frame. This cavity, which is subsequently sealed from below by a flexible membrane, later served as the media reservoir. From a second PDMS slab, six cylindrical posts measuring 1 mm in diameter and 1 cm in height were excised using biopsy punches. For the base of the cardiac device, a flexible membrane was fabricated by spin-coating 10 mL of uncured PDMS on a 78.5 $cm^2$ circular silicon wafer for about 3 s. The PDMS-coated wafer was then placed on a 70 °C hotplate, and the six cylindrical posts were immediately placed on the uncured PDMS using a removable post stencil/guide to ensure proper positioning. Placing the posts before the PDMS membrane was cured allowed secure attachment and positioning. The wafer was then left on the hotplate overnight to cure the post-laden membrane. The final thickness of this PDMS base was 1 mm, and the six posts were oriented into three pairs (two columns within each pair spaced 1 cm apart; each pair spaced 7.5 mm from the next). The post-laden membrane (plus underlying wafer) and square frame were then cleaned and bonded via oxygen plasma treatment (Harrick Plasma Systems, Ithaca, NY, USA) using 700 mTorr of pressure and 45 s of plasma exposure. The bonding created a tight seal to combine the two elements into one PDMS device. Before cell culture use, the underlying silicon wafer was carefully removed, excess PDMS was trimmed, and the device autoclaved for sterilization. The inner chambers were then filled with 2% molten agarose up to 1 mm below the top of the posts, which was then allowed to gel. Dumbbell-shaped troughs were created using a 5 mm-diameter biopsy punch to remove agarose around the posts, and the agarose connecting the paired posts was cut with a scalpel and removed with tweezers. The resulting pattern was three dumbbell-shaped chambers, each serving as a mold for cell-hydrogel seeding. Finally, the PDMS-agarose device

was washed with phosphate-buffered saline (PBS) and warmed in the 37 °C incubator before seeding the cardiac tissue constructs.

*2.2 Cell Culture and Collagen I-Matrigel Hydrogel Encapsulation*

Rat myoblasts and mouse embryonic fibroblasts were purchased from ATCC (H9c2(2-1), ATCC; CRL-1446; MEF (CF-1) SCRC-1040) and cultured in Dulbecco's Modified Eagle's Medium (ATCC; 30-2002) supplemented with 10% Fetal Bovine Serum (FBS) and 2% Non-Essential Amino Acids (Thermo Fisher Scientific; 11140050) in 5% CO2 at 37 °C. H9c2 and MEFs were dissociated once they reached ~85% confluency using 0.25% Trypsin/EDTA (Gibco; 25200-056). Each engineered tissue construct in the device contained approximately $2.8 \times 10^6$ H9c2s and $1.4 \times 10^6$ MEFs resuspended in collagen I via the following method (shown in Fig. 1a). First, 100 μL of 10x PBS and 20 μL 1 N NaOH were added to a small centrifuge tube, vortexed, and then placed on ice. While on the ice, 860 μL of collagen I (Corning; 354236) was added to the PBS-NaOH mixture, vortexed, and quickly returned to the ice. Then 100 μL of Matrigel® (Corning; 354230) was added to the mixture to create a collagen I-Matrigel hydrogel. Following trypsinization and combination of H9c2 and MEFs, the cells were centrifuged for 30 s to form a pellet and the supernatant was aspirated. The 1080 μL of collagen I-Matrigel hydrogel was then added to the cells and pipetted thoroughly to homogenize cell distribution throughout the gel. 250 μL of this suspension was pipetted into each dumbbell chamber. The device was placed into the incubator for 45 mins for gelation, and 3 mL of complete DMEM media was then added to the device's inner reservoir and returned to the incubator overnight. The next day,

the agarose mold was carefully removed, and the media was replenished.

*2.3 Hemodynamic Experimental Setup*

Two hemodynamic setups were designed to expose the engineered tissue constructs to stretch or pressure in isolation, both of which employed a modified version of the Biomimetic Cardiac Tissue Model (BCTM) developed by our lab [16, 18]. In the stretch experiments, the PDMS cardiac tissue chip was sandwiched between a top polycarbonate piece, which bore a 3 × 1 cm oval opening to allow for gas exchange and maintenance of constant atmospheric pressure in the media chamber, and a bottom polycarbonate piece, which had a 3 × 3 × 0.5 cm central cavity connected to a programmable vacuum pump (shown in Fig. 1b). A cylindrical obstacle was also placed in the bottom chamber so that each time vacuum was applied, the flexible membrane would deform around the obstacle, exerting stretches of 0-5% upon the engineered tissue constructs during each cycle (shown in Fig. 1b). The cardiac tissue chip was positioned between two non-deformable polycarbonate pieces for the pressure experiments, and "systolic" pressure (show in Fig. 1c) was created by connecting inlet and outlet ports on the top polycarbonate piece to a programmable pneumatic pump. Each time the pneumatic pump introduced positive pressure to the media chamber, the constructs remained static due to the non-deformable bottom polycarbonate piece. For static, pressure, and stretch conditions, the engineered tissue constructs were each given 3 mL of complete DMEM media contained solely in the PDMS' reservoir.

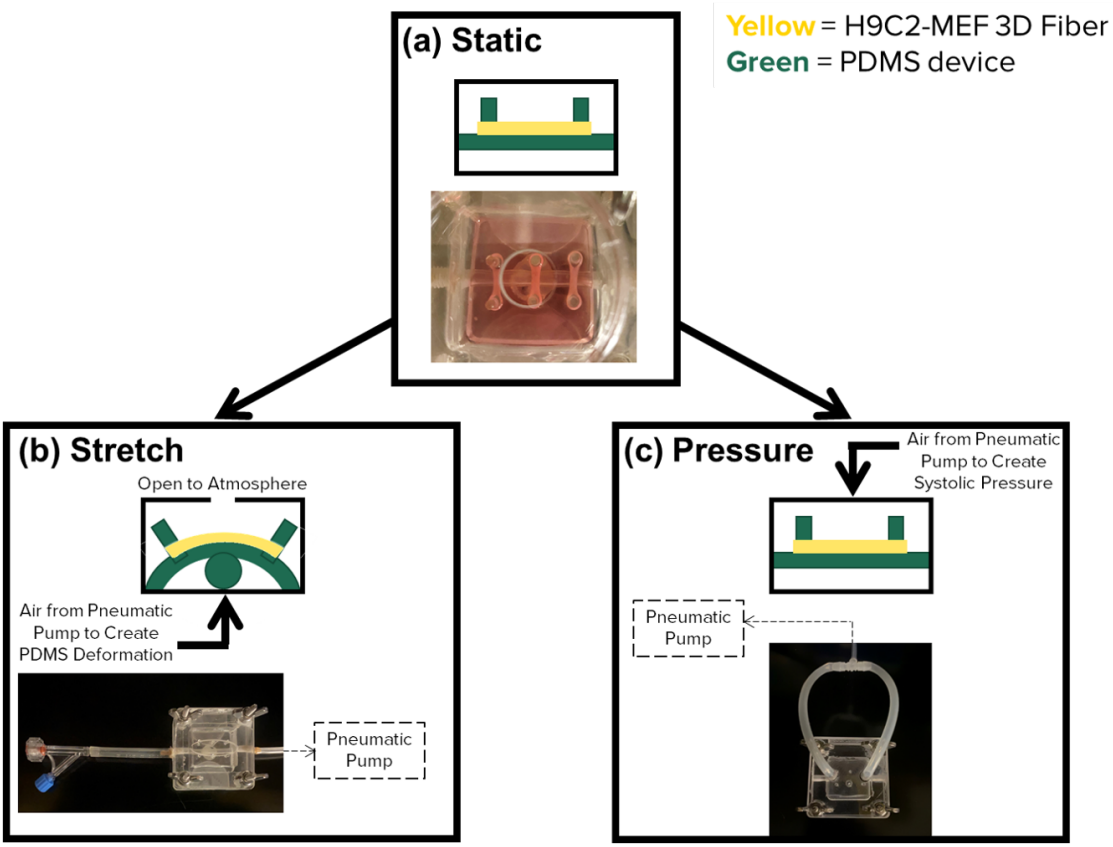


**Figure 1. Overview of 3D Cardiac Tissue Chips.** (a) Engineered constructs, used for all experimental conditions, containing rat myoblasts (H9c2) and mouse embryonic fibroblasts (MEF) within a collagen I-Matrigel hydrogel. Three tissue constructs per PDMS cardiac tissue chip. Static experiments received no external hemodynamic stimuli. (b) The stretch experiments were performed with the PDMS cardiac tissue chip sandwiched between an open-top polycarbonate piece that allows for gas exchange and maintenance of constant atmospheric pressure in the media chamber, and a bottom polycarbonate piece with an open cavity and cylindrical obstacle connected to a programmable pneumatic pump. (c) For the pressure experiments, the cardiac tissue chip was positioned between two non-deformable polycarbonate pieces, and "systolic" pressure was created by connecting inlet and outlet ports on the top polycarbonate piece to a programmable pneumatic pump.

*2.4 Histology and Immunohistochemistry*

On conclusion of the experiments at 24 h, engineered cardiac tissues were fixed with 1:10 buffered formalin (Fisherbrand; 245-684) for 24 h before processing. The formalin-fixed, paraffin-embedded engineered cardiac tissue sections were mounted on glass slides, stained with Hematoxylin and Eosin, Masson's trichrome stain, labeled with Phalloidin (Thermo Fisher Scientific; A34055), or Wheat germ agglutinin (Thermo Fisher Scientific; W11261). Additionally, some slices were immunostained for collagen I using a mouse monoclonal $IgG_1$ antibody (Santa Cruz Biotechnology; sc-59772) and a goat anti-mouse IgG-TR secondary antibody (Santa Cruz Biotechnology; sc-2781). Nuclei were stained using DAPI for all fluorescent stains.

*2.5 RT-qPCR*

After 24 hr of stimulation, the engineered cardiac tissues were flash-frozen and maintained at -80 °C until processing. Samples were first bead milled (BeadBug; D1030) in tubes containing 0.5 mm zirconium beads (Benchmark; D1032-05) for 40 s. The total RNA was isolated using the RNeasy® Plus Mini kit (Qiagen; 74134) as directed by the manufacturer protocol, and 2 μg of this total RNA was used to obtain cDNA for mRNAs using a High-Capacity cDNA Reverse Transcription Kit (Applied Biosystems; 4368814) as directed by the manufacturer protocol. Mouse primers were designed to target the following genes: TIMP-1, TIMP-2, TIMP-3, Col1α1, αSMA, MMP-2, MMP-3, and MMP-9 with their primer sequences located in the Supplemental Table. The quantitative real-time PCR utilized 5 ng synthesized cDNA in 1 μL, 5 μL of 2X Fast SYBR Green Master Mix (Applied Biosystems; 4385612), 0.5 μL forward and 0.5 μL reverse primers (both at 10 μM), and 3 μL nuclease free water were combined (total 10 μL) and pipetted into each well of a 384 well PCR plate. The plate was placed into a BioRad 4000 Real-Time PCR system using the following cycling conditions: 95

°C denaturation for 10 min, 40 cycles of amplification (95 °C denaturation for 15 s, and 60 °C annealing for 30 s, 72 °C extension for 30 s). Melting curves were used to monitor genomic contamination. For negative controls, SYBR Green-primer reactions were performed without cDNA. The obtained Cq values were normalized to mouse 18s rRNA expression levels and fold changes were calculated using the $2^{-\Delta\Delta C_T}$ method [19].

*2.6 Soluble Factor Analysis*

Media was collected after 24 hours of hemodynamic stimulation, frozen at -20 °C for storage, and later shipped on dry ice to Eve Technologies (Calgary, AB, Canada). Two arrays were conducted: Mouse Cytokine Array, TGF-β 3-Plex (TGF β1-3) and Mouse MMP Discovery Array 5-plex for Cell Culture and non-blood samples (MDMMP-C,O). TGFβ 1-3 measured TGFβ 1, 2, 3. MDMMP-C,O measured MMP-2, MMP-3, MMP-8, proMMP-9, and MMP-12. Each experiment was independently completed three times to produce triplicates of each cell culture media condition. Only soluble factors with detectable concentration or statistical significance were illustrated and discussed.

*2.7 Statistical Analysis*

All data are expressed as mean ±SEM. Statistical significance was evaluated with one-way ANOVA for comparison among ≥3 means with Prism 5 (GraphPad Software Inc). Values of $p < 0.05$ were considered to be statistically significant.

## 3. Results

### *3.1 Generation of Decoupled Pressure and Stretch*

Using our modified setups, we generated three unique experimental conditions (shown in Fig. 1). As detailed in Table 1, the static controls were maintained at atmospheric pressure with 0% stretch. The pressure only samples experienced cycles of pressure varying between peak "systolic" pressure of 140 mmHg and "diastolic" pressure of 0 mmHg and a stretch of 0% delivered at a frequency of 80 cycles per minute. The stretch-only samples experienced atmospheric pressure and time varying strain of 0-5% at an 80 cycles per minute frequency.

**Table 1:** Parameters for Experimental Setups.

| Condition | Pressure, mmHg | Stretch, % | Frequency, cycles/min |
|---|---|---|---|
| Static | – | – | 0 |
| Pressure | 40 | – | 80 |
| | 90 | – | 80 |
| | 140 | – | 80 |
| Stretch | – | 0.5 | 80 |
| | – | 2.5 | 80 |
| | – | 5 | 80 |

### *3.2 Tissue Morphology and Organization*

Tissue constructs maintained under static, pressure-only, and stretch-only conditions were evaluated for cellular morphology, changes in cell numbers and cell size, organization, and alignment using fluorescence microscopy and histology. Immunofluorescent staining for collagen 1α1 showed similar upregulation in both the pressure and stretch conditions compared to static controls (shown in Fig. 2a).

Cytoskeletal organization of F-actin filaments was visualized using Phalloidin staining and showed that both the pressure and stretch conditions resulted in more stress fiber development than the static controls (shown in Fig. 2b). Evaluation of cell size and shape using wheat germ agglutinin (WGA) suggested that acute exposure to pressure and stretch may not significantly increase cell size compared to static controls (shown in Fig. 2c).

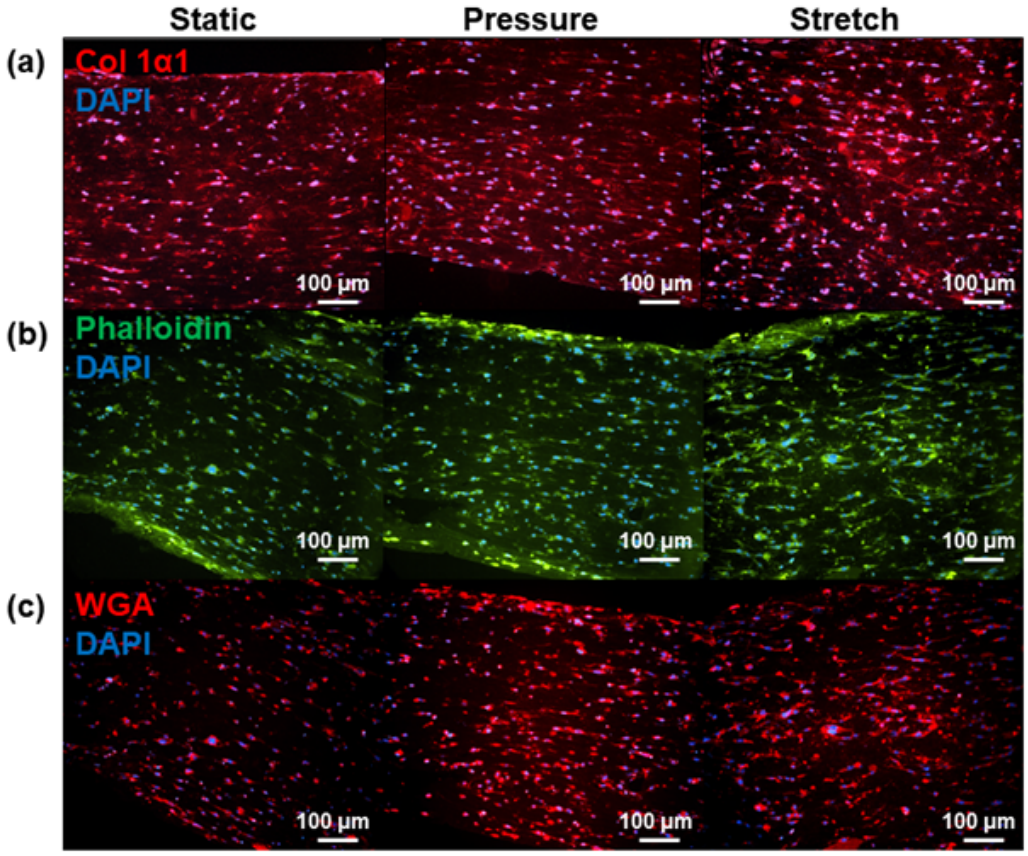


**Figure 2. Immunofluorescence microscopy of Engineered Constructs Following Static, Pressure, or Stretch Stimuli for 24 hours.** (a) Collagen 1α1 staining demonstrated upregulated deposition in dynamic conditions. (b) Cytoskeletal microfilament F-actin was evaluated using Phalloidin staining and appeared to be upregulated in both pressure and stretch. (c) Wheat Germ Agglutinin (WGA) staining

indicated increased cell number in the hemodynamic experiments. (Scale 100 μm). Static (n = 5), Pressure (n = 9), Stretch (n = 9).

Visualization of cell numbers via staining of the nuclei using DAPI indicated that both pressure and stretch were associated with slightly higher cell densities in comparison to static controls (shown in Fig. 2a-c). In these dynamic environments, the cells typically experience greater media perfusion, increasing viability and proliferation.

The H&E staining revealed cell alignment and homogeneous cell distributions in all three conditions without any distinguishable differences (shown in Fig. 3a). In addition to immunofluorescent labeling, collagen deposition was determined using Masson's trichrome staining (shown in Fig. 3b). Our results indicated that both dynamic conditions were associated with higher collagen deposition levels than static controls, similar to that observed with Col 1α1 immunohistochemistry.

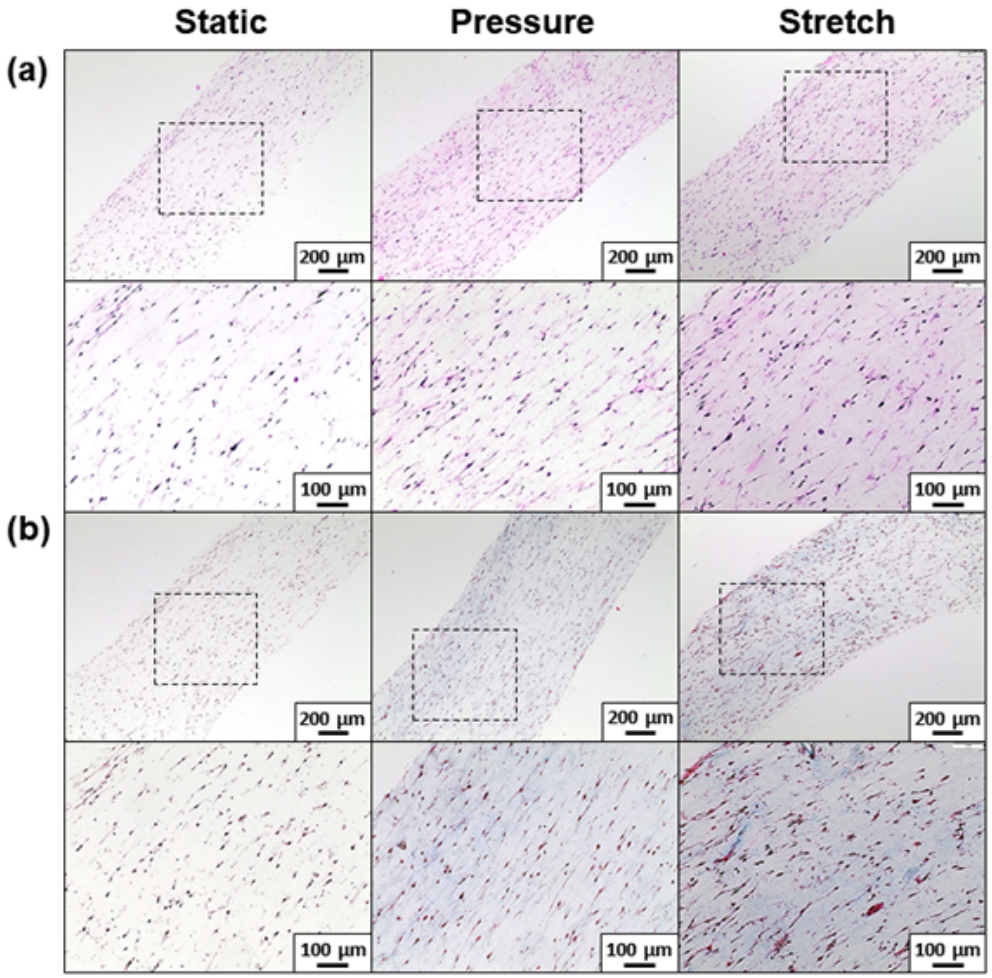


**Figure 4. Tissue Morphology and Alignment**. (a) H&E staining of paraffin embedded tissue sections showed alignment and uniform distribution of H9c2 and MEF cells within the constructs in all experimental conditions. (b) Masson's Trichrome staining indicated greater collagen density in pressure and stretch conditions than static controls. (Scale: Top = 200 µm, Bottom = 100 µm). Static (n = 5), Pressure (n = 9), Stretch (n = 9).

*3.3 Gene Expression Profiling*

The choice of gene targets for this study was partially influenced by the results of previous studies in our lab, which showed that PO and VO led to upregulation of genes whose products mediate matrix remodeling [16]. In the present study, no

statistically significant alterations in gene expression were seen in either experimental group compared to the static controls, perhaps due to the brief time frame of the experiments. However, general trends were observed (shown in Fig. 4).

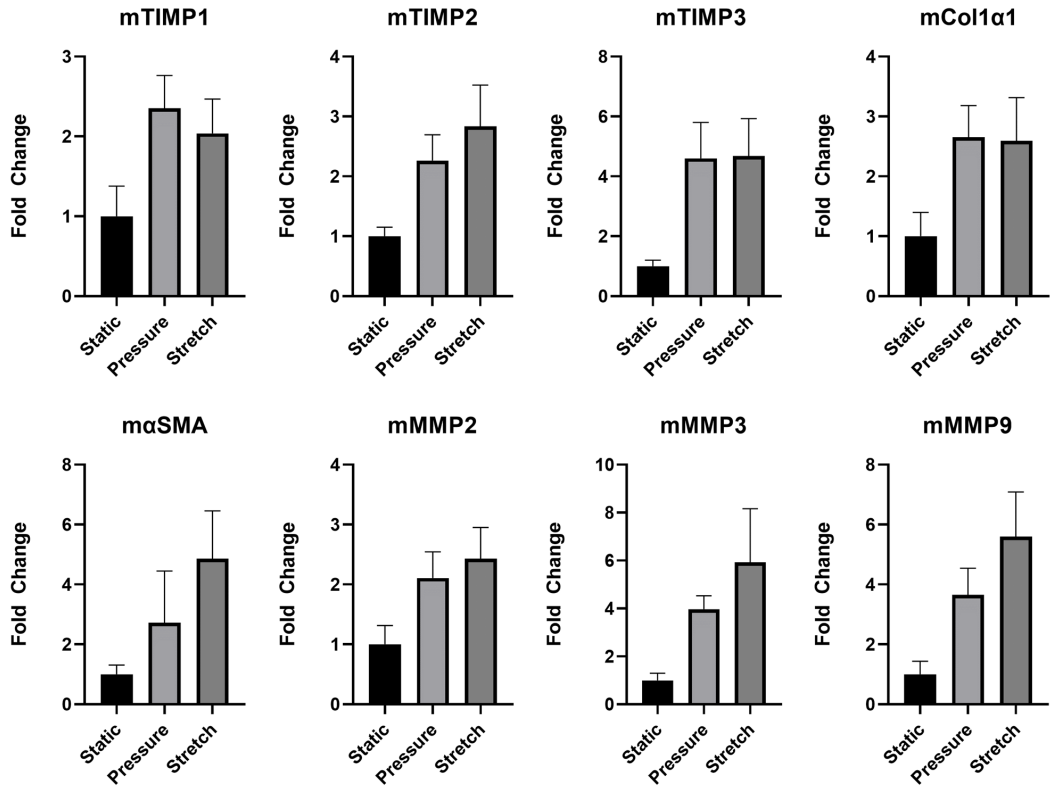


**Figure 4. Molecular Characterization of Engineered Cardiac Tissues**. Total RNA from control (static) and pressure and stretch cardiac tissue fibers were isolated, and RT-qPCR analyzed transcript expression quantities. Means (± SEM) of TIMP1, TIMP 2, TIMP3, Col1α1, αSMA, MMP2, MMP3, and MMP9 transcript expression levels were comparable in pressure and stretch conditions and both upregulated compared to static controls. Static (n = 5), Pressure (n = 8), Stretch (n = 8).

First, both pressure and stretch conditions elicited a ~2-fold increase in Col 1α1 expression. Evaluation of alpha-smooth muscle actin (αSMA) showed that stretch constructs had an approximately 5-fold increase in αSMA compared to static, whereas pressure led to a 2-fold increase. Evaluation of matrix metalloproteinases (MMPs) and tissue inhibitors of metalloproteinases (TIMPs) demonstrated an approximately 6-fold increase of MMP-3 and MMP-9 with stretch and 4-fold increase with pressure in comparison to the static controls. TIMP-1, TIMP-2, TIMP-3, and MMP levels were elevated in both pressure and stretch constructs compared to static controls. TIMP-3 expression levels were not discernible between pressure and stretch, while MMP-2 and TIMP-2 were slightly elevated in stretch versus pressure. Conversely, the pressure was associated with slightly greater upregulation of TIMP-1 than stretch.

*3.4 Soluble Factor Analysis*

Cytokine arrays that were used in this study enabled the detection of known mediators of matrix remodeling, inflammation, and angiogenesis in the culture media (shown in Fig. 5). Regarding the matrix metalloproteinases, MMP-3 demonstrated statistically significant upregulation in constructs exposed to dynamic stretch compared to both static controls and pressure constructs, similar to the gene expression trend. MMP-12 was significantly decreased in pressure constructs compared to stretch, and TGFβ3 demonstrated a similar expression pattern. In general, inflammatory cytokines findings were inconsistent.

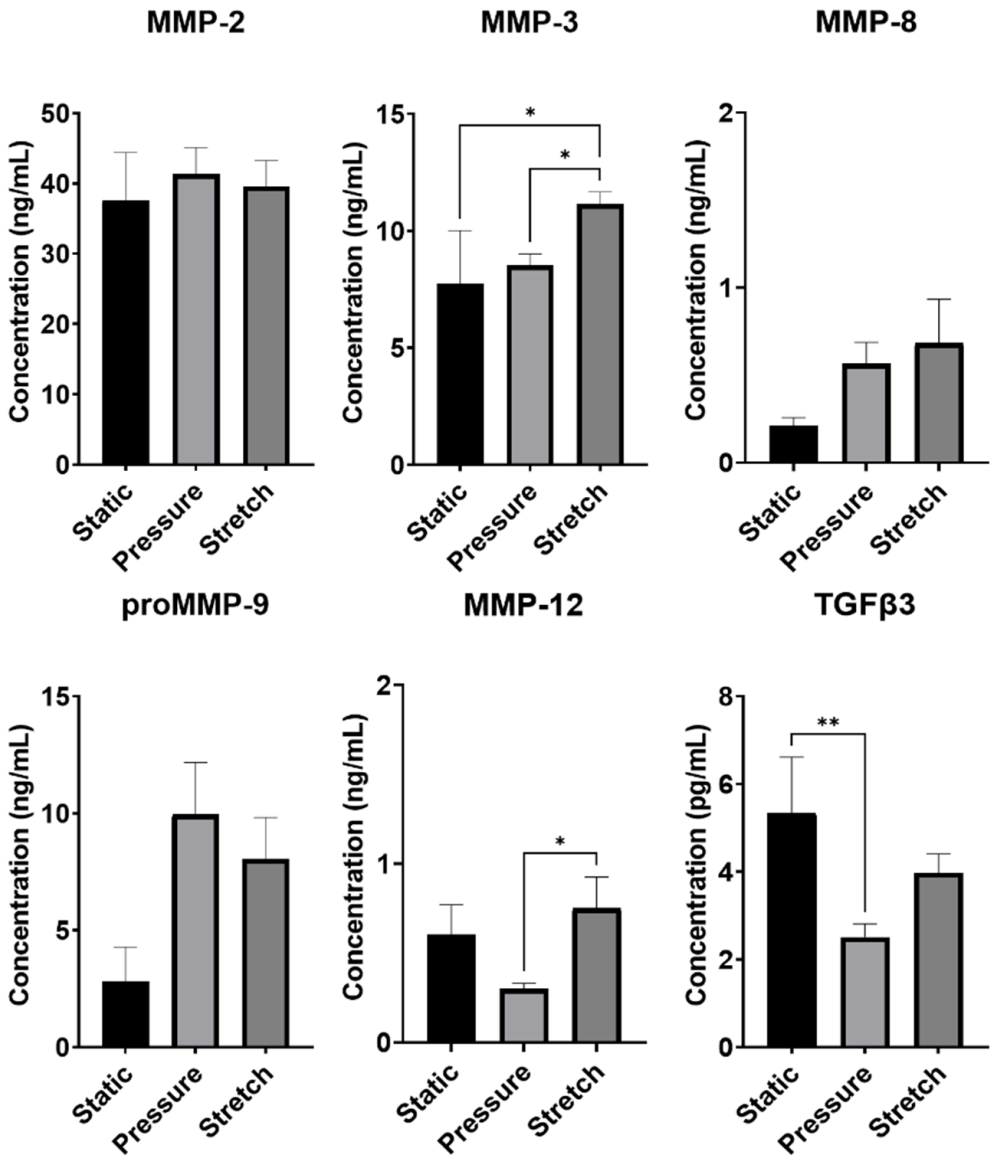


**Figure 5. Soluble Factor Analysis.** Means (± SEM) of MMP2, MMP3, and MMP8, proMMP9, MMP12, and TGFβ3 of matrix remodeling cytokines (pg/mL and ng/mL) in perfusing media for engineered constructs cultured under control (static), pressure, or stretch conditions. Statistical analyses by one-way ANOVA, *$p < 0.05$, **$p < 0.005$. Static (n = 3), Pressure (n = 9), Stretch (n = 9).

# 4. Discussion

The heart is a dynamic organ that cyclically contracts and relaxes to pump blood throughout the body. With each cardiac cycle, the cells that make up the heart wall experience alterations in pressure and stretch. These mechanical stresses serve as signal inputs for feedback mechanisms that ensure proper heart function acutely through modulation of heart rate, contractile force, and vascular tone, and chronically through cardiac remodeling. Changes in these stimuli within physiological limits, such as those seen during exercise, can lead to physiological remodeling of the heart depending upon the frequency and duration of the increased stresses, resulting in a slight increase in organ size and improvement in cardiac function [20, 21]. In almost any type of cardiovascular dysfunction, extrinsic or intrinsic factors cause intraventricular pressure and/or cardiac wall stretch to shift from physiological to pathological levels, eventually leading to adverse, rather than compensatory, cardiac tissue remodeling. Specifically, in PO, cardiomyocytes become thicker via the addition of sarcomeres in parallel and cardiac fibrosis often develops, both of which contribute to increased wall thickness, oxidative stress, and arrhythmias, which can lead to sudden death [21-24]. In contrast, cardiomyocytes subjected to VO conditions become thinner and longer due to addition of sarcomeres in series, and chronically volume overloaded hearts demonstrate heightened ECM degradation and myofibrillar disorganization [22]. Both PO and VO are also associated with contractile dysfunction, activation of fetal gene programs, metabolic switch from fatty acid oxidation to glycolysis, electrophysiological dysfunction, and increased oxidative stress [3].

In intact organisms, pressure and stretch in the heart are coupled and cannot be evaluated in isolation. However, as exemplified by the present study, in vitro models can study the effects of pressure or stretch alone. In this study, we engineered two

unique platforms to study the impact of pressure or stretch in isolation on engineered cardiac tissue. In both dynamic conditions, the engineered tissues were subjected to 80 cycles per minute, as this falls within normal heart rate range for adult humans [25]. 140 mmHg of pressure, which falls within the range of maximal left ventricular pressures in healthy adults, was applied to the engineered tissues in the pressure studies [26]. Though the 5% strain achieved in the stretch condition falls below the estimated 19% experienced by myocytes in healthy adult hearts [27], the authors felt this was sufficient to elicit any stretch-induced cell remodeling phenomena. Using this platform, we sought to (a) characterize how engineered cardiac tissue responds to isolated acute stimulation with pressure or stretch, (b) determine if the responses were distinct, and (c) compare how the acute phase response to pressure or stretch in isolation compares to morphological and gene expression changes associated with chronic PO and VO.

As mentioned earlier, PO and VO are associated with adverse tissue remodeling. Specifically, PO results in increased fibrosis, whereas VO frequently results in excessive ECM degradation and tissue thinning [28-30]. Since alterations to the ECM play significant roles in PO- and VO-associated pathological cardiac tissue remodeling, we tailored our evaluation of gene expression changes and analysis of soluble factors to assay proteins that either play direct roles in ECM remodeling or indicative of a fibrotic phenotype. Both MMPs and TIMPs are widely recognized for their roles in mediating matrix remodeling in cardiac disease states [22]. MMP classes with myocardial remodeling relevance include collagenases (MMP-1), stromelysins (MMP-3), gelatinases (MMP-9 and MMP-2), and the membrane-type MMPs [31].

Our gene expression results showed that collagen 1α1 was upregulated in pressure and stretch compared to static controls, and this finding was also reflected by our histological and immunohistology analyses (shown in Fig. 4). The progression of

cardiac hypertrophy in response to chronic hemodynamic overload stimulates cardiac fibroblasts to undergo a phenotypic switch to become contractile myofibroblasts, cells that express abundant smooth muscle alpha-actin (α-SMA) through the Rho signaling pathway [32-34]. Similar to collagen 1α1, upregulation of α-SMA expression was observed in stimulated constructs compared to static controls.

In summary, we were able to devise platforms that allowed for applying pressure or stretch in isolation to engineered cardiac tissue constructs and demonstrate that engineered tissue constructs respond to isolated pressure and stretch stimuli via changes in structure, gene expression, and soluble factor production. Though the experimental conditions led to unique responses, the majority were not statistically significant and differed from those seen in chronic PO or VO. Due to the short time course of these experiments and the uncoupled nature with which pressure and stretch were applied, it is not surprising that the findings do not align with those from clinical scenarios. These results suggest that acute exposure to pressure-only or stretch-only conditions elicit an acute injury response from the engineered cardiac tissue, which may not clearly distinguish pressure from stretch; however, we believe that chronic exposure to pressure-only or stretch-only conditions would enable adaptive changes past the acute injury response which would more closely resemble changes seen with chronic PO and VO.

Overall, the gene expression data suggest the cells within the engineered constructs are sensitive to the applied stimuli, as indicated by the upregulation of genes associated with ventricular remodeling in both experimental conditions compared to the static control. While both pressure and stretch stimuli elicited responses in similar genes in most cases, the magnitude of the gene expression changes and soluble factor concentrations were different.

Moving forward with these bioengineered constructs and experimental hemodynamic systems, it would be worthwhile to repeat this study over a more extended time period. Within 24 hours, we observed morphological, gene expression, and soluble factors changes; however, many were not statistically relevant. Furthermore, many of the cardiac phenotypes associated with PO and VO result from prolonged cardiovascular disease. In addition to prolonging the duration of future studies, applying higher amounts of pressure and stretch to the engineered tissues would likely elicit more dramatic changes. Faithful recapitulation of the onset of cardiovascular disease is a fundamental challenge in in vitro models due to limitations in current cell culture and tissue engineering technologies. Alternatively, combining ex vivo cardiac tissue with the hemodynamic systems utilized here could provide another avenue for investigating the acute effects of pressure and volume overload on the healthy heart. In summary, our pressure-only and stretch-only cardiac tissue chips system was valuable in investigating the roles of pressure and stretch in mediating physiologic and pathophysiologic cardiac remodeling.

## 5. Conclusion

In conclusion, we developed a unique in vitro model system that allows for the evaluation of engineered tissue constructs under conditions of isolated pressure or stretch stimuli. Using this system, we showed that engineered cardiac tissue can be acutely exposed to pressure-only and stretch-only conditions. Both conditions elicited an acute phase injury response, which was similar between the two experimental states. Chronic exposure to pressure-only or stretch-only conditions may recreate pathophysiological hallmarks of PO and VO.

Reference:


1. Clark, E.B., et al., *Ventricular function and morphology in chick embryo from stages 18 to 29.* Am. J. Physiol. - Heart Circ. Physiol., 1986. **250**(3): p. H407-H413.
2. Clark, E.B. and N. Hu, *Hemodynamics of the developing cardiovascular system.* Ann. N. Y. Acad. Sci., 1990. **588**(1): p. 41-47.
3. Mann, D.L., *Basic mechanisms of left ventricular remodeling: the contribution of wall stress.* J Card Fail, 2004. **10**(6): p. S202-S206.
4. Diwan, A. and G.W. Dorn, *Decompensation of cardiac hypertrophy: cellular mechanisms and novel therapeutic targets.* Physiology, 2007. **22**(1): p. 56-64.
5. Donoghue, L., et al., *Tissue Chips and Microphysiological Systems for Disease Modeling and Drug Testing.* Micromachines, 2021. **12**(2).
6. Grossman, W., D. Jones, and L. McLaurin, *Wall stress and patterns of hypertrophy in the human left ventricle.* J Clin Invest, 1975. **56**(1): p. 56-64.
7. Kong, P., P. Christia, and N.G. Frangogiannis, *The pathogenesis of cardiac fibrosis.* Cell Mol Life Sci, 2014. **71**(4): p. 549-574.
8. Hutchinson, K.R., J.A. Stewart Jr, and P.A. Lucchesi, *Extracellular matrix remodeling during the progression of volume overload-induced heart failure.* J Mol Cell Cardiol, 2010. **48**(3): p. 564-569.
9. Carabello, B.A., *Concentric versus eccentric remodeling.* J Card Fail, 2002. **8**(6 Suppl): p. S258-63.
10. Chan, A.H.P. and N.F. Huang, *Engineering Cardiovascular Tissue Chips for Disease Modeling and Drug Screening Applications.* Front Bioeng Biotechnol, 2021. **9**: p. 673212.
11. Lee, A.A., et al., *Differential responses of adult cardiac fibroblasts to in vitro biaxial strain patterns.* J Mol Cell Cardiol, 1999. **31**(10): p. 1833-1843.
12. Nguyen, M.-D., et al., *Cardiac cell culture model as a left ventricle mimic for cardiac tissue generation.* Anal Chem, 2013. **85**(18): p. 8773-8779.
13. Nguyen, M.-D., et al., *Effects of physiologic mechanical stimulation on embryonic chick cardiomyocytes using a microfluidic cardiac cell culture model.* Anal Chem, 2015. **87**(4): p. 2107-2113.
14. De Jong, A.M., et al., *Cyclical stretch induces structural changes in atrial myocytes.* J Cell Mol Med, 2013. **17**(6): p. 743-753.
15. Herum, K.M., et al., *Mechanical regulation of cardiac fibroblast profibrotic phenotypes.* Mol Biol Cell, 2017. **28**(14): p. 1871-1882.
16. Rogers, A.J., et al., *Cardiac Tissue Chips (CTCs) for Modeling Cardiovascular Disease.* IEEE Trans Biomed Eng, 2019. **66**(12): p. 3436-3443.
17. Nguyen, K.T., et al., *Acute response of human aortic endothelial cells to loss of pulsatility as seen during cardiopulmonary bypass.* Cells Tissues Organs, 2022. **211**(3): p. 1-11.
18. Rogers, A.J., et al., *Hemodynamic stimulation using the biomimetic cardiac tissue model (BCTM) enhances maturation of human induced pluripotent stem cell-derived cardiomyocytes.* Cells Tissues Organs, 2018. **206**(1-2): p. 82-94.
19. Livak, K.J. and T.D. Schmittgen, *Analysis of relative gene expression data using real-time quantitative PCR and the 2(-Delta Delta C(T)) Method.* Methods, 2001. **25**(4): p. 402-8.
20. Fagard, R., *Athlete's heart.* Heart, 2003. **89**(12): p. 1455-1461.

21. Vega, R.B., et al., *Molecular mechanisms underlying cardiac adaptation to exercise.* Cell Metab, 2017. **25**(5): p. 1012-1026.
22. Spinale, F.G., *Myocardial matrix remodeling and the matrix metalloproteinases: influence on cardiac form and function.* Physiol Rev, 2007. **87**(4): p. 1285-1342.
23. Harvey, P.A. and L.A. Leinwand, *Cellular mechanisms of cardiomyopathy.* J Cell Biol, 2011. **194**(3): p. 355-365.
24. Takimoto, E. and D.A. Kass, *Role of oxidative stress in cardiac hypertrophy and remodeling.* Hypertension, 2007. **49**(2): p. 241-248.
25. Bonnemeier, H., et al., *Circadian profile of cardiac autonomic nervous modulation in healthy subjects: differing effects of aging and gender on heart rate variability.* Journal of cardiovascular electrophysiology, 2003. **14**(8): p. 791-799.
26. Bahraseman, H.G., et al., *Estimation of maximum intraventricular pressure: a three-dimensional fluid–structure interaction model.* BioMedical Engineering OnLine, 2013. **12**(1): p. 122.
27. Wang, V.Y., et al., *Image-Based Investigation of Human in Vivo Myofibre Strain.* IEEE Transactions on Medical Imaging, 2016. **35**(11): p. 2486-2496.
28. Eghbali, M., *Cardiac fibroblasts: function, regulation of gene expression, and phenotypic modulation.* Basic Res Cardiol, 1992. **87 Suppl 2**: p. 183-9.
29. MacKenna, D., S.R. Summerour, and F.J. Villarreal, *Role of mechanical factors in modulating cardiac fibroblast function and extracellular matrix synthesis.* Cardiovasc Res, 2000. **46**(2): p. 257-263.
30. Nicoletti, A. and J.B. Michel, *Cardiac fibrosis and inflammation: interaction with hemodynamic and hormonal factors.* Cardiovasc Res, 1999. **41**(3): p. 532-43.
31. Mann, D.L. and F.G. Spinale, *Activation of matrix metalloproteinases in the failing human heart: breaking the tie that binds.* Circulation, 1998. **98**(17): p. 1699-1702.
32. Black, F.M., et al., *The vascular smooth muscle alpha-actin gene is reactivated during cardiac hypertrophy provoked by load.* J Clin Invest, 1991. **88**(5): p. 1581-8.
33. Leslie, K.O., et al., *Cardiac myofibroblasts express alpha smooth muscle actin during right ventricular pressure overload in the rabbit.* Am J Pathol, 1991. **139**(1): p. 207-16.
34. Zhao, X.-H., et al., *Force activates smooth muscle α-actin promoter activity through the Rho signaling pathway.* J Cell Sci, 2007. **120**(10): p. 1801-1809.

# CHAPTER 3

# PROINFLAMMATORY AND PROFIBROTIC PROFILES OF HUMAN RENAL PROXIMAL EPITHELIAL CELLS IN RESPONSE TO DRUGS AND FLUIDIC SHEAR STRESS

by

LESLIE DONOGHUE, ARUSHI KOTRU, IAN BERG, EMMA STEVENSON, AND PALANIAPPAN SETHU

In preparation for journal submission

Format adapted for dissertation

Specific Aim 1:

To test the hypothesis that our 2D RPTC containing human renal proximal tubule cells (hRPTEC-hTERT) cultured under physiologic shear and pressure will differ from static controls in their relative nephrotoxic responses. We will utilize drugs classified based on their nephrotoxic risk (high and low) and evaluate nephrotoxicity through quantitative and/or non-invasive assessments.

Abstract

The current pathway for drug discovery is associated with costs of $2.55 billion and between 10-15 years of development for a single drug to reach the market. The challenges in predicting drug toxicities and efficacies are attributed to inherent species differences in drug-metabolizing enzyme activities and cell-type-specific sensitivities to toxicants. Organs-on-a-chip are an emerging technology in disease modeling and screening therapeutics to address discrepancies between animal models and human clinical trials. They utilize tissue engineering, fluid mechanics, and biomaterials to replicate complex organs and tissues' in vivo architectures and functions. The renal proximal tubule (PT) in vivo is exposed to fluid flow and mechanical stress (pressure, stretch, shear), and these stimuli play an important role in maintaining cellular phenotype and homeostasis. Currently, available prototypes fail to replicate the in vivo environment because they often fail to mimic the physiological forces. Therefore, these models have had limited success in predicting drug-induced nephrotoxicity. In this study, we bioengineered and evaluated a dynamic platform of the PT and studied the effects of drugs and tubular dysfunction to establish its potential for translational research. Human renal proximal tubule cells (hRPTEC-hTERT) cultured under a spectrum of physiological fluidic shear (static controls, low shear 0.1 dynes/cm$^2$, and high shear 1.0 dynes/cm$^2$) were evaluated for shear alteration using qualitative immunofluorescence for morphological changes and transcriptomic analysis of 758 targets via a Nanostring gene expression panel. Shear and drug alteration responses were evaluated using forty-eight cytokine panels and viability through lactase dehydrogenase assays. Drugs were classified based on their nephrotoxic risk (high, intermediate, and low), and the platform aimed to incorporate noninvasive

readouts to reflect cellular function and viability. Results indicate 117 significantly up or down-regulated genes between the conditions and identified shear-sensitive proinflammatory and profibrotic cytokines, transcription factors, and growth factors in the in vitro human proximal tubule epithelium. Together, this study allowed for a more thorough investigation of drug compounds and shear to help determine accurate pharmacological and pathological responses and to determine the utility of in vitro perfusion models.

# 1. Introduction

Off-target effects of pharmaceutical drugs account for approximately 20% of all patients diagnosed with acute renal failure [1]. Patients today are older, have higher incidences of diabetes, obesity, and cardiovascular disease, and take multiple medications to manage their conditions. Therefore, they are at higher risk of exposure to drugs and treatments that may prove nephrotoxic [2]. Between 1990 and 2010, fourteen drugs were withdrawn from the market due to their nephrotoxicity [3]. It may be necessary to evaluate drug-induced nephrotoxicity early during the drug discovery cycle to avoid such scenarios and prevent drugs that have off-target effects from advancing past pre-clinical testing to late-stage clinical trials. Screening will help ensure drug safety and minimize the costs associated with drug failure in late-stage clinical trials or after the drug is on the market [1].

Drugs exert nephrotoxic effects via different mechanisms, including altered glomerular hemodynamics, tubular cell toxicity, inflammation, and crystal nephropathy. Therefore, it is important to understand the specific mechanism of renal injury to recognize and prevent drug-induced renal dysfunction. PT epithelial cells are particularly vulnerable to the toxic effects of drugs as they are involved in the concentration and reabsorption of glomerular filtrate, exposing them to high levels of circulating toxins. These cells are rich in mitochondria to generate the energy required for the PT's transporters and receptors, making them sensitive to oxidative stress, forming free radicals, or interferences with tubular transport [4, 5]. This study categorized drugs based on the nephrotoxic effects and relative PT damage. "Low": drugs that are not harmful to the kidney; "Intermediate": drugs

that are considered damaging to other parts of the kidney (glomerulus, distal tubule); “High”; direct PT toxicity or damage via a secondary mechanism such as crystal formation. We utilized Human renal proximal tubule cells (hPTEC-hTERT1) as they are immortalized through the stable expression of the catalytic subunit of human telomerase reverse transcriptase (hTERT) and readily prevent mesenchymal-epithelial transition [6]. These cells have been well characterized to retain the functional properties of primary cells while maintaining consistent expression levels of functional markers over several passages [7]. Furthermore, the static culture of hPTEC-hTERT1 was initially evaluated via lactase dehydrogenase release and transepithelial electrical resistance to establish appropriate in vitro concentrations of drugs with our desired type. Non-invasive measurements are a more favorable assay choice for tissue chip models to evaluate drug toxicity to monitor time-dependent measurements. Human cytokine arrays were incorporated in this study to investigate tubular cell viability, reduction in barrier function, and analysis of pro-inflammatory, pro-apoptotic soluble factors in the culture medium. Lastly, invasive readouts such as transcriptomic Nanostring assessed the effects of a spectrum of fluidic shear stress (i.e., static 0 dyne/cm$^2$, low shear 0.1 dyne/cm$^2$, and high shear 1.0 dyne/cm$^2$) for over 700 gene targets.

As discussed in Chapter 1, current efforts to evaluate drug-induced nephrotoxicity utilize various kidney cell types and manufacturing techniques [8]. However, the shear stress range on PT cells and the associated contribution to cellular pharmacokinetics response are poorly understood. Shear stress is a critical tissue chip (TC) component that emulates the physiological forces in vivo. However, existing models have not investigated the spectrum of shear conditions within models in their ability to screen therapeutics. This

chapter examines the importance of shear stress in ensuring an accurate in-vivo –like tubular epithelial phenotype and the importance of that phenotype in accurately predicting drug-induced nephrotoxicity.

## 2. Materials and Methods

### *2.1 Planar Proximal Tubule Device Fabrication*

The cell culture chambers were fabricated using standard soft lithography methods established in our lab [9]. First, polydimethylsiloxane (PDMS) (QSil 216, Quantum Silicones, Richmond, VA, USA) with a base-to-crosslinker ratio of 10:1 was thoroughly mixed and desiccated for 45 min to remove any bubbles. A negative replica mold of the cell culture chamber was created using a laser-cut nylon sheet of the cell culture chamber adhered to a glass and perimeter acrylic base. Uncured PDMS was placed into an initial model and cured overnight in a 70°C oven. The device was removed and placed in an oxygen plasma treatment (Harrick Plasma Systems, Ithaca, NY, USA) under 700 mTorr of pressure and 60 s of plasma exposure. Following protocols described by Kim et al., the device was placed in a room-temperature (RT) methanol bath and vacuum desiccated for at least 1 hour to allow for passivation [10]. The passivated PDMS was then incorporated into a new mold with the passivated devices face-up and submerged into approximately 150 g of wet PDMS. The devices were cured overnight at RT instead of an oven, as a prolonged period of heat will negate the passivation of the devices. Once cured, the placeholder devices were removed, and the negative mold followed the same protocol of oxygen plasma and subsequent methanol treatment. Following passivation, the mold is ready to create the desired devices. 16-gauge syringe needles were placed in the mold's inlet and outlet channels to ultimately create holes for the tubing fasteners. Wet, uncured

PDMS was placed in the mold to surround the syringe needles and cured at RT overnight. Next, the syringe needles were removed, and the desired channel PDMS devices were gently removed from the passivated PDMS mold using a thin spatula. These PDMS devices were then cleaned and bonded to a standard glass slide (7.5 cm length x 2.5 cm width x 1 mm depth) via oxygen plasma treatment using 700 mTorr of pressure and 45 s of plasma exposure. The bonding created a tight seal surrounding the cell culture chamber. From this point on, the devices were constructed one of two ways. For perfusion devices, Polypropylene 1.6 mm barbed tube ID luer lock couplings were added to the inlet and outlet holes created via the 16-gauge syringe needles and sealed with 0.5 mL of wet PDMS on each end to prevent leaks. For static culture devices, 5 mL luer lock syringes with the plunger removed and 1.6 mm ID luer lock couplings attached were used as media reservoirs, attached to inlet and outlet holes, and sealed with PDMS. Before cell culture use, the devices were autoclaved for sterilization.

*2.2 Cell Culture and Collagen-IV*

Human renal proximal tubule cells (hPTEC-hTERT1) were purchased from ATCC (RPTEC/TERT1, ATCC; CRL-4031) and cultured in Dulbecco's Modified Eagle's Medium: F-12 (ATCC, 30-2006) supplemented with hTERT Immortalized RPTEC growth kit (ATCC; ACS-4007) in 5% CO2 at 37°C according to the manufacturer's protocols. The day before cell seeding, the entirety of the channel volume (150 µL) was filled with PBS and Collagen IV (Corning, 354233) at 8 $\mu g/cm^2$ to enhance cell adhesion. The devices were placed at 4°C overnight to ensure an even coating of basement membranous extracellular matrix, Collagen IV [11]. Approximately 90% confluent hRPTEC-hTERT1 were dissociated using 0.05% trypsin/EDTA (Gibco, 25200-054). The PBS-Collagen IV mixture

was carefully removed, and $1 \times 10^6$ cells suspended in 150 µL were seeded into each device's channel and returned to the incubator. After approximately 45 minutes, the cells began to adhere to the channel and were maintained in culture overnight in an incubator with 5% CO2 at 37°C.

*2.3 Perfusion Experimental Setup*

Each device had an independent perfusion system or "loop" setup to ensure controlled experiment parameters. A single loop consisted of silicone tubing of equal lengths and tube fittings, a media reservoir containing precisely 6 mL of media, connection to a 6-channel MP2 Micro Peristaltic Pump (ESI, Golden, CO), associated pump-stop tubing, a one-way valve ahead of the device to minimize potential bubbles, and a tubing outlet to a 3D printed reservoir cap to recirculate media. Between 12-14 experimental loops were run simultaneously via two 6-channel and one 2-channel peristaltic pump to achieve sufficient throughput for the various drugs and shear conditions. Experimental setup parameters were established using pressure and flow sensors and were set to <10 mmHg and either 0.1 dyne/cm$^2$ for the low shear conditions or 1.0 dyne/cm$^2$ for the high shear conditions. The loop components were sterilized using ethylene oxide sterilization overnight to prevent contamination. Furthermore, the loops were assembled in a cell culture hood under sterile conditions, primed first with DPBS(-) to flush the systems of air, and then with F:12-hTERT cell culture media supplemented with 1% antibiotic-antimycotic supplement. Devices were then transferred to each loop system and placed at a slight angle on the inlet side to prevent any potential bubbles from being trapped within the tissue chip. Once all loop assemblies circulated with media, they were transferred to a large incubator and maintained in culture under conditions of 5% $CO_2$ at 37°C.

*2.4 Computational Fluid Dynamics*

The magnitude and distribution of shear stress across the devices at the relevant flow rates were estimated using computational fluid dynamics (CFD) modeling software. Using the device's Autodesk Inventor CAD model, a finite element mesh of the channel fluid domain was generated using Gmsh [12]. Mesh refinement was increased at all boundaries to account for steep velocity gradients. This mesh was imported into FeBio, which was used to set up, execute, and analyze the CFD model [13]. All device walls were assigned a no-slip boundary condition, and the outlet was assigned a zero fluid dilation boundary condition. At the inlet, the flow was implemented by assigning a prescribed velocity calculated from the desired flow rate. The fluid (cell culture media) was modeled as water at 37°C, a Newtonian fluid with a density of 1000 kg/m$^3$, bulk modulus of 2.1 GPa, and shear viscosity of 0.00069 Pa*s.

*2.5 Immunofluorescence (IF)*

For LIVE/DEAD® (Invitrogen, L3224) staining, devices were imaged immediately after 48 hours of shear stress to evaluate cell viability. For the remaining devices, hPTEC-hTERT1s within the tissue chip were fixed with 4% paraformaldehyde in PBS for 20 mins and washed with DPBS(-) 3X 5 mins. Devices stained for F-actin phalloidin (Invitrogen, A12379) were permeabilized with 0.5% Triton X-100 (Fisher Scientific, Fair Lawn, NJ, USA) for 10 min at room temperature, whereas devices intended for occludin (Invitrogen, OC-3F10), E-cadherin (Cell Signaling Technology, 24E10), and α-Tubulin were permeabilized for 10 mins at room temperature with 0.1% Tween 20 (Sigma, P1379), a milder detergent used for cell membrane proteins. Devices were washed with DPBS(-) 3X 5 mins and later blocked for nonspecific binding using DPBS(-) containing 2% BSA at 4°C

overnight. The next day, the devices were washed, and primary antibodies were diluted 1:200 with antibody dilution buffer containing 0.1% Tween 20 and 2% BSA and incubated overnight at 4°C. On the final day, they were washed, and the secondary goat anti-rabbit IgG Texas Red (Invitrogen, T-2767) was diluted to 4 μg/mL using a dilution buffer and incubated at room temperature for 2 hr in the dark (note: occludin stain skipped this step as it contained a conjugated primary antibody). Finally, VECTASHIELD DAPI (Vector Lab., CA, USA) was added, and the cells were imaged using a Nikon Eclipse TE2000-U epifluorescence microscope (Nikon Instrument Inc., USA).

*2.5 RNA Isolation and Sample Preparation for Nanostring*

After 48 hr of exposure to fluidic shear stress, the devices containing hPTEC-hTERT1 were immediately lysed using the lysis buffer from the RNeasy® Plus Mini kit (Qiagen; 74134) by repetitively pipetting the lysis buffer within the device. The total RNA was isolated using the Qiagen kit as directed by the manufacturer's protocol to yield, on average, 3.4 μg of total RNA per device with an average 260/280 and 260/230 purity ratios of 2.05 and 2.04, respectively. RNA samples were stored at −80 °C until further use. Subsequent hybridization steps were performed overnight at the Nanostring Laboratory in the Department of Radiation Oncology at UAB using the nCounter Analysis System by Nanostring Technologies (Seattle, WA). The pre-constructed gene panel chosen for this study was the nCounter® Human Organ Transplant Panel containing 770 genes for its overlap of targets pertinent to the nephrotoxicity in the proximal tubule and cytokine array in section 2.11. Gene expression was normalized using twelve housekeeper genes within the panel.

*2.6 ROSALIND® Nanostring Gene Expression Methods*

Datasets were analyzed by ROSALIND® (https://rosalind.bio/), with a HyperScale architecture developed by ROSALIND, Inc. (San Diego, CA). Read Distribution percentages, violin plots, identity heatmaps, and sample MDS plots were generated as part of the QC step. Normalization, fold changes and p-values were calculated using criteria provided by Nanostring. ROSALIND® follows the nCounter® Advanced Analysis protocol of dividing counts within a lane by the geometric mean of the normalizer probes from the same lane. Housekeeping probes to be used for normalization are selected based on the geNorm algorithm as implemented in the NormqPCR R library [14]. The abundance of various cell populations was calculated on ROSALIND using the Nanostring Cell Type Profiling Module. ROSALIND performs a filtering of Cell Type Profiling Module to include results that have scores with a p-value less than or equal to 0.05. Fold changes and p-values are calculated using the fast method described in the nCounter® Advanced Analysis 2.0 User Manual. P-value adjustment is performed using the Benjamini-Hochberg method of estimating false discovery rates (FDR). Clustering of genes for the final heatmap of differentially expressed genes was done using the Partitioning Around Medoids (PAM ) method using the fpc R library that considers the direction and type of all signals on a pathway, the position, role, and type of every gene, etc. [15]. Hypergeometric distribution was used to analyze the enrichment of pathways, gene ontology, domain structure, and other ontologies. The topGO R library was used to determine local similarities and dependencies between GO terms in order to perform Elim pruning correction [16]. Several database sources were referenced for enrichment analysis, including Interpro, NCBI,

MSigDB, REACTOME, WikiPathways [17-22]. Enrichment was calculated relative to a set of background genes relevant to the experiment.

*2.7 Principal Component Analysis (PCA)*

To better understand the distinct shear profiles from the Nanostring data, the multivariate technique of Principal Component Analysis (PCA) was performed to reduce the dimensionality of a dataset while retaining as much of the variation in the data as possible [23-26]. Using R programming software and methods to standardize data, i.e., subtracting the mean and dividing by the standard deviation, the variables could move forward on the same scale. Next, the covariance matrix was calculated to show the relationships between all variables in the dataset using the "cov()" function in R. The third step was to calculate the eigenvalues and eigenvectors of the covariance matrix using the "eigen()" function in R. Eigenvalues represent the amount of variance explained by each principal component. In contrast, eigenvectors represent the direction of each principal component. Next, the principal components were calculated by multiplying the standardized data by the eigenvectors. The intended result gives linear combinations of the original variables that capture as much of the variation in the data as possible. Finally, the amount of variance explained by each principal component and loading coefficients were graphed to visualize the eigenvalues and determine how many principal components to retain.

*2.8 Drug Nephrotoxicity Concentrations and Lactase Dehydrogenase (LDH) Cytotoxicity Analyses*

Preliminary nephrotoxicity assessments of P3 hPTEC-hTERT1 cells with drugs with known low toxicity, dexamethasone and probenecid, and high toxicity, gentamicin

and cisplatin, were evaluated using the CyQUANT™ LDH Cytotoxicity Assay (Invitrogen, C20300) colorimetric kit as directed by the manufacturer defined protocols. Absorbance at 490 nm and 680 nm was recorded using a SpectraMax i3x MiniMax 300 (Molecular Devices, San Jose, CA). Percent viability was calculated by the following equation:

$$\%Viability = 1 - \%Cytotoxicity$$

$$= 1 - \frac{Compound - treated\ LDH\ activity - spontaneous\ LDH\ activity}{Maximum\ LDH\ activity - Spontaneous\ LDH\ activity} \times 100.$$

The cells were in contact with the drugs for 24 hours at varying concentrations to determine in vitro drug concentration toxicities. Following exposure to drugs under perfusion, LDH cytotoxicity was assessed using the same colorimetric kit and reader. Frozen media samples were thawed at room temperature and used after the first thaw cycle to minimize protein degradation.

*2.9 Transepithelial Electrical Resistance (TEER)*

Five Transwell® Permeable 12 mm insert, 12 well plates with 0.4 µm polyester membranes (Costar, 3460) were used to observe the transepithelial electrical resistance (TEER) between the inner hPTEC-hTERT1 monolayer and the outer well containing F12:TERT cell media. An EVOM2 Epithelial Volt/Ohm TEER Meter (World Precision Instruments) with STX2 electrodes was used to measure and display approximate hPTEC-hTERT1 resistance. Blank wells (with media but no cells) were used as a control resistance measurement. After at least seven days of stable resistance achieved following the establishment of confluent monolayers of contact-inhibited hPTEC-hTERT1, the drugs Cisplatin (Sigma, P4394), dexamethasone (Sigma, D4902), and probenecid (Sigma, P8761) were reconstituted via manufacturers guidelines and added to the “basolateral” outside well of the plates. The TEER plates with drugs and corresponding DPBS(-) vehicle

controls were measured daily for an additional seven days, with media and drug changes every other day. Final resistance measurements were first subtracted by the blank media wells measurements and then normalized to the cell surface area of the membrane to yield resistance in the units $\Omega * cm^2$.

*2.10 NGAL ELISA*

ELISA kit (Biotechne, Catalog #DY008) was used for NGAL/lipocalin Solid Phase Sandwich ELISA. The capture antibody was diluted to the recommended working concentration in PBS. A 96-well microplate was loaded with 100 µL per well of the diluted capture antibody. The plate was sealed and left to incubate overnight at room temperature. The next day, each well was aspirated and washed 3X with 300 µL of wash buffer. After the third wash, the remaining wash buffer was removed by inverting the plate and blotting it against a Kimtech wipe. Next, the plate was blocked by adding 300 µL of reagent diluent to each well. The plate was sealed and incubated at room temperature for one hour before repeating the three wash steps. Then, a 1:2 serial dilution of the standard to reagent diluent was added to the standard wells to obtain NGAL concentrations of 5000, 2500, 1250, 625, 312.5, 156.25, and 78.125 pg/mL. The remaining plate wells contained 100 µL of frozen media samples thawed at room temperature and used after the first thaw cycle to minimize protein degradation. The plate was sealed and incubated at room temperature for 2 hours before another washing procedure. Following the third wash, 100 µL of the diluted streptavidin-HRP was added to each well. The plate was sealed and left to incubate at room temperature for 20 minutes away from direct light. After 20 minutes, the 3X wash steps were repeated, and 100 µL of the substrate solution was sealed and left to incubate at room temperature for 20 minutes away from direct light. After 20 minutes, 50 µL of stop solution

was added to each plate and immediately placed into a SpectraMax i3x MiniMax 300 (Molecular Devices, San Jose, CA) Imaging Cytometer for reading. The light source was set to 450 nm with wavelength correction set to 540 nm. The final optical density was obtained by subtracting the 540 nm absorbance from the readings at 450 nm. Concentrations were then extrapolated from the standard curve using a four-parameter logistic (4-PL) in GraphPad Prism software. The results of these experiments are shown in the supplement.

*2.11 Soluble Factor Analysis*

A 500 µL cell culture media sample was collected every 12 hours from every static and loop device. The multiplexing analysis was performed using the Luminex™ 200 system (Luminex, Austin, TX, USA) by Eve Technologies Corp. (Calgary, Alberta). Forty-eight markers were simultaneously measured in the samples using Eve Technologies' Human Cytokine Panel A 48-Plex Discovery Assay® (MilliporeSigma, Burlington, Massachusetts, USA) according to the manufacturer's protocol. The 48-plex consisted of sCD40L, EGF, Eotaxin, FGF-2, FLT-3 Ligand, Fractalkine, G-CSF, GM-CSF, GROα, IFN-α2, IFN-γ, IL-1α, IL-1β, IL-1RA, IL-2, IL-3, IL-4, IL-5, IL-6, IL-7, IL-8, IL-9, IL-10, IL-12(p40), IL-12(p70), IL-13, IL-15, IL-17A, IL-17E/IL-25, IL-17F, IL-18, IL-22, IL-27, IP-10, MCP-1, MCP-3, M-CSF, MDC, MIG/CXCL9, MIP-1α, MIP-1β, PDGF-AA, PDGF-AB/BB, RANTES, TGFα, TNF-α, TNF-β, and VEGF-A. Assay sensitivities of these markers range from 0.14 – 50.78 pg/mL for the 48-plex. Individual analyte sensitivity values are available in the MILLIPLEX® MAP protocol.

*2.12 Statistical Analysis*

All data are expressed as mean ± SD. The statistical significance of gene expression data was evaluated with one-way ANOVA with Bonferroni posthoc analysis, whereas cytokine arrays were evaluated with two-way ANOVA with Tukey posthoc analysis for comparison among ≥3 means with Prism 9 (GraphPad Software Inc). Values of $p < 0.05$ were considered to be statistically significant.

## 3. Results

### *3.1 Device Design and Perfusion Parameters to Evaluate Shear Stresses to hRPTEC-hTERT1 Cells*

As shear stress was the main objective of this study, it was important to eliminate non-laminar and heterogenous flow patterns to ensure the maximum amount of homogenous shear stress that the hRPTEC-hTERT1 would experience. To accomplish this, the design for the 2D tissue chip was kept a simple straight channel large enough to ensure quantifiable protein alteration could be detected (Figure 1A) and small enough to minimize materials and allow a greater number of devices to run simultaneously (Figure 1B-C). Experiments were typically run between 12 to 14 devices in parallel to yield sufficient throughput, with the number of micro-peristaltic pump channels being the limiting factor. Furthermore, shear stresses of 0.1 dyne/cm$^2$ and 1.0 dyne/cm$^2$ were validated via computational fluid dynamics to assess homogenous shear stress to the cells (Figure 1D). Some variance in shear stress is present around the inlet and outlet channels, which is to be expected. The appropriate fluid velocities were determined to be 32 µL/min and 327 µL/min for low and high shear conditions, respectively. Collagen IV, the most predominant ECM protein in the basement membrane for hRPTEC-hTERT1s, helped maximize cell attachment and enable cell survival under perfusion. Lastly, the experimental protocol was

designed to account for cells to acclimate to the flow conditions before the administration of drugs (Figure 1E).

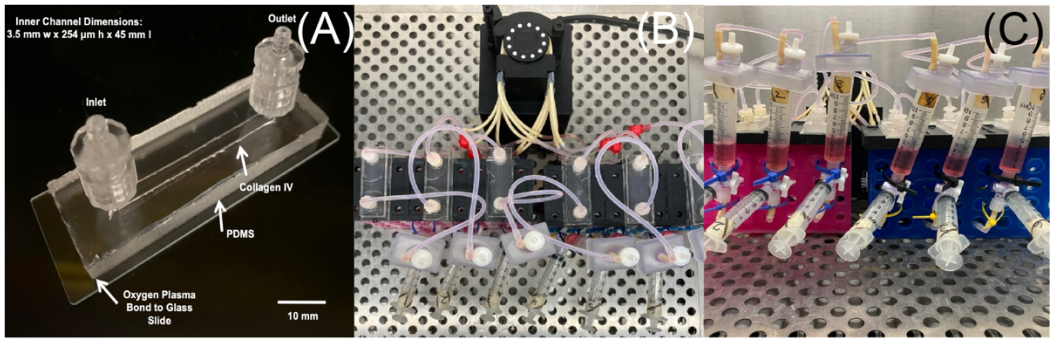


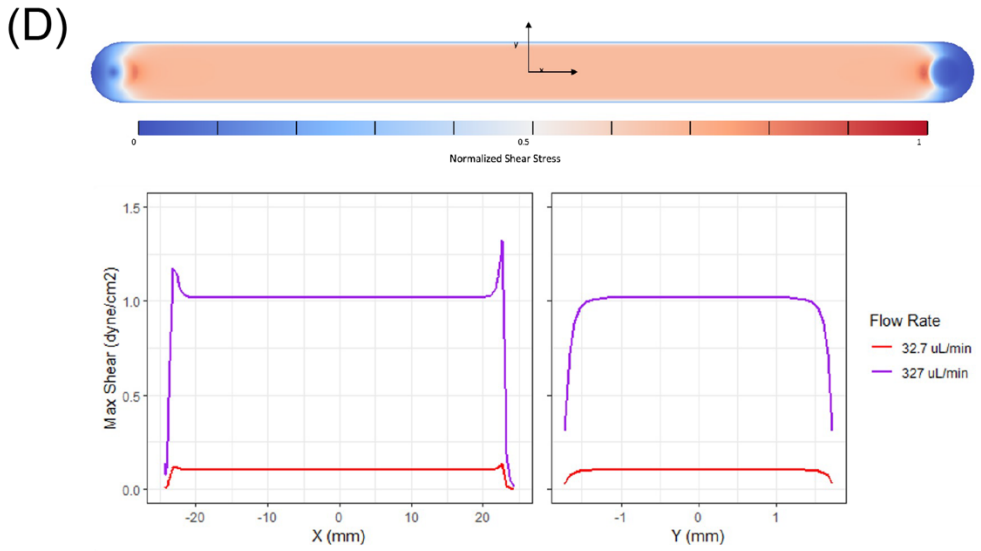


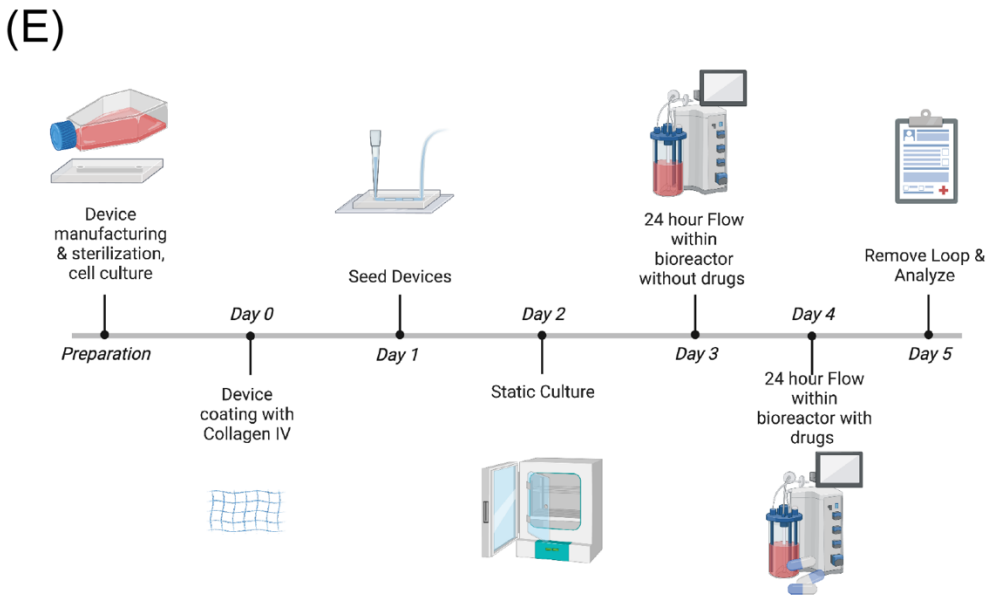

**Figure 1. Device Design and Perfusion Parameters.** (A) PDMS device containing a straight channel (dimensions of 45 mm x 3.5 mm x 254 μm) was utilized to assess flow alterations. Perfusion experiment with six devices visualized (top view, B) with media sampling ports (side view, C). (D) FEBio computation fluid dynamic rendering equates 32 and 327 μL/min fluid velocities to the low and high shear stresses of 0.1 and 1 dynes/cm$^{2,}$ respectively. (E) Overview of experimental protocol and time course.

*3.2 Fluid Flow Promotes Expression of Functional and Structural Markers of hRPTEC-hTERT1s when Compared to Culture in Static Conditions*

Using IF, the viability and structural and functional markers of hRPTEC-hTERT1s were analyzed at both 48 hours of static culture and 48 hours under flow (Figure 2A). The viability of cells under conditions of flow was determined to be comparable to the cells cultured under static conditions (2B). Cytoskeletal microfilament F-actin was visible in both static and flow (0.1 dyne/cm$^2$ depicted in Figure 2), but flow induced a more compact morphology and greater and more uniform expression across the cell volume (Figure 2C). Expression of tight junction marker occludin and adherens junction marker E-Cadherin were more strongly expressed at cell-cell junctions under flow conditions. Cells under shear conditions also appeared to attain a cobblestone morphology (Figures 2D-E). Transporters in the cell membrane, such as the water transporter aquaporin-1 (AQP1) more greatly expressed under flow conditions. Lastly, the polarization of hRPTEC-hTERT1 determined that the expression of primary cilia through acetylated tubulin was also enhanced under flow conditions.

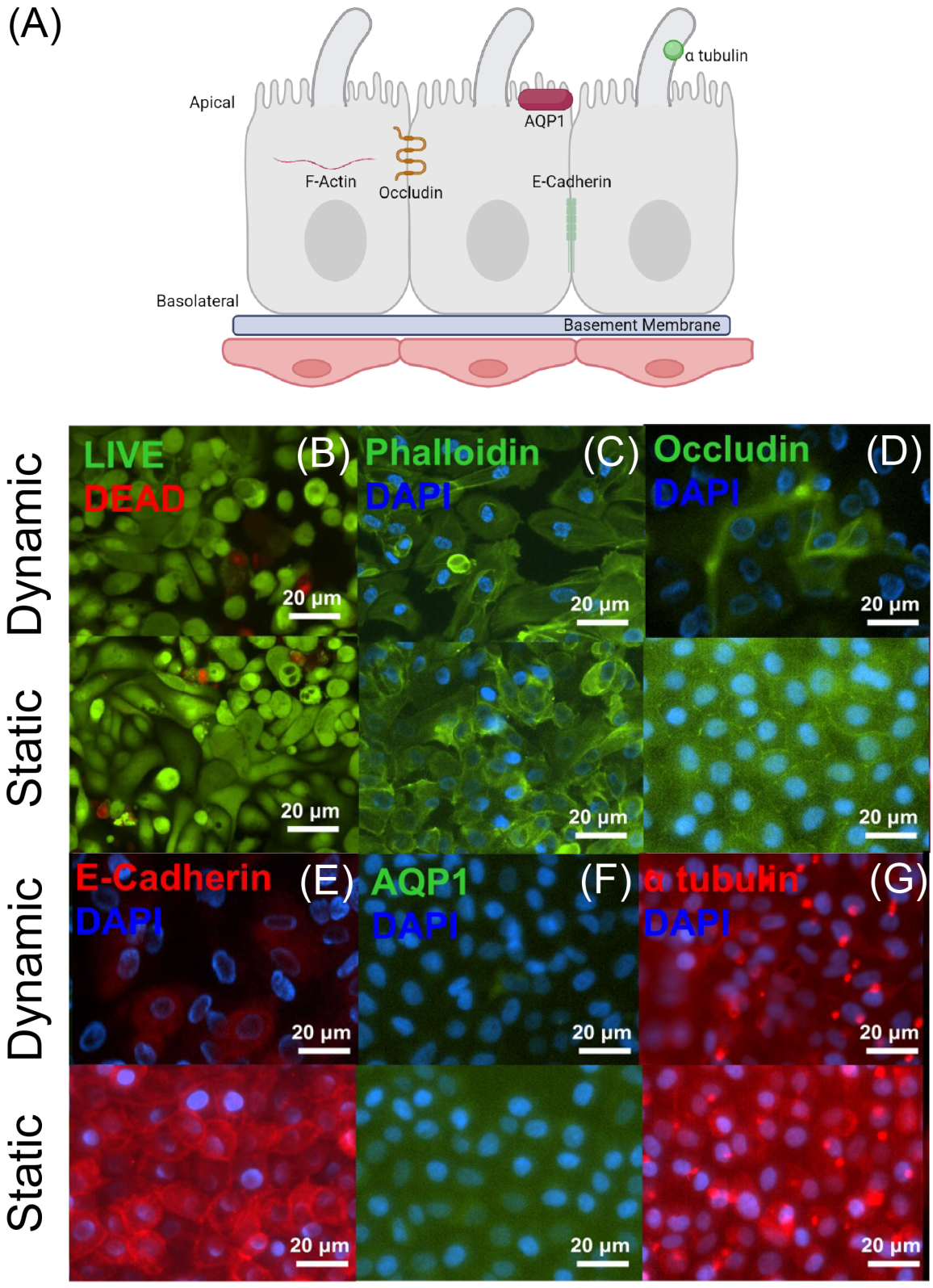
(A)
Apical
α tubulin
AQP1
F-Actin
Occludin
E-Cadherin
Basolateral
Basement Membrane
Dynamic
Static
LIVE
DEAD
(B)
Phalloidin
DAPI
(C)
Occludin
DAPI
(D)
E-Cadherin
DAPI
(E)
AQP1
DAPI
(F)
α tubulin
DAPI
(G)
20 μm

**Figure 2. Immunofluorescence Microscopy of hRPTEC-hTERT1s Grown in Either Static or Dynamic Physiological Shear Stress Conditions.** (A) Cellular location of imaged proteins, (B) viability was maintained and demonstrated using a LIVE/DEAD®, (C) cell cytoskeleton F-actin with Phalloidin, (D) greater expression of tight junction protein occludin, (E) adhesion protein E-cadherin, (F) water channel protein AQP1, and (G) microtubule α-tubulin cilia architecture in static and perfused devices (n=6).

*3.3 Nanostring and Principal Component Analysis Show Distinct Gene Expression Profiles Between Static, Low Shear, and High Shear Conditions*

The Nanostring array evaluated a total of 758 genes. ROSALIND Meta-Analysis detected 117 statistically significant genes amongst all groups (Figure 3). The greatest difference was detected between static and low conditions, with 101 genes statistically significant with Type I interferon signaling, Treg differentiation, and MHC Class I antigen presentation having scores calculated between 4-5. A high score means that many of the genes in a pathway show variations in expression between sets of groups. Static and low shear statistically differed in 81 genes, with the greatest scores between 3.4 and 3.9 in ECM interactions, Type I Interferon, and MAPK. Lastly, the two shear conditions differed in 14 genes associated with Type I and Type II Interferon and Treg differentiation with scores between 1.5 and 2.

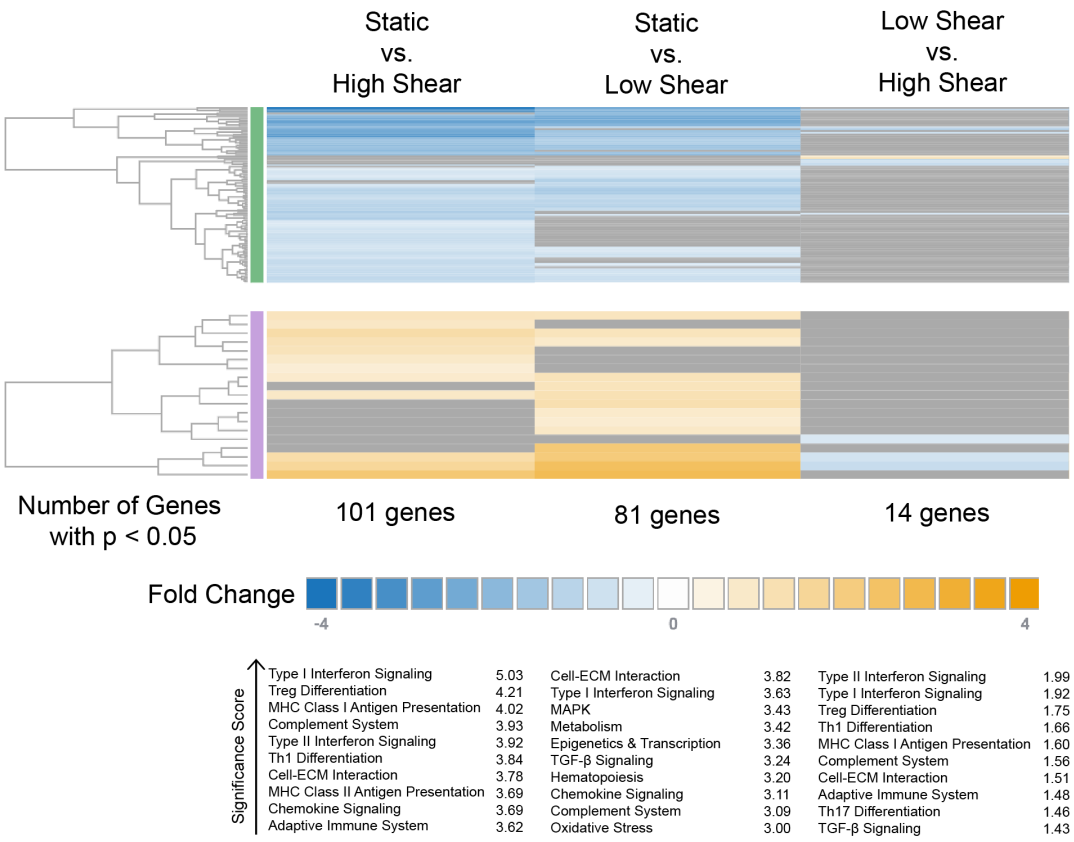


**Figure 3. Meta-Analysis Using ROSALIND Software to Investigate 758 Genes Detected in Nanostring Data Comparing Static, Low Shear, and High Shear Conditions.** Heatmaps display 117 significantly up or down-regulated genes and corresponding cluster significance scores (n=4).

The principal component analysis showed the variance of data with the greatest variance captured between principal components (PC) 1 (26.9%) and 2 (14.8%) (Figure 4A-B). The low and high groups between PC1 and PC2 show greater clustering and similar variance to each other compared to static controls. As more PCs were compared, the variance started to level off with PC 2 vs. PC3 (12.7%) (Figure 4C), PC3 vs. PC4 (8.1%) (Figure 4D), and PC4 vs. PC5 (6.6%) (Figure 4E). Zero variance was calculated with PC12 (Figure 4E).

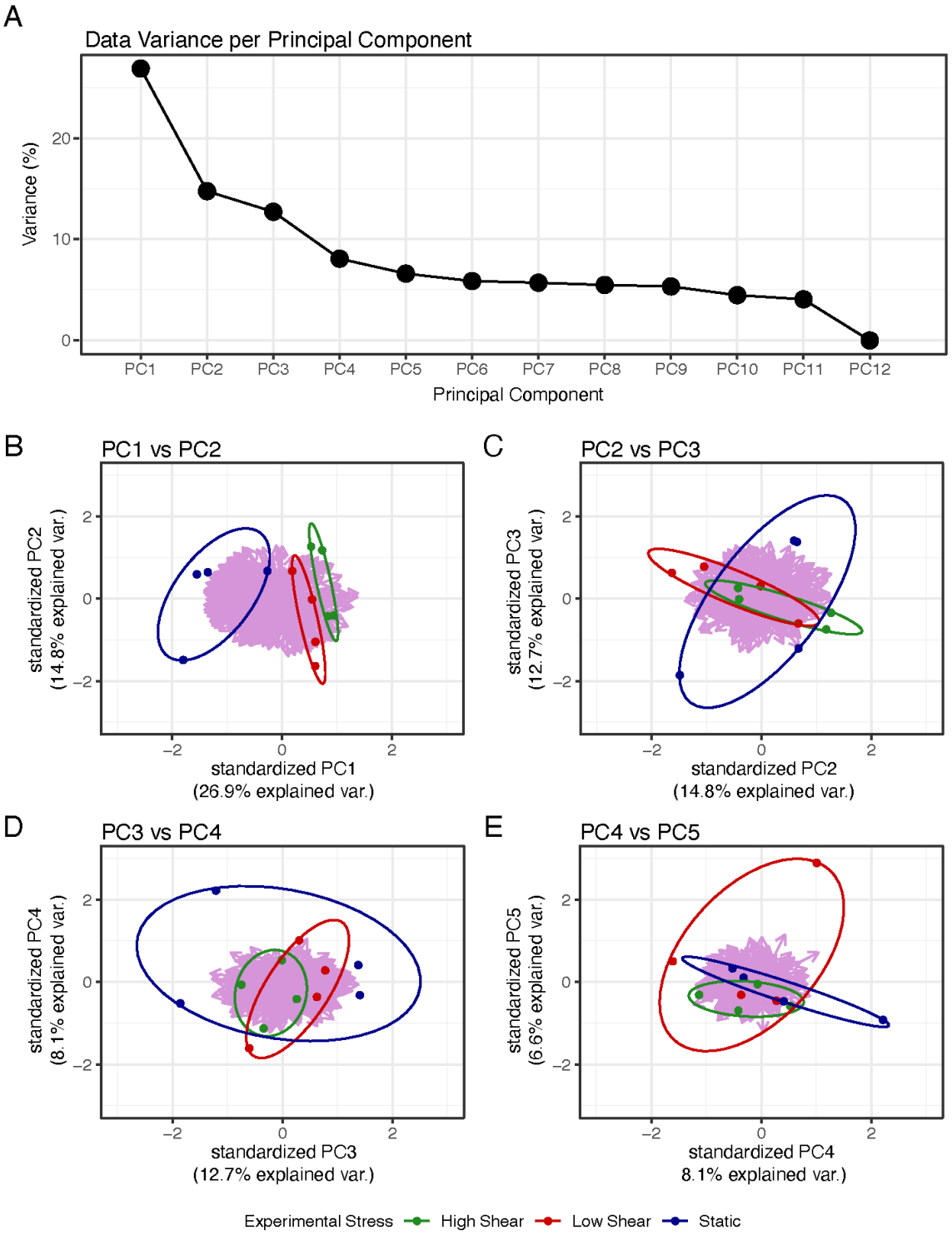


**Figure 4. Principal Component Analysis of Nanostring Gene Expression Comparing Static, Low Shear, and High Shear Conditions.** Calculated principal components (PC)

plotted to show variance until variance is zero (A), and PC variance plotted against the adjacent PC show distinct profiles of static, low shear, and high shear applied to hRPTEC-hTERT1 for 48 hours: (B) PC1 vs. PC2, (C) PC2 vs. PC3, (D) PC4 vs. PC4, (E) PC4 vs. PC5 (n=4).

*3.4 Nephrotoxic and Non-Nephrotoxic Drugs and hRPTEC-hTERT1*

Lactase dehydrogenase (LDH) assay was used to profile a range of drug concentrations to determine appropriate drug concentrations of cisplatin, probenecid, dexamethasone, and gentamicin for in vitro studies using hRPTEC-hTERT1 (Figure 5A). These results were further confirmed using Transepithelial electrical resistance (TEER) using both nephrotoxic (cisplatin) and non-nephrotoxic (dexamethasone and probenecid) drug effects on hRPTEC-hTERT1 over the course of 7 days with two concentrations and compared to vehicle controls (Figure 5B). Both probenecid and dexamethasone maintained similar TEER to vehicle controls at 50 and 100 μM drug concentrations. Meanwhile, cisplatin at 39 μM and 100 μM by 7 d resulted in a TEER to zero, indicating cell death. However, days 1 and 2 showed varying results in the applied concentration with no distinguishable difference at 39 μM cisplatin and vehicle controls until the third day.

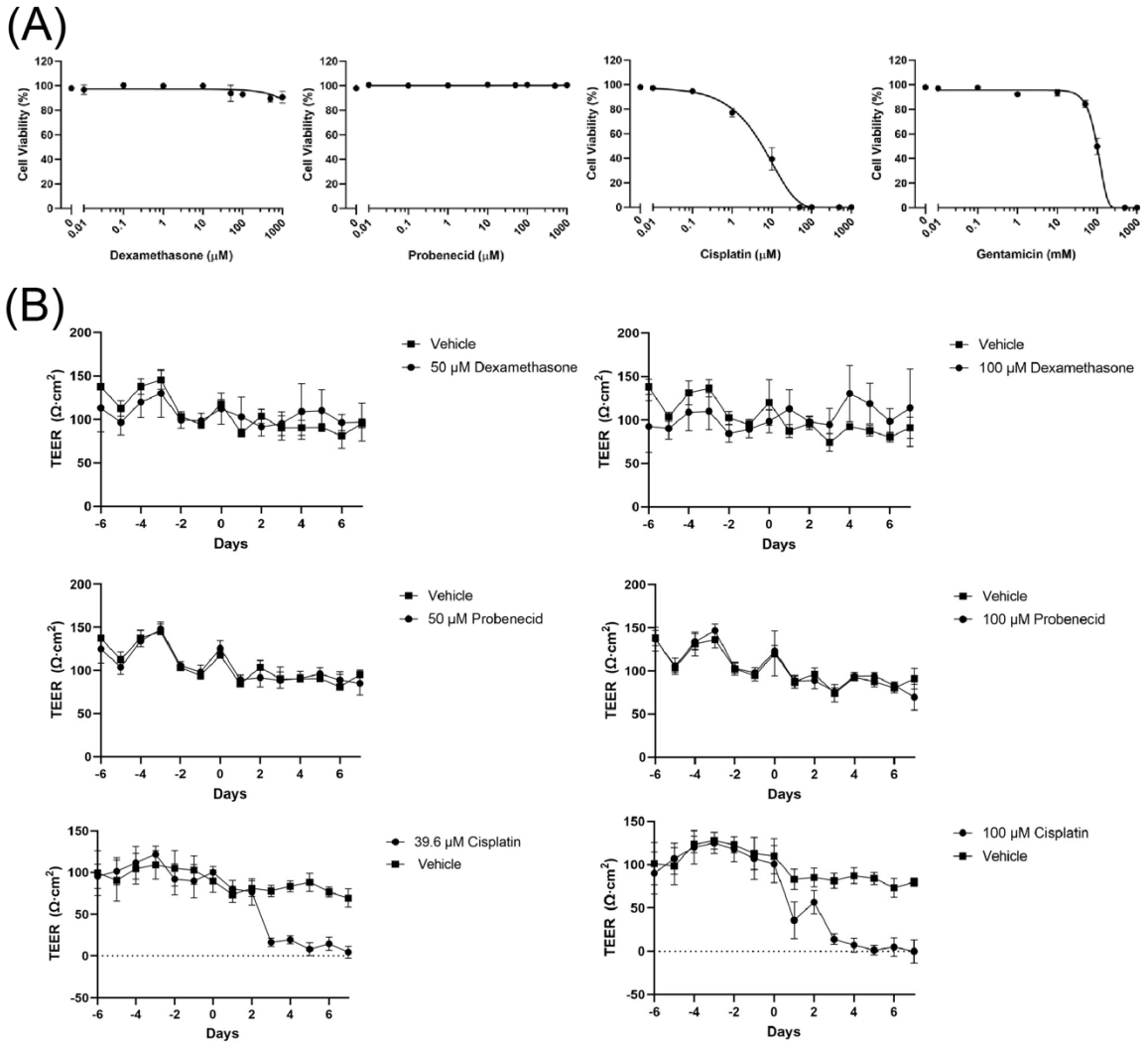


**Figure 5. In Vitro Culture of hRPTEC-hTERT1 with Nephrotoxic Drug Cisplatin Non-Nephrotoxic Drugs Probenecid Using Static LDH Assay at Varying Drug Concentrations, TEER Using Transwell Plates, and LDH Following 48 Hours of Perfusion.** (A) Increasing concentrations of cisplatin and gentamicin, but not probenecid and dexamethasone, correlated with decreased viability. (B) TEER was evaluated for drug effect on barrier function after adding drugs and monitored for 7 days.

LDH assays after the conclusion of the perfusion experiments showed statistically significant results in static vs. low shear and vs. high shear and all conditions tested (Figure 5C).

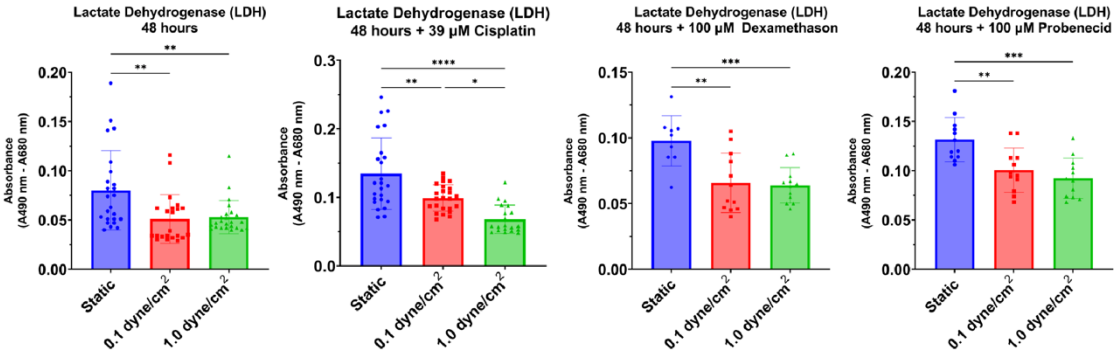


**Figure 6. LDH Relative Absorbance was Measured After Perfusion Without Drugs and With Probenecid, Dexamethasone, or Probenecid.** Imposition of shear resulted in relatively lower cell death levels in drug-free and drug-perfusion conditions.

*3.5 Soluble Factor Analysis*

A non-invasive method to examine cell viability and molecular signaling responses within tissue chip models is through a periodic sampling of the cell culture media. Cell culture samples from the 24-hour timepoint (of flow acclimation) and 48-hour timepoint were utilized to investigate changes in the levels of various soluble factors secreted into the cell culture media. Based on our preliminary studies, three drugs at specific drug concentrations were considered for this study: 39 µM cisplatin, 100 µM dexamethasone, and 100 µM probenecid (Figure 5). Of the 48 cytokines profiled, they were divided into one of the following cytokine families: chemokines CCL, CXCL, and CX3CL; colony-stimulating factors (CSFs), growth factors (GFs), tumor necrosis factors (TNFs), interleukins (ILs), interferons (IFNs), and others. Chemokines are low molecular weight proinflammatory cytokines that were first identified to induce the migration of leukocytes

[27]. Several chemokines, CCL4, CXCL10, and CX3CR1 (not shown), were not identified under our experimental conditions (Figure 7-8). However, eight others (CCL2, CCL3, CCL5, CCL11, CXCL2, CXCL8, CXCL9) were detectable with generally stable concentrations across static, low, and high shear stress conditions and nephrotoxin cisplatin and non-nephrotoxins, dexamethasone, and probenecid. Of exception is RANTES (CCL5), which was upregulated in all static conditions with or without drugs. When cross-referenced with Nanostring gene expression data (only investigating fluidic shear conditions and not nephrotoxicity), cytokine MCP-1 (CCL2) was the only chemokine of statistical significance to be upregulated in the static condition (Figure 7).

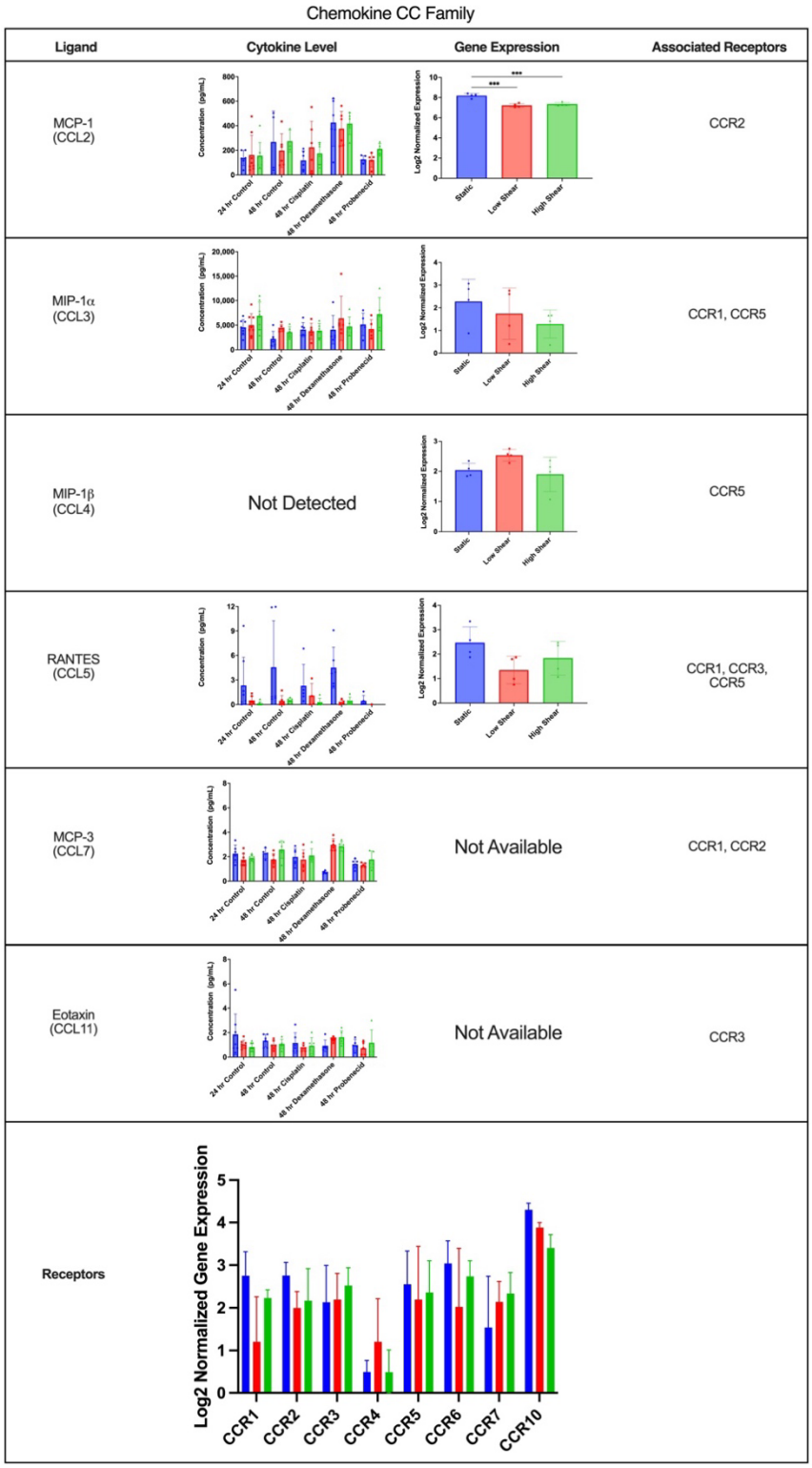


**Figure 7. Chemokine CC Family Cytokine Production and Gene Expression.** 24-hour and 48-hour time points with control, 39 µM cisplatin, 100 µM dexamethasone, or 100 µM

probenecid, and gene expression under static, 0.1 dyne/cm$^2$, or 1.0 dyne/cm$^2$ shear, and associated receptors and receptor expression**.** Of the chemokine-CC family tested (CCL2-7,11), MCP1 and RANTES were upregulated in static conditions indicating an acute inflammatory response in static conditions but no significant alterations in drug responses compared to 24-hour and 48-hour controls.

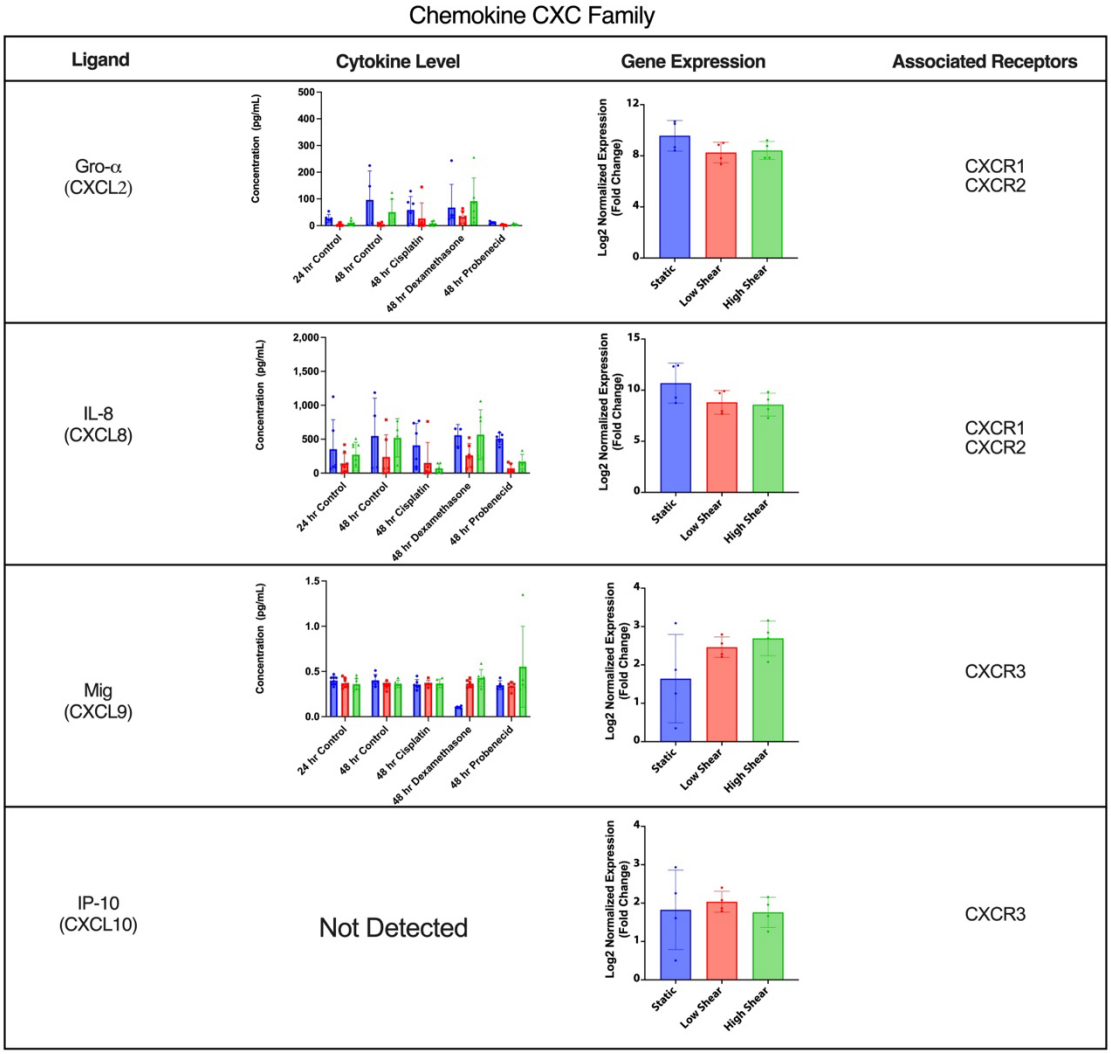


**Figure 8. Chemokine CXC Family Cytokine Production and Gene Expression.** 24-hour and 48-hour time points with control, 39 µM cisplatin, 100 µM dexamethasone, or 100 µM probenecid, and gene expression under static, 0.1 dyne/cm$^2$, or 1.0 dyne/cm$^2$ shear.

The cytokine family of colony-stimulating factors (CSF) consists of macrophages CSF (CSF-1, M-CSF), granulocyte-macrophage CSF (CSF-2, GM-CSF), and granulocyte CSF (CSF-3, G-CSF). In the kidney and specifically the proximal tubule, CSF-1 I is produced in response to acute kidney injury as a mediator of macrophage and dendritic cell polarization and recovery from acute kidney injury [28]. However, gene expression and CSF cytokine production were largely insignificant in the different flow conditions and drug compounds used in this study (Figure 8).

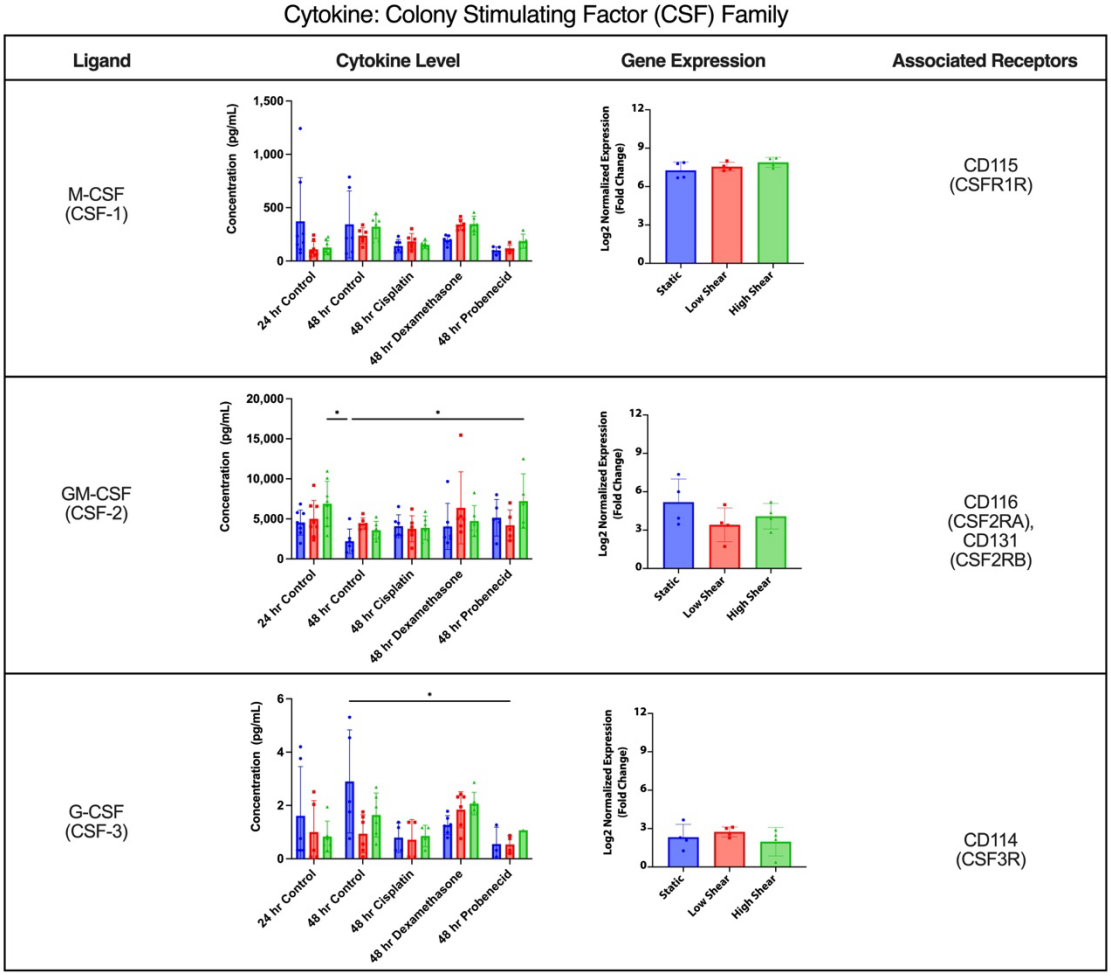


**Figure 9. Colony Stimulating Factor (CSF) Family Cytokine Production and Gene Expression.** During 24-hour and 48-hour time points with control, 39 µM cisplatin, 100

μM dexamethasone, or 100 μM probenecid, and gene expression under static, 0.1 dyne/cm$^2$, or 1.0 dyne/cm$^2$ shear and associated receptors.

In contrast, the proinflammatory tumor necrosis factor family (TNF) of TNF (TNF-α) and TNF-β (LTA) exhibited increased TNF- α cytokine production in static conditions for both time controls and drugs (Figure 10). However, gene expression did not result in an increase. Previous in vitro studies have shown that TNF- α (in addition to IL-1β, IFN-γ, and LPS) rapidly induces MCP-1, IL-8, and IP-10 within a few hours. Whereas RANTES was included between 12 to 48 hours [29, 30]. This correlation between TNF- α and listed cytokines is consistent with our general findings, indicating that chemokines mediate each other during renal inflammation during the initiation and amplification phases of injury.

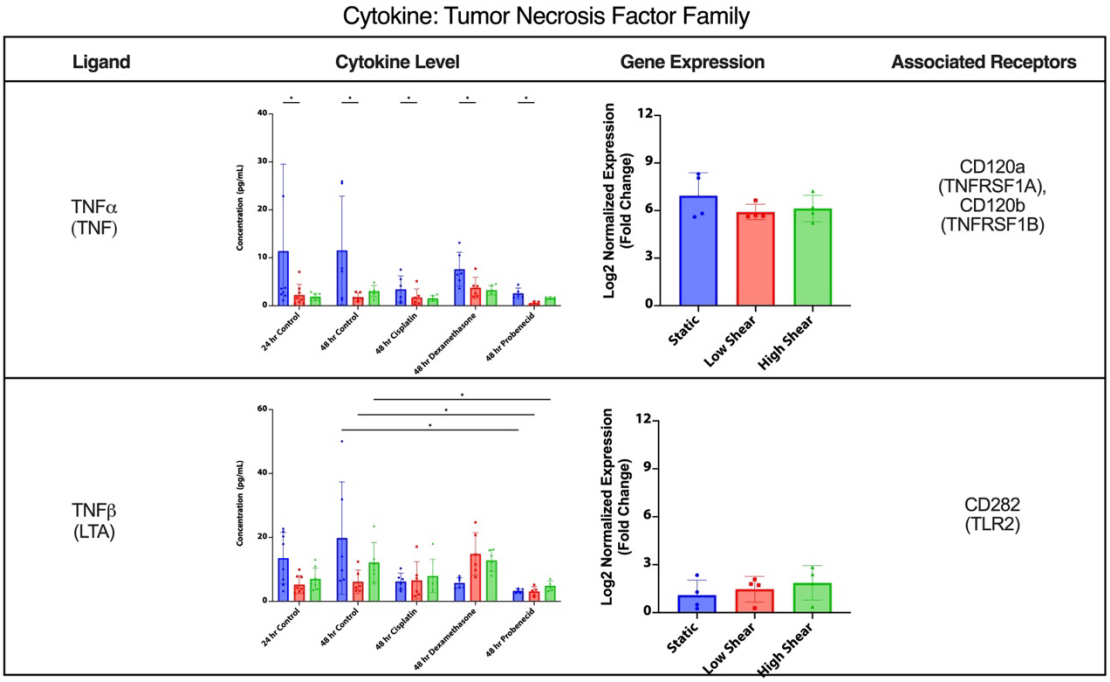


**Figure 10. Tumor Necrosis Factor (TNF) Family Cytokine Production and Gene Expression.** During 24-hour and 48-hour time points with control, 39 μM cisplatin, 100

μM dexamethasone, or 100 μM probenecid, and gene expression under static, 0.1 dyne/cm$^2$, or 1.0 dyne/cm$^2$ shear and associated receptors.

The interferon family of cytokines investigated in this study include Type I Interferons IFN-α1 (IFNA1) and IFN-α2 (IFNA2), and Type II Interferons IFN-γ1. Type I interferons are typically induced when present with a virus and are not known to be produced by renal epithelial cells but by fibroblasts and monocytes. Type II interferons are known to be proinflammatory and released by cytotoxic T cells and type-1 T helper cells. Interestingly, the Nanostring expression with some of the greatest significant scores between static and shear groups was for interferon type I and II (Figure 3). The expression of these cytokines by themselves was insignificant, but the receptors chains for IFNAR2 and INFGR2 were significant (Figure 11). Additionally, cytokine production was generally inconclusive but with some upregulation in IFN-γ in static controls.

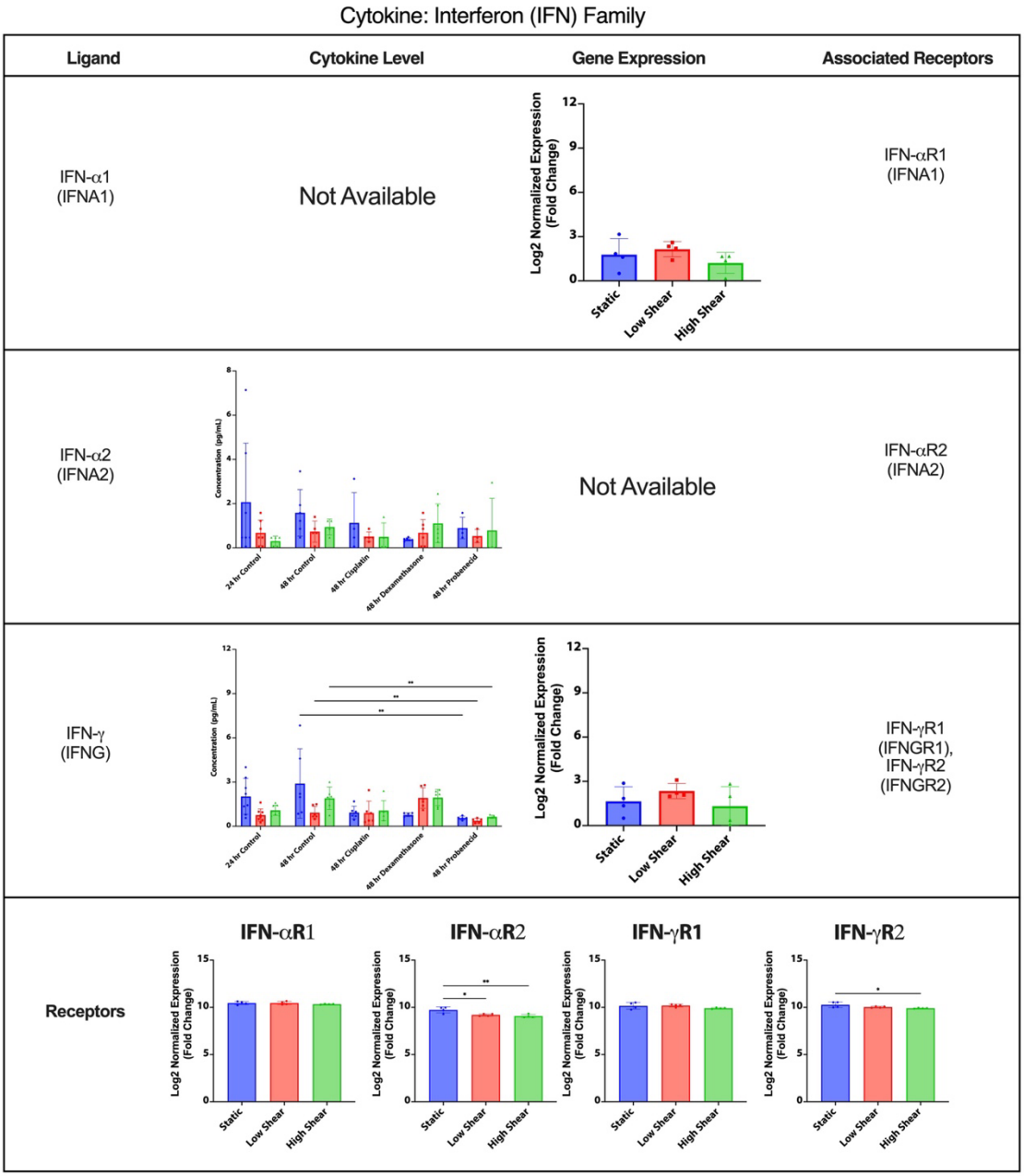


**Figure 11. Interferon Family Cytokine Production and Gene Expression.** During 24-hour and 48-hour time points with control, 39 µM cisplatin, 100 µM dexamethasone, and 100 µM probenecid, and gene expression under static, 0.1 dyne/cm$^2$, or 1.0 dyne/cm$^2$ shear and associated receptors.

Chemokine Interleukin (IL) Family (1/2)

| Ligand | Cytokine Level | Gene Expression |
|---|---|---|
| IL-1β | 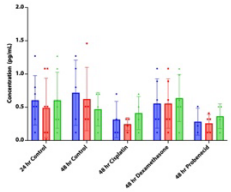 | 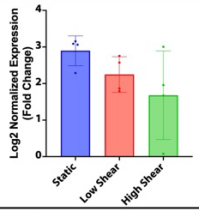 |
| IL-4 | 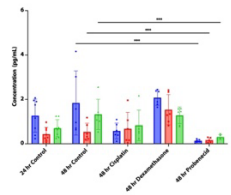 | 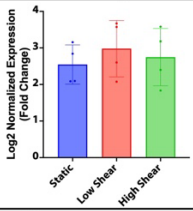 |
| IL-6 | 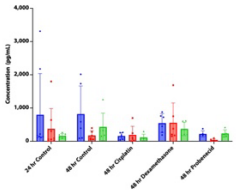 | 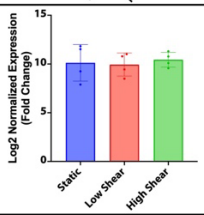 |
| IL-9 | 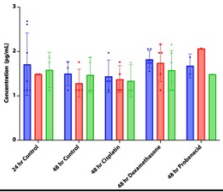 | Not Available |
| IL-13 | 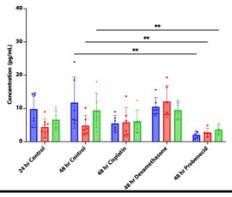 | 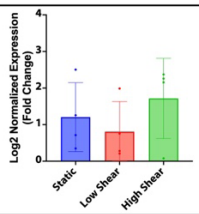 |
| IL-15 | 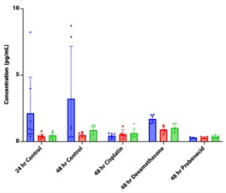 | 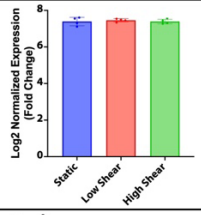 |
| IL-17A | 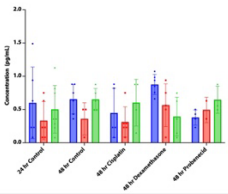 | 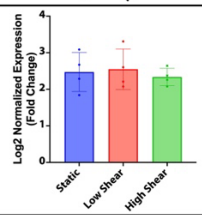 |

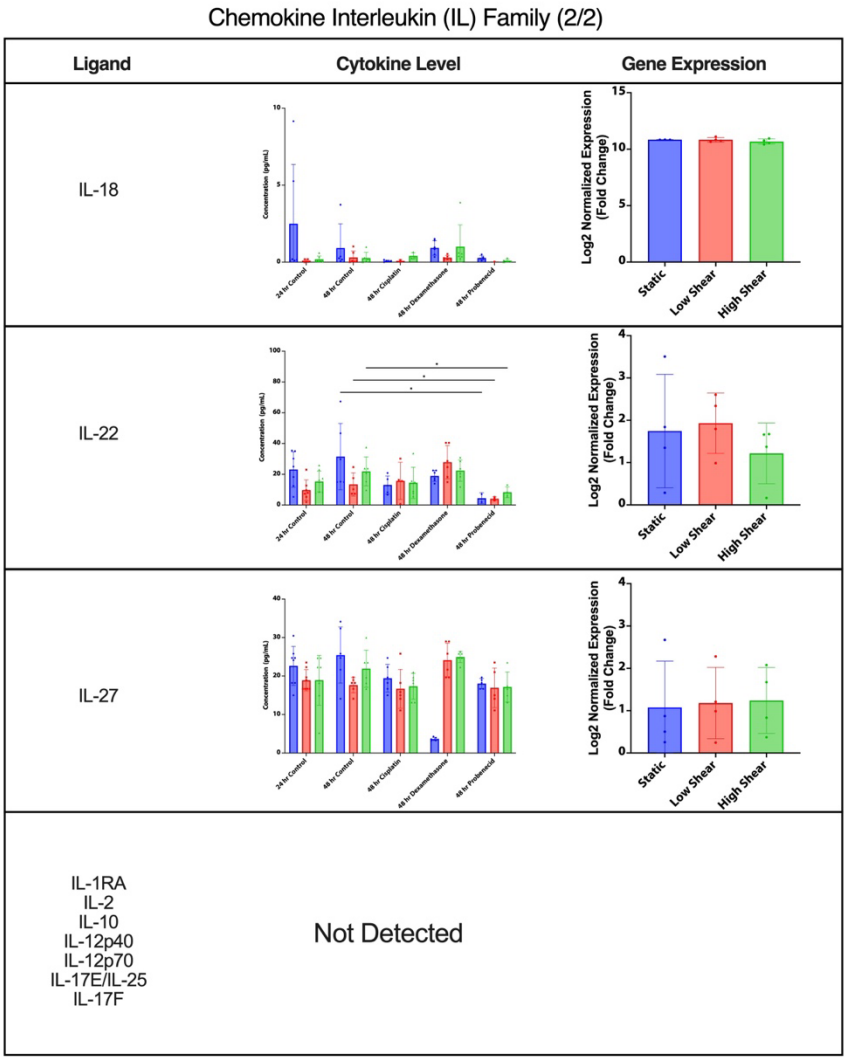


**Figure 12. Interleukin Family Cytokine Production and Gene Expression.** During 24-hour and 48-hour time points with control, 39 µM cisplatin, 100 µM dexamethasone, and 100 µM probenecid, and gene expression under static, 0.1 dyne/cm$^2$, or 1.0 dyne/cm$^2$ shear.

Notably, the broad Interleukin family cytokine production and gene expression were largely insignificant in this study's different flow conditions and drug compounds (Figure 12). Very low concentration values (< 10 pg/mL) were common for this family subtype and did not appear as shear-sensitive as the other cytokines discussed. In

contrast, the growth factor family including epidermal growth factor (EGF), fibroblast growth factor 2 (FGF2), platelet-derived growth factors AA and AB/BB (PDGF-AA, PDGF-AB/BB), transforming factor α and β (TGF-α, TGF-β), and vascular endothelial growth factor (VEGFA) were more shear-sensitive (Figure 13). PDGF-AB/BB cytokine production was significantly increased in all static conditions, whereas TGF-α shear conditions were upregulated. Of particular interest is the gene expression of TGF-β1 and 2 which were highly significant in static conditions compared to both shear conditions. The role of TGF-β1 in proximal tubule epithelial-myofibroblast trans-differentiation has been studied widely for their participation in perpetuating renal fibrosis, therefore, associated markers were investigated further in section 3.5.

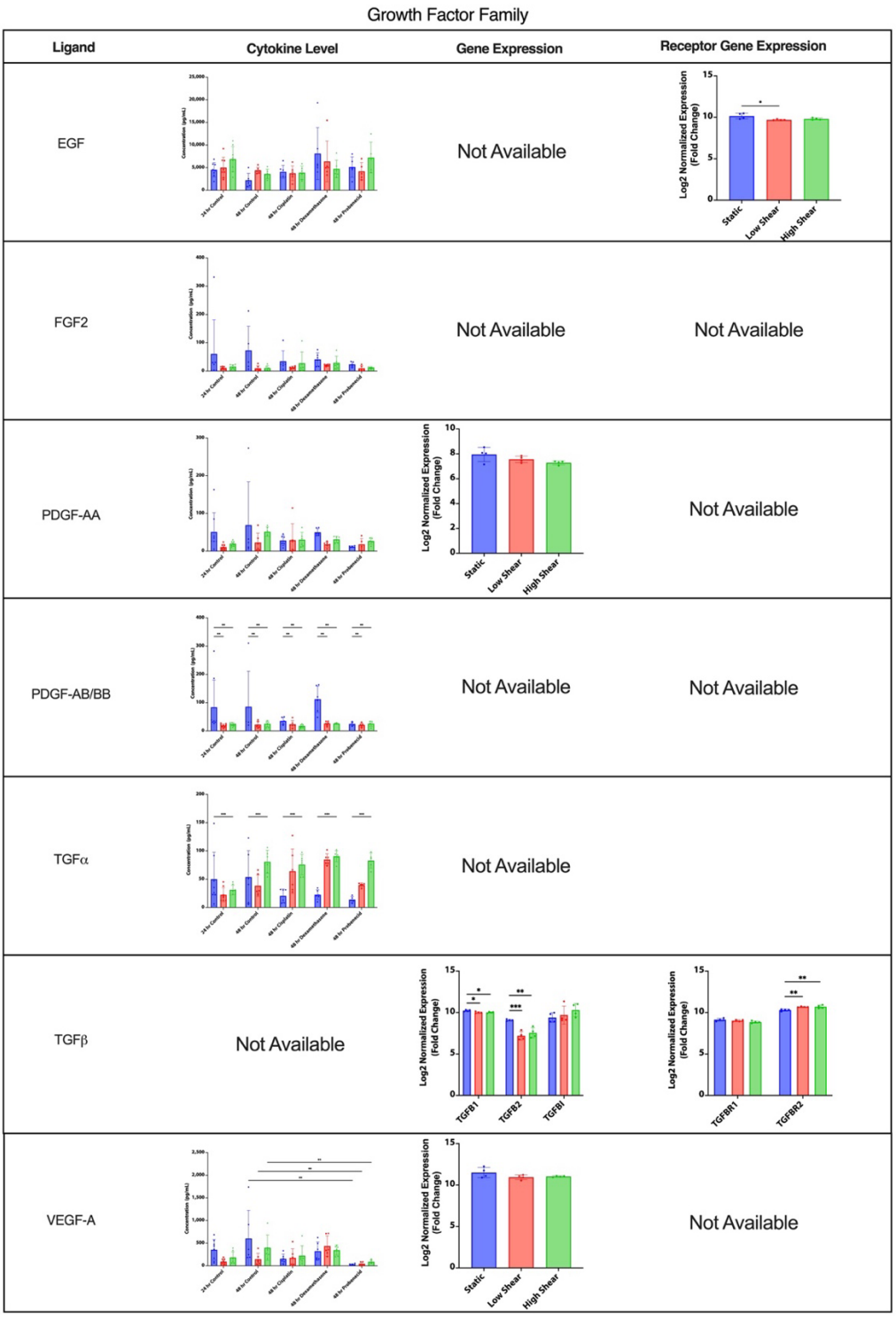


**Figure 13. Growth Factor Family Cytokine Production and Gene Expression.** During 24-hour and 48-hour time points with control, 39 µM cisplatin, 100 µM dexamethasone,

and 100 μM probenecid, and gene expression under static, 0.1 dyne/cm$^2$, or 1.0 dyne/cm$^2$ shear with associated receptor expression.

*3.5 Additional Findings: In vitro Human Proximal Tubule Cells in Static Culture Experience Up-Regulation of Mediators in the Fibrotic Pathway*

Based on the results surrounding potential static epithelial to mesenchymal transition (EMT) in section 3.4, a greater investigation of these mechanisms was conducted. Growth factors, angiogenic factors, fibrogenic cytokines, and proteinases are produced during chronic inflammation that frequently leads to renal fibrosis. A collection of these factors, ECM alternations, and transcription factors detected in Nanostring gene expression are summarized (Figure 14). Via epithelial to EMT, these variables can promote an excessive buildup of ECM components to further contribute to renal fibrosis. Transforming growth factor-beta (TGF-β) is thought to have a key role in triggering EMT and is implicated in renal cell proliferation, apoptosis, hypertrophy, and ECM protein production (Figure 13).

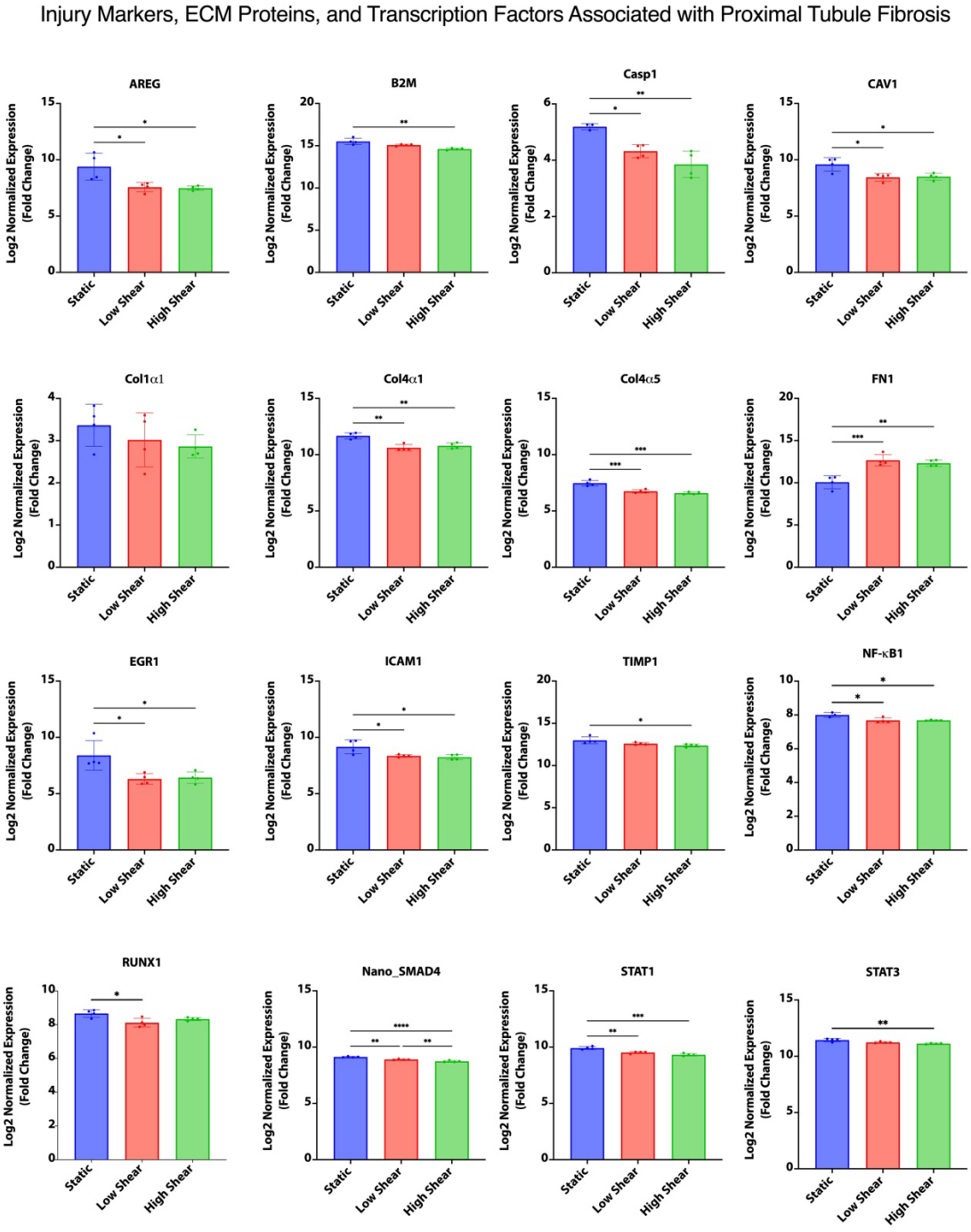


**Figure 14. Epithelial-to-Mesenchymal Transition and Proximal Tubule Fibrosis Related Transcription Factors Upregulated in Static Conditions.**

Injury markers B2M and ICAM1 were elevated in static conditions. Signal transduction and endocytosis protein, caveolin-1 (encoded by CAV1), a known caveolae component,

was shown to be expressed in PT cells in culture but absent from PT in vivo [31]. Under static conditions in our system, CAV1 expression was upregulated compared to both low and high shear conditions. ECM deposition is a critical alteration seen in renal fibrosis. Our study detected increases in Collagen IV α1 and α5 under static conditions, with no significant changes in Collagen 1α1. Interestingly, fibronectin, another mediator of tubular fibrosis, was higher in shear conditions compared to controls. Lastly, proinflammatory and profibrotic transcription factors EGR, NF-κB, and RUNX1 were all elevated in static conditions. In summary, in addition to investigating the role in which nephrotoxic drugs alter cytokine production under shear conditions compared to static markers of proximal tubular injury, EMT and renal fibrosis were determined to be highly influenced by fluidic shear stress.

## 4. Discussion and Conclusions

The innovation in this chapter is the design and fabrication of a microfluidic model of a specific renal niche (i.e.) the PT, the variety of assays to investigate alterations due to shear stress, and the use of multiple nephrotoxic drugs and noninvasive assessments to profile drug-induced nephrotoxicity. As discussed in chapter one, several research groups have developed proximal tubule tissue chips in the last few years [7, 21, 32-36]. However, many do not include multiple drugs or include appropriate non-nephrotoxic controls. Furthermore, such models oftentimes use non-human or non-proximal tubule-specific epithelial cells (ex., HK-2 cells) or accomplish an evaluation of cells under a single-shear stress setpoint [37]. Finally, in vivo, alternations in flow rate occur in concert with changes in glomerular filtration rate (GFR), tubuloglomerular feedback (TGF) via the macula densa, pelvic wall contraction, and reabsorption rates [38-45]. Therefore, the proximal

tubule model utilized and studied in this chapter strives to explore the effects of shear stress to a greater extent to build upon prior published work.

In this study, accurate replication of in-vivo fluidic shear stress was highly important; therefore, we modeled the proximal tubule device using computer-aided design (CAD) software and simulated flow profiles using computational fluid dynamics (CFD) (Figure 1). These assessments (in combination with real-life flow loops with flow and pressure sensors) validated that the biomechanical forces applied on hRPTECs-hTERT cells cultured within our systems were appropriate. The range of shear stresses found in the literature for the proximal tubule is predominately between 0.1 to 1.0 dyne/cm$^2$ [37, 45-49]. Therefore, we moved forward with these lower and upper range values as our two shear conditions. Based on the findings presented in this chapter confirming that the selected shear stresses are within physiological levels, future studies of super-physiological shear stress (i.e.,> 1.0 dyne/cm$^2$) could potentially evaluate the effects of pathological shear stress.

We utilized hRPTEC-TERT1 cells as they are immortalized through the stable expression of the catalytic subunit of human telomerase reverse transcriptase (hTERT) and readily prevent mesenchymal-epithelial transition [6]. These cells have been well characterized to retain the functional properties of primary cells while maintaining consistent expression levels of functional markers over several passages [7]. Due to the limitations of immortalized cell lines, our in vitro study provides a thorough overview of how fluid shear stress alters gene expression and cytokine production in human renal epithelial cells, but it is not entirely representative of the in vivo condition. Therefore, some

drug responses of this cell line should be further evaluated on whether hTERT alters its nephrotoxicity response.

This study categorized drugs based on the nephrotoxic effects and relative PT damage to “Low”: drugs that are not harmful to the kidney; “Intermediate”: drugs that are considered damaging to other parts of the kidney (glomerulus, distal tubule); “High”; direct PT toxicity or via a secondary mechanism such as crystal formation. However, due to the timing of this thesis, we only comprehensively investigated low dexamethasone and probenecid, and the high nephrotoxin, cisplatin. These drugs exert widely different mechanisms on the proximal tubule epithelium. Cisplatin is transported basolaterally through the organic cation 2 (OCT2) [50]. Whereas Probenecid is a uricosuric agent that inhibits the organic anion transporters in the PT and is used in the treatment of gout [51]. Lastly, Dexamethasone is a glucocorticoid available in various administration modes to treat various inflammatory conditions.

Secker et al. demonstrated similar drug cytotoxicity assessments and static transepithelial electrical resistance to our study [52]. A dynamic TEER instrument called PREDICT96 from Draper Laboratories utilized primary human renal proximal tubule cells at either 0.1 or 0.7 dyne/cm$^2$ [53]. The addition of their highest concentration of cisplatin (25 μM) showed the greatest reduction in TEER, 25 W·cm$^2$, after 72 hours and in the low shear condition. Compared to our static TEER experiments using 39 and 100 μM cisplatin in the same timeframe, we observed greater than a 50 W·cm$^2$ reduction in TEER. Furthermore, media perfusate analysis allowed for time-dependent monitoring of hRPTEC cytokine markers in vitro and provided insights into the dynamics involved in drug-induced toxicity.

A difficulty in microfluidic models is designing well-balanced models—meaning they are small enough to conserve the use of tissue engineering reagents, hydrogels, cells, etc. but also large enough to elicit observable cell responses. For example, the quantity of RNA harvested from a microfluidic device like the one used in this chapter would not be sufficient to run more than a couple of RT-qPCRs targets with replicates. Compared to 500 ng RNA required for >700 targets analyzed via Nanostring and RNA sequencing, this makes RT-qPCR an unfavorable and more biased option for studying gene expression.

Few research groups have utilized Nanostring analysis of kidney samples, despite its ease of use, higher throughput and accuracy compared to RT-qPCR, and reduced costs compared to RNA-seq [54-56]. Previous transcriptional profiling studies of hRPTECs-hTERT under shear stress (between 0-0.5 dyne/cm$^2$) for 24 hours found enhanced polarization, presence of cilia, and transport functions using albumin reabsorption via endocytosis and efflux transport [57], but did not discuss markers and transcripts associated with EMT in detail. One transcriptomic study using murine proximal tubule cells observed TGF-β, MAPK, and Wnt signaling as core signaling pathways up-regulated by shear (0.25–2.0 dyne/cm$^2$) and up-regulated cytokine pathways included FGF, HB-EGF, PDGF, and CXC after 24 hours [37]. Therefore, this is the first study to identify EMT profiles using human cells across a larger spectrum of shear stress. The importance is notable because epithelial-mesenchymal transitions are considered the key basis by which resident epithelial cells dedifferentiate, leading to renal fibrosis.

In summary, this model was validated using drugs known to cause toxicity to tubular cells. Ensuring physiological pressure and shear associated with the tubular flow are critical components of bioengineering a faithful tissue chip model of the proximal

tubule. This innovative in vitro model offers a practical method to study renal pharmacology, renal drug transport, and toxicities pertinent to the physiology of the human kidney.

Reference:


1. Kim, S.-Y. and A.R. Moon, *Drug-Induced Nephrotoxicity and Its Biomarkers.* Biomolecules & therapeutics, 2012. **20**(3): p. 268-272.
2. Madariaga, M.L. and H.C. Ott, *Bioengineering kidneys for transplantation.* Semin Nephrol, 2014. **34**(4): p. 384-93.
3. Craveiro, N.S., et al., *Drug Withdrawal Due to Safety: A Review of the Data Supporting Withdrawal Decision.* Current Drug Safety, 2020. **15**(1): p. 4-12.
4. Guo, X. and C. Nzerue, *How to prevent, recognize, and treat drug-induced nephrotoxicity.* Cleve Clin J Med, 2002. **69**(4): p. 289-90, 293-4, 296-7 passim.
5. Bhargava, P. and R.G. Schnellmann, *Mitochondrial energetics in the kidney.* Nature Reviews Nephrology, 2017. **13**(10): p. 629-646.
6. Wieser, M., et al., *hTERT alone immortalizes epithelial cells of renal proximal tubules without changing their functional characteristics.* American journal of physiology., 2008. **295**(5): p. F1365-F1375.
7. Homan, K.A., et al., *Bioprinting of 3D Convoluted Renal Proximal Tubules on Perfusable Chips.* Sci Rep, 2016. **6**: p. 34845.
8. Donoghue, L., et al., *Tissue Chips and Microphysiological Systems for Disease Modeling and Drug Testing.* Micromachines, 2021. **12**(2): p. 139.
9. Donoghue, L., C. Graham, and P. Sethu, *Acute Response of Engineered Cardiac Tissue to Pressure and Stretch.* Cells Tissues Organs, 2022.
10. Kim, S.-H., et al., *PDMS double casting method enabled by plasma treatment and alcohol passivation.* Sensors and Actuators B: Chemical, 2019. **293**: p. 115-121.
11. Zhang, H., et al., *The impact of extracellular matrix coatings on the performance of human renal cells applied in bioartificial kidneys.* Biomaterials, 2009. **30**(15): p. 2899-911.
12. Geuzaine, C. and J.-F. Remacle, *Gmsh: A 3-D finite element mesh generator with built-in pre- and post-processing facilities.* International Journal for Numerical Methods in Engineering, 2009. **79**(11): p. 1309-1331.
13. Maas, S.A., et al., *FEBio: Finite Elements for Biomechanics.* Journal of Biomechanical Engineering, 2012. **134**(1).
14. Perkins, J.R., et al., *ReadqPCR and NormqPCR: R packages for the reading, quality checking and normalisation of RT-qPCR quantification cycle (Cq) data.* BMC Genomics, 2012. **13**(1): p. 1-8.
15. Hennig, C., *Cran-package fpc.*
16. Alexa A, R.J., *topGO: Enrichment Analysis for Gene Ontology*. 2019.
17. Slenter, D.N., et al., *WikiPathways: a multifaceted pathway database bridging metabolomics to other omics research.* Nucleic Acids Res, 2018. **46**(D1): p. D661-d667.
18. Mitchell, A.L., et al., *InterPro in 2019: improving coverage, classification and access to protein sequence annotations.* Nucleic Acids Research, 2018. **47**(D1): p. D351-D360.
19. Geer, L.Y., et al., *The NCBI BioSystems database.* Nucleic Acids Research, 2009. **38**(suppl_1): p. D492-D496.
20. Liberzon, A., et al., *The Molecular Signatures Database (MSigDB) hallmark gene set collection.* Cell Syst, 2015. **1**(6): p. 417-425.

21. Subramanian, A., et al., *Gene Set Enrichment Analysis: A Knowledge-Based Approach for Interpreting Genome-Wide Expression Profiles.* Proceedings of the National Academy of Sciences of the United States of America, 2005. **102**(43): p. 15545-15550.
22. Fabregat, A., et al., *The Reactome Pathway Knowledgebase.* Nucleic Acids Research, 2017. **46**(D1): p. D649-D655.
23. Abdi, H. and L.J. Williams, *Principal component analysis.* WIREs Computational Statistics, 2010. **2**(4): p. 433-459.
24. Bro, R. and A.K. Smilde, *Principal component analysis.* Analytical methods, 2014. **6**(9): p. 2812-2831.
25. Molania, R., et al., *A new normalization for Nanostring nCounter gene expression data.* Nucleic Acids Research, 2019. **47**(12): p. 6073-6083.
26. Bhattacharya, A., et al., *An approach for normalization and quality control for NanoString RNA expression data.* Briefings in Bioinformatics, 2020. **22**(3).
27. Zlotnik, A. and O. Yoshie, *Chemokines: a new classification system and their role in immunity.* Immunity, 2000. **12**(2): p. 121-7.
28. Wang, Y., et al., *Proximal tubule-derived colony stimulating factor-1 mediates polarization of renal macrophages and dendritic cells, and recovery in acute kidney injury.* Kidney Int, 2015. **88**(6): p. 1274-1282.
29. Chiu, J.J., et al., *Effects of disturbed flow on endothelial cells.* J Biomech Eng, 1998. **120**(1): p. 2-8.
30. Anders, H.-J., V. Vielhauer, and D. Schlöndorff, *Chemokines and chemokine receptors are involved in the resolution or progression of renal disease.* Kidney international, 2003. **63**(2): p. 401-15.
31. Zhuang, Z., et al., *Is caveolin involved in normal proximal tubule function? Presence in model PT systems but absence in situ.* American Journal of Physiology-Renal Physiology, 2011. **300**(1): p. F199-F206.
32. Jang, K.J., et al., *Human kidney proximal tubule-on-a-chip for drug transport and nephrotoxicity assessment.* Integr Biol (Camb), 2013. **5**(9): p. 1119-29.
33. Astashkina, A.I., et al., *A 3-D organoid kidney culture model engineered for high-throughput nephrotoxicity assays.* Biomaterials, 2012. **33**(18): p. 4700-11.
34. Weber, E.J., et al., *Development of a microphysiological model of human kidney proximal tubule function.* Kidney Int, 2016. **90**(3): p. 627-37.
35. Homan, K.A., et al., *Flow-enhanced vascularization and maturation of kidney organoids in vitro.* Nature Methods, 2019. **16**(3): p. 255-262.
36. Lin, N.Y.C., et al., *Renal reabsorption in 3D vascularized proximal tubule models.* Proc Natl Acad Sci U S A, 2019. **116**(12): p. 5399-5404.
37. Kunnen, S.J., et al., *Comprehensive transcriptome analysis of fluid shear stress altered gene expression in renal epithelial cells.* Journal of Cellular Physiology, 2018. **233**(4): p. 3615-3628.
38. Gilmer, G.G., et al., *Flow resistance along the rat renal tubule.* Am J Physiol Renal Physiol, 2018. **315**(5): p. F1398-f1405.
39. Holstein-Rathlou, N.H. and D.J. Marsh, *Oscillations of tubular pressure, flow, and distal chloride concentration in rats.* Am J Physiol, 1989. **256**(6 Pt 2): p. F1007-14.

40. Reinking, L.N. and B. Schmidt-Nielsen, *Peristaltic flow of urine in the renal capillary collecting ducts of hamsters.* Kidney Int, 1981. **20**(1): p. 55-60.
41. Sakai, T., et al., *Fluid waves in renal tubules.* Biophys J, 1986. **50**(5): p. 805-13.
42. Ulfendahl, H.R., et al., *The tubulo-glomerular feedback mechanism-a determinant for the autoregulation of the glomerular filtration rate in superficial and juxtamedullary nephrons.* Klin Wochenschr, 1982. **60**(18): p. 1071-6.
43. Schnermann, J., et al., *Regulation of superficial nephron filtration rate by tubulo-glomerular feedback.* Pflügers Archiv, 1970. **318**(2): p. 147-175.
44. Vallon, V., *Tubuloglomerular feedback and the control of glomerular filtration rate.* News Physiol Sci, 2003. **18**: p. 169-74.
45. Verschuren, E.H.J., et al., *Sensing of tubular flow and renal electrolyte transport.* Nature Reviews Nephrology, 2020. **16**(6): p. 337-351.
46. Grabias, B.M. and K. Konstantopoulos, *Epithelial-mesenchymal transition and fibrosis are mutually exclusive reponses in shear-activated proximal tubular epithelial cells.* The FASEB Journal, 2012. **26**(10): p. 4131-4141.
47. Weinbaum, S., et al., *Mechanotransduction in the renal tubule*. 2010, American Physiological Society.
48. Park, H.J., et al., *Transcriptional Programs Driving Shear Stress-Induced Differentiation of Kidney Proximal Tubule Cells in Culture.* Frontiers in physiology, 2020. **11**: p. 587358.
49. Birdsall, H.H. and T.G. Hammond, *Role of Shear Stress on Renal Proximal Tubular Cells for Nephrotoxicity Assays.* J Toxicol, 2021. **2021**: p. 6643324.
50. Miller, R.P., et al., *Mechanisms of Cisplatin nephrotoxicity.* Toxins (Basel), 2010. **2**(11): p. 2490-518.
51. Barone, S., et al., *Probenecid Pre-treatment Downregulates the Kidney Cl(-)/HCO(3)(-) Exchanger (Pendrin) and Potentiates Hydrochlorothiazide-Induced Diuresis.* Front Physiol, 2018. **9**: p. 849.
52. Secker, P.F., et al., *Functional transepithelial transport measurements to detect nephrotoxicity in vitro using the RPTEC/TERT1 cell line.* Arch Toxicol, 2019. **93**(7): p. 1965-1978.
53. Shaughnessey, E.M., et al., *Evaluation of rapid transepithelial electrical resistance (TEER) measurement as a metric of kidney toxicity in a high-throughput microfluidic culture system.* Sci Rep, 2022. **12**(1): p. 13182.
54. Hay, A., et al., *Optimization of RNA extraction from laser captured microdissected glomeruli from formalin-fixed paraffin-embedded mouse kidney samples for Nanostring analysis.* Histology and histopathology, 2020. **35**(1): p. 57-68.
55. Nam, H., et al., *PGC1α suppresses kidney cancer progression by inhibiting collagen-induced SNAIL expression.* Matrix Biology, 2020. **89**: p. 43-58.
56. Aceves, J.O., et al., *3D proximal tubule-on-chip model derived from kidney organoids with improved drug uptake.* Scientific Reports, 2022. **12**(1): p. 14997.
57. Ross, E.J., et al., *Three dimensional modeling of biologically relevant fluid shear stress in human renal tubule cells mimics in vivo transcriptional profiles.* Scientific Reports, 2021. **11**(1).

Supplement:

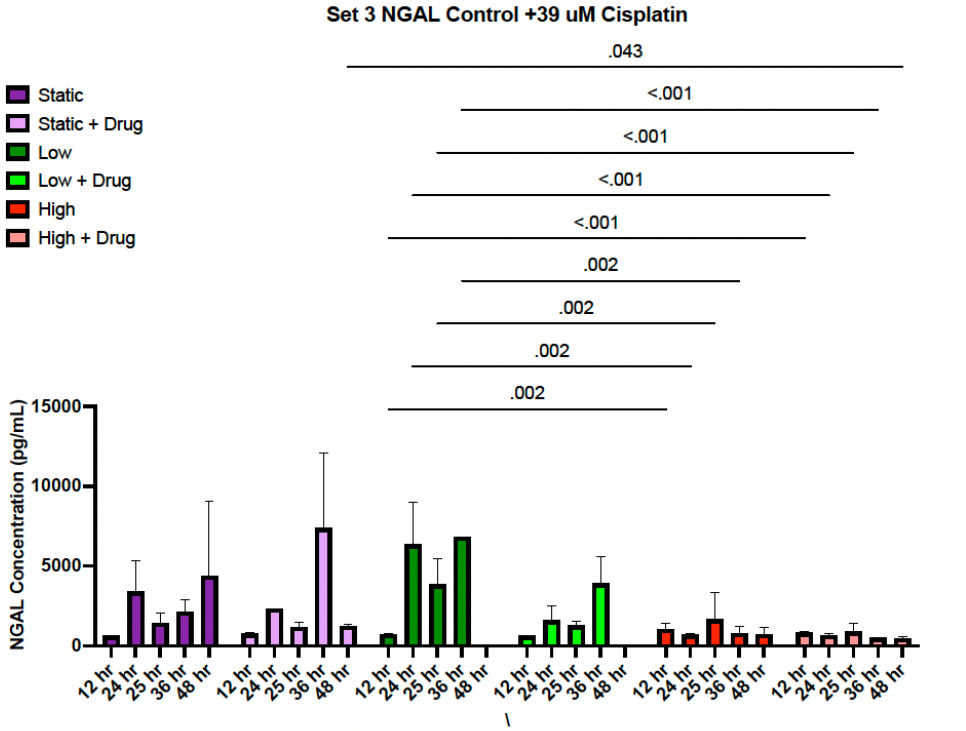
Set 3 NGAL Control +39 uM Cisplatin
.043
<.001
<.001
<.001
<.001
.002
.002
.002
.002
Static
Static + Drug
Low
Low + Drug
High
High + Drug
NGAL Concentration (pg/mL)
15000
10000
5000
0
12 hr
24 hr
25 hr
36 hr
48 hr

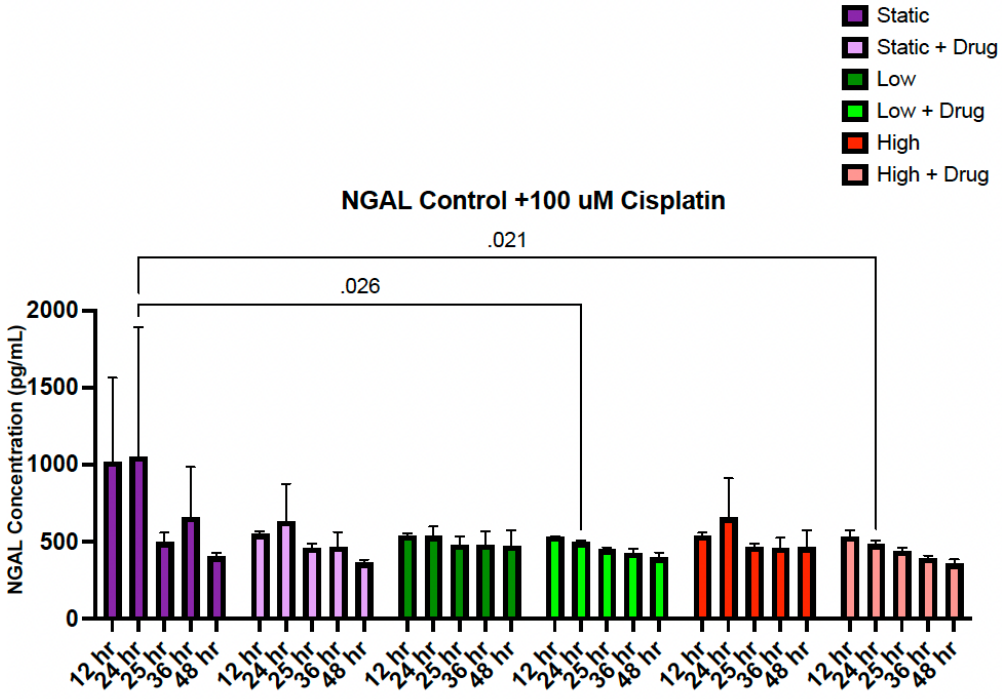
Static
Static + Drug
Low
Low + Drug
High
High + Drug
NGAL Control +100 uM Cisplatin
.021
.026
NGAL Concentration (pg/mL)
2000
1500
1000
500
0
12 hr
24 hr
25 hr
36 hr
48 hr

# CHAPTER 4

# NOVEL HUMAN RENAL PROXIMAL TUBULE TISSUE CHIPS CONTAINING 3D TUBULES WITH SURROUNDING PERITUBULAR MICROVASCULAR NETWORKS

by

LESLIE DONOGHUE, ARUSHI KOTRU, IAN BERG, EMMA STEVENSON, AND PALANIAPPAN SETHU

In preparation for journal submission

Format adapted for dissertation

Specific Aim 2:

To develop a 3D RPTC that combines a 3D proximal tubule and peritubular vascular. To validate the novelty of this model, we will test the hypothesis that the addition of a vascular network enhances physiological relevance and selective transport seen in vivo.

# 1. Introduction

Currently, limited options are available to screen drugs for nephrotoxicity or model diseases associated with the proximal tubule (PT). Existing models often lack 3D structural relevance, inaccurately integrate the vascular network found around the tubules, or have limited throughput capabilities. To become a translatable tool, a proximal tubule chip must replicate tubular architecture, secretion, tubular flow and pressure, reabsorption associated with peritubular capillaries, accurately predict in vivo-like drug responses, and recapitulate tubular disease states.

A major challenge in designing 3D PTs is engineering a supporting biocompatible scaffold to connect the tubular structure with its microvascular network. The scaffold's architecture should allow for the following components: an innermost PT with perfusable lumens. The perfusable channel within the scaffold should support the adhesion of renal proximal tubule epithelial cells and replicate the tubule's natural basement membrane composed of collagen fibers. Surrounding the tubular structure should be a densely packed layer of capillaries, and the density of the scaffold needs to be such that angiogenesis occurs to connect the capillaries to a larger blood vessel structure. Prior efforts to mimic this integration of peritubular capillaries involved electrospinning to generate fiber-based structures using various natural and synthetic biodegradable materials at both nano- and microscale [1]. However, in the recent decade, methods that rely on the self-assembly of microvascular networks have gained popularity in other organ systems and the cancer biology [2-4]. The co-culturing of endothelial cells with a stromal cell line suspended in a hydrogel enables their self-assembly of perfusable capillary networks over a period of five

to seven days. Building complex architectures associated with the renal proximal tubule requires the combination of several cell types (epithelial, endothelial, and fibroblast) to enable epithelium-endothelium crosstalk, but this also create challenges due to limitations associated with the working distances of epifluorescence and confocal microscopes and imaging cells associated with different structures. The limitations associated with short working distances of microscopes was addressed by creating the tubular and microvascular structures in proximity to the microscope coverslip that forms the bottom of the renal proximal tubule chip. To address the issue of distinguishing cells associated with different structures, we created stable microvascular endothelial cell lines fluorescently labeled human microvascular endothelial cells with either tdTomato (maxima 554 nm excitation and 581 nm emission) or enhanced green fluorescent protein (EGFP, maxima 488 nm excitation and 509 nm emission). The two populations distinguish the endothelial cells suspended in a hydrogel that self-assemble into capillaries from the larger endothelial cell channel perfused with cell culture media. Furthermore, the two different fluorophores can show the location of angiogenic sprouting and integration of the microvascular and the larger perfused channel.

The complex architecture of the PT-vascular network enables transport which is approximately 60-80% of the total renal nutrient reabsorption into the surrounding peritubular capillaries [5]. An essential element of these cellular processes is achieving PT epithelial cell polarity containing distinct transporters on the apical and basolateral sides. Functioning and mature PTs exhibit cell polarity, such as basolateral localization of Na+/K+ ATPase, apically expressed sodium-glucose cotransporter-2 (SGLT2), apical primary cilia containing acetylated tubulin, and basal-side deposition of basement

membrane proteins. To validate the reabsorption capability of in vitro proximal tubule and vascular tissue chips, quantifying glucose reabsorption is preferred since healthy PTs in vivo reabsorb essentially one hundred percent of the glucose in the glomerular filtrate. Six different SGLTs have been identified in humans [6, 7]. However, only SGLT1 (in the late PT) and SGLT2 (in the early PT) have been well characterized in the human kidney, with SGLT2 being responsible for the majority (approximately 90%) of glucose reabsorption. Of existing 3D PT models, 3D printing of adjacent PTs and vascular channels in close proximity (within 70 μm) has shown the greatest reabsorption of glucose at about 60 $\mu g/mm^2$ per day [8]. However, when the reabsorption rates are normalized for PT length, diameter, and glucose concentration difference between the two channels, the estimated glucose reabsorption is about twenty percent as efficient as a healthy human kidney. Therefore, the reabsorption properties of in vitro vascularized PT models need to demonstrate greater transport efficiencies than previously demonstrated to mimic in vivo PT function accurately. In this chapter, we discuss methods and advances in our 3D proximal tubule model that aims to incorporate a dense microvascular surrounding a perfused PT to improve upon the architecture and function of these models to better study and model disease or test nephrotoxic compounds.

## 2. Materials and Methods

### *2.1 Cell Culture*

Human renal proximal tubule cells (hPTEC-hTERT1) were purchased from ATCC (ATCC, CRL-4031) and cultured in Dulbecco's Modified Eagle's Medium: F-12 (ATCC, 30-2006) supplemented with hTERT Immortalized RPTEC growth kit (ATCC, ACS-4007) and. 1% geneticin antibiotic (G418) (Thermo Scientific, 10131035) according to the

manufacturer's protocols. The hRPTEC-hTERT1 cells were split at approximately 90% confluence using 0.05% trypsin EDTA (Gibco, 25200-054).

Lenti-X$^{TM}$ HEK-293T (Takara, 632180) cells were kindly gifted from UAB's Dr. Jay Zhang's lab. Cells were revived from frozen aliquots initially seeded on Matrigel® (Corning, CB-40230A) coated 6-well plates to enhance attachment and cultured in Dulbecco's Modified Eagle's Medium with high glucose (Gibco, 11965092) and supplemented with 10% fetal bovine serum (Fisher Scientific, FB12999102).

Human dermal microvascular endothelial cells (hMEC-1s) (ATCC, CRL-3243) were kindly gifted by UAB's Dr. Mary Kathryn Sewell-Loftin's Lab. Primary human dermal fibroblasts (hDFs) were purchased from ATCC (ATCC, PCS-201-010). Both hMEC-1s and hDFs were cultured in EGM-2 (Lonza, CC-3162). The hMECs were split at approximately 85% confluence using 0.25% trypsin EDTA (ATCC, 30-2101), while hDFs were split at approximately 90% confluency with 0.05% trypsin EDTA. All cell types listed were grown in a humidified incubator containing 5% $CO_2$ at 37 °C.

*2.2 Plasmid Construction and Validation*

The plasmid pLJM1-EGFP (Addgene, 19319) was commercially purchased, while the plasmid pLJM1-tdTomato was constructed using the insert from pCSCMV:tdTomato (Addgene, 30530) and the backbone of pLJM1-EGFP. In sterile conditions, the plasmids were plated on 100 mm diameter Petri dishes containing agar (Sigma, L7025) and ampicillin (Sigma, A9518). To prevent excessive bacterial growth, they were plated during the late afternoon and allowed to grow overnight in a 37 °C oven. The next morning, the colonies were isolated, grown in a suspension culture containing 2 mL sterile LB media (Sigma, L7275) and ampicillin, and placed in 250 RPM and 37 °C shaker incubator for at

least 4 hours. Once the E. coli indicated enough growth (via opacity of the media), the plasmid DNA was isolated using the E.Z.N.A. Plasmid DNA Mini Kit I (Omega Bio-Tek, D6942) according to the manufacturer's guidelines.

The fragment tdTomato was amplified via Q5 PCR (New England BioLabs, M0491) per standard protocol except during the primer-specific steps. The custom forward and reverse oligo tdTomato primers (Thermo Fischer) in Q5 PCR were set to 68 °C and 30 s annealing steps and 72 °C and 43 s extension steps (due to GC content of primers and tdTomato's 1431 base pairs).

Plasmid base pair lengths were validated using 1 w/v % agarose gel electrophoresis utilizing 1% Tris-acetate-EDTA and purple 2-log DNA ladder (New England Bio Labs, N3200S) run at 90 volts for 75 mins. The desired DNA bands were excised. The DNA in the excised gel was extracted using QIAquick Gel Extraction Kit (Qiagen, 28706X4) per the manufacturer's guidelines. The DNA quality and quantity were determined via a spectrophotometer (Thermo Fischer, ND-2000). The PCR products and EGFP were digested using the restriction enzymes AgeI HF (New England BioLabs, R3552S) and EcoRI HF (New England BioLabs, R3101S) using standard protocols 37 °C overnight.

The next morning, the digest was inactivated at 65 °C for 20 mins on a preheated heat block. A gel electrophoresis was performed using 20% loading buffer (Quality Biological, 351-028-661), 10% SYBR gold (Invitrogen, S11494), the digested pLJM1-EGFP backbone, and tdTomato products. The gel extraction protocol was repeated to acquire the tdTomato insert and the pLJM1 backbone of the pLJM1-EGFP. Next, the DNA sticky ends of these products were ligated using standard protocols for T4 ligase (New

England BioLabs, M0101S) overnight at 16 °C in a MicroCooler (Boekel Scientific, 260010).

The next day, ligated products were transformed into stable competent E. coli (New England BioLabs, C3040I) per the manufacturer's protocol. After 2 hours in the shaker incubator suspended in SOC outgrowth media (New England BioLabs, B9020S), the transformation product (pLJM1-tdTomato) was spread on new agar plates and growth overnight. In the morning, isolated colonies were selected and grown in the shaker incubator until sufficient bacteria were grown in the media. Next, gel electrophoresis validated the pLJM1-tdTomato, tdTomato insert, and pLJM1-EGFP's base pair lengths. The resulting pLJM1-tdTomato band was excised, and the DNA was isolated. 1 μg of the final construct was sent as is or digested at the restriction sites, AgeI-HF and EcoRI-HF. The custom-made pCMV forward and tdTomato sequencing primers were reconstituted to 5 μM in 10 μL nuclease-free water. These samples and primers were sent to UAB's genetics core facility for Sanger sequencing for validation. The sequencing results were analyzed using SnapGene software (Dotmatics, Boston, MA) for appropriate base pairing and size.

Additionally, pLJM1-hTERT was constructed using the same methods and backbone of pLJM1-EGFP, but using pBABE-hygro-hTERT (Addgene, 1773) for the insert. The goal was to immortalize our own primary renal proximal tubule epithelial cells using this constructed plasmid. However, this project did not progress significantly because of the greater priority of other endeavors.

*2.3 Generation of Fluorescence and Stable Cell Lines*

The constructed pLJM1-tdTomato and purchased pLJM1-EGFP plasmids were used as the transfer plasmid in generating lentivirus. The transfection consisted of the envelope plasmid, pMD2.G (Addgene, 12259), and the packaging plasmid, psPAX2 (Addgene, 12260), which were kindly gifted from UAB's Dr. Jay Zhang's lab. Between 250-500 ng of each transfer, envelope, and packaging plasmid (at a ratio of 3:2:1 transfer: packaging: envelope) and between 1.0-2.5 μL of Lipofectamine 2000 (ThermoFisher, 11668027) were carefully added dropwise to 80% confluent Lenti-XTM HEK-293T cells of a 24-well plate containing in Opti-MEM$^{TM}$ medium. (Gibco, 31985070). Media containing lentivirus was collected and changed every other day for three days. The media from all wells and days were combined and placed into a 38.5 mL ultra-clear (UC) tube Beckman Coulter, 344058). To concentrate the lentivirus, the tubes were ultracentrifuged at 120,000 x g, 4°C, for 90 mins in an Optima XE-90 Ultracentrifuge (Beckman Coulter, A94471) in an SW 32 Ti swinging bucket rotor (Beckman Coulter, 369694). After centrifugation, the supernatant in the UC tubes was removed, and the UC tubes were inverted on a Kimwipe for 3-5 mins. 500 μL of ice-cold 1X DPBS(-) was added to the UC tubes and left to dissolve lentivirus for 20 mins before resuspending with a pipette. 100 μL volumes of lentivirus (containing EGFP or tdTomato) were aliquoted and stored at -80 °C until later use.

For the transduction, passage 3 hMEC-1s were plated on a 24-well plate and grown until approximately 70% confluency. Between 5-8 μg/mL of polybrene (Sigma, TR-1003-G) and a serial dilution of previously collected lentivirus were plated to optimize the protocol with this cell type and plasmids. Simultaneously in a second plate, a kill curve for

hMEC-1s and puromycin (ThermoScientific, A1113803) was conducted at concentrations between 0.5 to 1.5 μg/mL puromycin for 10 days.

*2.4 Computer-Aided-Design (CAD) for 3D Renal Proximal Tubule Tissue Chip*

The device was designed in-house using the 3D computer-aided design software Autodesk Inventor (San Francisco, CA). The device's overall dimensions are 35 mm in diameter and 27 mm in height. The tubule structure surrounded by the gel is 940 μm in diameter and 5 mm in length. The gel is housed within two non-separated compartments: the bottom compartment is 5 mm x 5 mm x 5 mm; the top compartment has a diameter of 14 mm and is 5.75 mm deep. The total volume of the gel compartment equates to approximately 500 μL of the hydrogel. From a superior view, the device contains four ports: two female-luer locks resembling syringe-needle ends and two male-luer locks as part of the intended printed design. The female-luer are the inlet and outlet ports for the tubular cells, whereas the two-male luers are for hydrogel addition in one and to displace air trapped within the chamber. Following hydrogel polymerization, the male-luers are connected to female-luer plugs and the two-female luers (inlet and outlets) are connected to Polypropylene 1.6 mm barbed tube ID luer lock couplings with teflon tape secured in between to seal the connected parts. Lastly, both the superior and inferior views of the device contain a 14 mm diameter circular indentation with depths of 1.75 mm and 500 μm, respectively.

*2.5 Computational Fluid Dynamics*

The magnitude and distribution of shear across the devices at the relevant flow rates was estimated using computational fluid dynamics (CFD) modeling software. Using the CAD model of the device, a finite element mesh of the channel fluid domain was generated

using Gmsh [9]. Mesh refinement was increased at all boundaries to account for steep velocity gradients. This mesh was imported into FeBio, which was used to set up, execute, and analyze the CFD model [10]. All device walls were assigned a no-slip boundary condition, and the outlet was assigned a zero fluid dilation boundary condition. At the inlet, the flow was implemented by assigning a prescribed velocity calculated from the desired flow rate. The fluid (cell culture media) was modeled as water at 37°C, a Newtonian fluid with a density of 1000 kg/m$^3$, bulk modulus of 2.1 GPa, and shear viscosity of 0.00069 Pa*s.

*2.6 3D Printed SLA Devices and Post-Processing*

The Inventor files are exported as .stl files and subsequently imported into PreForm software (Somerville, MA) to prepare the files for printing. In PreForm, the devices' orientation is set to 45° from the build platform, structural supports are added, the print resolution is set to 100 μm, and the build platform is mapped to print up to 12 devices in one session. At this time, the print can successfully be uploaded to the Stereolithography (SLA) Formlabs 2 printer (Formlabs, PKG-F2-WSVC-BASIC) using the biocompatible BioMed Clear Resin (Formlabs, RS-F2-BMCL-01). At the completion of the print, the devices are removed from the build platform, the printing supports are removed, and the devices are washed in the Form Wash (Formlabs, FH-WA-01) containing 99% isopropanol for 20 mins. As an extra precaution, additional 99% isopropanol is flushed through the hollow tubule channel using a squeeze bottle. Next, a 940 μm diameter silicone tubing is carefully pulled through the inlet and outlet channel with a few cm of tubing slack at each end. This tubing will later serve as the open channel for cells to create a tubular structure. These two steps are critical to ensure the device has a hollow channel prior to curing.

Lastly, the devices are placed in a 405 nm Form Cure (Formlabs, FH-CU-01) at 60 °C for 60 mins to completely cure the BioMed clear resin.

The 3D-printed devices must be processed further to prepare them for cell culture and perfusion. First, a very thin (approximately 200 μL) of wet PDMS was made at a 1:10 ratio of pre-polymer to cross-linking agent using methods standard to our lab and placed on the 14 mm circular indention on the inferior view of the device [11]. Applying a gentle force, a 12 mm circular cover glass (Electron Microscopy Sciences, 72231) is placed in this indentation containing wet PDMS and mated with the device. It is then placed upside down in a 70 °C oven for 30 mins or until the PDMS is completely cured around the cover glass. Then a larger volume of wet PDMS (approximately 500 μL) is spread evenly on the bottom to distribute a thin PDMS layer. The device is placed back into the oven for 30 mins. Next, the device is flipped 180° (to the superior view), where 200 μL of wet PDMS is carefully placed around the circular raised edges to insert the second 12 mm diameter coverslip. The PDMS around the superior cover glass is allowed cure for 30 mins. Like the anterior end, the superior view is sealed using 500 μL of wet PDMS and placed into the oven for 30 mins. The final 3D-printed SLA resin and PDMS device is now a closed vessel (excluding the sealable luer lock ports) with the 940 μm diameter placeholder tubing still in place. The devices are then sterilized using an autoclave before subsequent hydrogel and cell culture steps.

*2.7 Microvascular Fibrinogen-Gelatin Hydrogel*

The hydrogel comprises several components optimized for dense microvascular formation while maintaining appropriate mechanical properties such as elastic modulus. All reagents in the gel except Transglutaminase (TG) were reconstituted, aliquoted, and

stored in the appropriate storage conditions in advance. TG is highly temperature sensitive and should be made fresh for each experiment. Lyophilized human fibrinogen (EMD Millipore, 341578) was reconstituted at 80 mg/mL, aliquoted, and stored in -80 °C human fibrinogen but was a final concentration of 10 mg/mL in the gel. DPBS(-) (1X Dulbecco's PBS without calcium and magnesium) was warmed to 70 °C, and gelatin powder (type A; 300 bloom from porcine skin, Sigma) was added to yield 15 wt/vol% gelatin while vigorously stirring for 12 h at 70 °C. The gelatin was pH adjusted to 7.5 using 1 M NaOH and sterile filtered before aliquoting and storing at 4 °C. The final concentration of gelatin in the hydrogel was 1 w/v%. Next, a 250 mM $CaCl_2$ stock solution was prepared by dissolving $CaCl_2$ powder (Fisher Scientific, BP510) in DPBS(-) and had a final concentration of 2.5 mM in the hydrogel. On the day of the experiment, TG was constituted into a stock solution at a concentration of 60 mg/mL MooGloo TI Transglutaminase (Modernist Pantry, 1203), syringe filtered, and suspended in the hydrogel at a final concentration of 0.2 w/v% TG. Longer incubation times of TG improve the optical clarity of the final matrix [12]. Fibrinogen, gelatin, $CaCl_2$, TG, and DPBS(-) are warmed for 15 mins before proceeding. The reagents are combined in the following order: fibrinogen, DPBS(-), gelatin, $CaCl_2$, and TG and allowed to warm at 37 °C for 15 mins. During this step, hMEC-1:EGFP (or hMEC-1:tdTomato) and hDFs in culture are dissociated using trypsin and combined so that $1x10^6$ hMEC-1 and $2x10^6$ hDF are resuspended in 2 mL of total media. The combined hMEC-1 and hDF volume to gel for the final cell ratio was 2:1. Lastly, lyophilized thrombin from human powder (Sigma-Aldrich, T6884) was reconstituted at 500 U/mL using sterile DPBS(-) and stored at −20 °C. The thrombin aliquots were thawed immediately before use for 15 mins, resulting in a final concentration

of 2 U/mL. The addition of thrombin rapidly polymerized the gel, and the addition of the hydrogel was quickly added to the tissue chip devices in the gel channel. Each device (via the device's gel inlet port) was gently filled with 500 μL of cell-gel matrix. The two gel ports are now closed using a female plug luer lock, and the entire device is allowed to gel at 37 °C for 3 hours before beginning perfusion. The final concentrations of the cell-laden matrix were 10 mg/mL fibrinogen, 1 w/v% gelatin, 2.5 mM $CaCl_2$, 0.2 w/v% TG, 2 U/mL thrombin, with $1x10^6$ hMEC-1 and $2x10^6$ hDF.

*2.8 Perfusion Experimental Setup*

After 3 hours of gelation, the placeholder tubing of the device is removed so that media can be perfused. Each perfusion system or "loop" setup is independently perfused to ensure controlled experiment parameters. A single loop consists of silicone tubing, a media reservoir containing 6 mL of media, connection to a 6-channel MP2 Micro Peristaltic Pump (ESI, Golden, CO), associated pump-stop tubing, a one-way valve ahead of the device to minimize potential bubbles, and tubing outlet to a 3D printed reservoir cap to recirculate media. Between 12-14 experimental loops were run simultaneously via two 6-channel and one 2-channel peristaltic pump to achieve sufficient throughput. Experimental parameters for perfusion were established using the pump setup and pressure and flow sensors were used to ensure that the pressure within the flow loops was <10 mmHg and the shear stress was between 0.1-1.0 dyne/$cm^2$. For at least a day before the start of the experiment, the loop components were sterilized using ethylene oxide sterilization overnight to prevent contamination. Furthermore, the loops were assembled in a cell culture hood under sterile conditions, primed first with DPBS(-) to flush the systems of air, and then with loop media culture media as described below. Devices were then

transferred to each loop system and placed at a slight angle on the inlet side to prevent any potential bubbles from being trapped within the tissue chip. Once all loop assemblies were circulating with media, they were transferred to a large incubator and maintained in culture under conditions of 5% CO2 at 37°C.

Two supplements are added to EGM2 media perfusing the loop to enhance vascularization and prevent hydrogel degradation. First, a 40 μg/uL stock vial of lyophilized aprotinin from bovine lung (Sigma-Aldrich, A3428) was prepared and aliquoted so that EGM2 media would have a final concentration of 40 μg/mL aprotinin. Next, a 50 ng/μL stock of vascular endothelial growth factor (VEGF) (Sigma-Aldrich, V7259) was prepared and introduced into the medium to ensure that EGM2 media would have a final concentration of 50 ng/mL VEGF. Lastly, 1% of 100X antibiotic-antimycotic (Thermo Fisher, 15240062) was added to the media to prevent bacterial contamination. The cell-laded hydrogel was perfused at 0.1 dyne/cm$^2$ between 2-7 days before additional alterations were made.

*2.9 Proximal Tubule Seeding*

The hollow gel channel was washed gently with 1X DPBS(-) before adding stock iMatrix-511 (Advanced Biomatrix, 5344) diluted to 2.5 μg/mL in 100 μL of 1X DPBS(-)_ and placed within the channel for at least 45 mins [13]. During this time, hRPTEC-hTERT1 maintained in culture were dissociated and resuspended at a concentration of $2x10^6$ cells/100 μL. The iMatrix-511 ECM solution is carefully removed to add 100 μL of the cell suspension to the channel via the inlet port. The inlet and outlet ports are then secured with tubing connecting to each other to maintain a closed and sterile environment inside the device. The device is returned to the incubator and rotated 180° every 15 mins for 1

hour so that cells evenly attach in the hollow channel. The device is left in the incubator for an additional 3 hours to ensure cellular attachment before perfusion.

A simple flow loop using the protocols described earlier was performed, except that loop media contained F:12-hTERT cell culture media supplemented with 1% antibiotic-antimycotic and 2.5 μg/mL aprotinin supplements. Devices were then transferred to each loop system and placed at a slight angle on the inlet side to prevent any potential bubbles from being trapped within the tissue chip. Once all loop assemblies were circulating with media, they were transferred to a large incubator and maintained in culture under conditions of 5% CO2 at 37°C.

*2.10 Confocal Microscopy*

The proximal tubule and microvascular devices were fixed with 4% paraformaldehyde in PBS for 20 min, washed with DPBS(-) 3X 5 mins. Devices stained for phalloidin rhodamine (Invitrogen, R415) were permeabilized with 0.5% Triton X-100 (Fisher Scientific, Fair Lawn, NJ, USA) for 10 min at room temperature. Because of the thickness of the hydrogel, ProLong™ glass antifade mountant (Thermo Scientific, P36980) was used to help penetrate the gel for z-stack imaging. Devices were imaged using a Nikon A1R Confocal Microscope (Nikon Instrument Inc., USA) located in UAB's High-Resolution Imaging Facility.

## 3. Results

*3.1 Generation of Stable Cell Lines for Utilization in Tissue-Engineered Peritubular Microvascular Networks*

The starting commercial plasmids pLJM1-EGFP and pCSCMV:tdTomato were selected and designed with the appropriate promoters for lentivirus transfection (Figure

1A). Throughout the plasmid construction process, gel electrophoresis was utilized to ensure the correct band size of the starting plasmids, backbones, and inserts (Figure 1B). Sanger sequencing confirmed the accuracy of the constructed plasmids and detected no mismatches for several hundred base pairs (until Sanger sequencing becomes less reliable after 600 nucleotides) [14]. Upon Sanger validation, pLJM1-EGFP and pLJM1:tdTomato were subsequently transfected into HEK 293T cells to amplify the lentivirus. Over 70% of the cells positively express EGFP or tdTomato under epifluorescence (Figure 1D). The harvested lentivirus was, in turn, traduced into the desired human microvascular cell line, hMEC-1, with greater than 50% positive expression of EGFP or tdTomato (Figure 1E). The positive hMEC-1-EGFP or hMEC-1-tdTomato were isolated and amplified in cell culture for subsequent use to construct tissue-engineered microtubules.

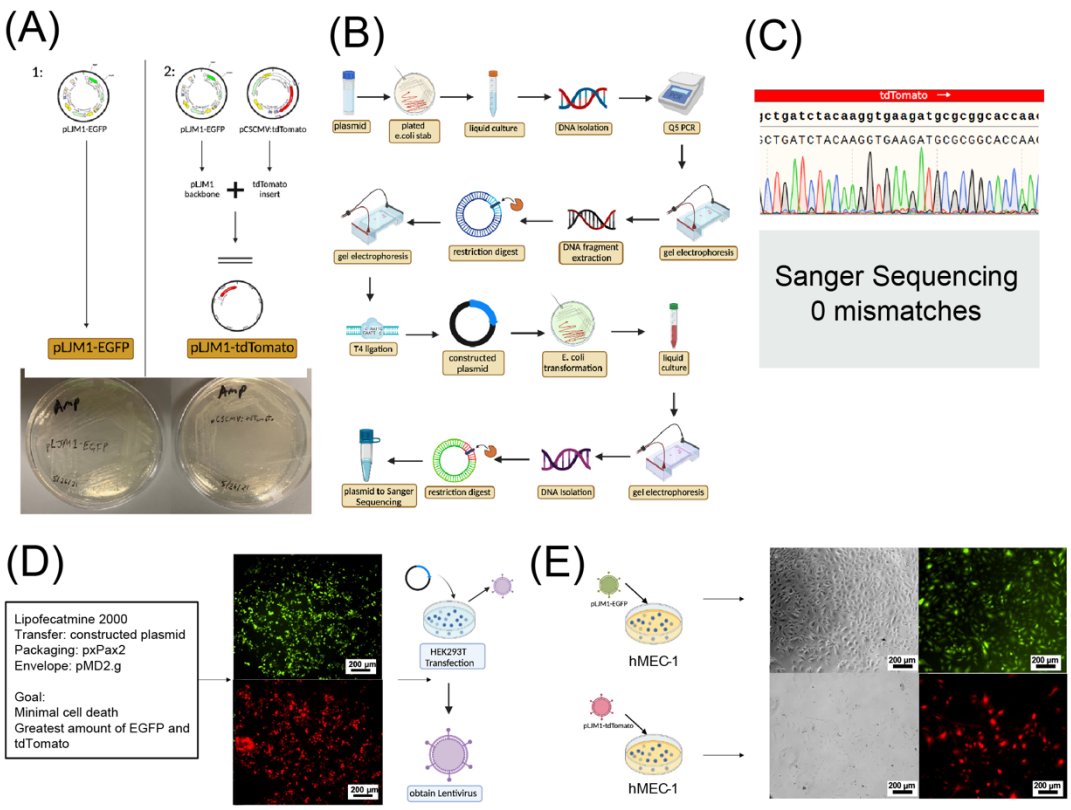


**Figure 1. Overview of the process and validation of Stable Cell Lines Generated for Tissue-Engineered Peritubular Microvascular Networks.** (A) Starting commercially available plasmids and constructed plasmids. (B) The general workflow to construct pLJM1:tdTomato. (C) Validation of constructed pLJM1:tdTomato using Sanger sequencing. (D) Transfection of pLJM1:tdTomato into HEK293T cells to generate lentivirus and verified using epifluorescence. (E) Lentivirus transduced into microvascular endothelial cell line hMEC-1 and verified using epifluorescence. Created with BioRender.com.

*3.2 Engineering Technologies to Generate Human Renal Proximal Tubule Tissue Chips*

Several designs and iterations of a 3D-printed PT tissue chip were considered, but the final design is described as follows. Autodesk Inventor was used to design the 3D renal proximal tubule chip (Figure 2A). Briefly, the proximal tubule chamber was designed to

have a diameter of 35 mm and a height of 27 mm. Two ports were incorporated for fluid flow in contact with the engineered proximal tubule structure, and two additional ports were incorporated to introduce the hydrogel (Figure 2B). The designed devices were successfully 3D printed using a Formslab SLA printer and post-processed with PDMS to add coverslips (Figure 2C) to the open bottom end to achieve a sealed device that is compatible with imaging using a confocal microscope. A 940 µm in diameter silicone tubing was fed through to use a placeholder to define the proximal tubule prior to adding gelatin-fibrin hydrogel to fill the device's volume (Figure 2C). The tubule was oriented less than 1 mm from the anterior side of the device's coverslip for more reliable confocal imaging (Figure 2D). Lastly, shear stress was determined using FEBio CFD software and simulations indicate that the shear stress within the design remained within physiological levels (Figure 2E).

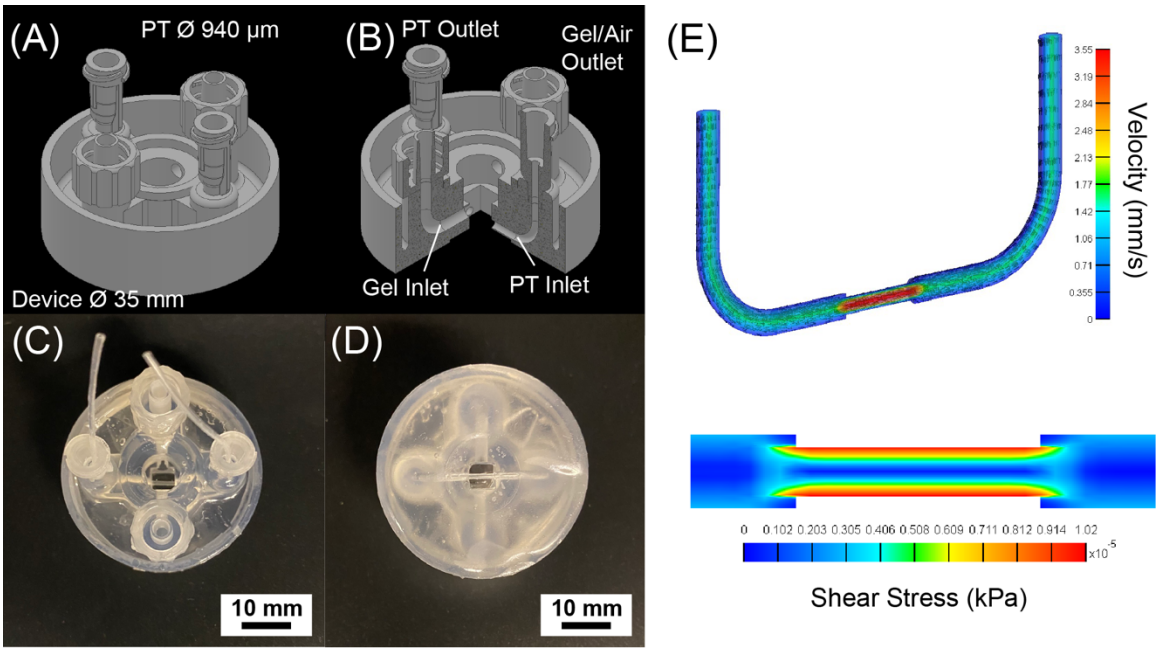


**Figure 2. Computer-Aided-Design (CAD), 3D Printing Technologies, and Computational Fluid Dynamics (CFD) modeling software to generate Human Renal**

**Proximal Tubule Tissue Chips.** Inventor CAD program models showing (A) orthogonal view (B) and 3/4 section view of in-house designed tissue chip containing four ports for seeding and fluid flow. (C) Superior view and (D) anterior view of the 3D printed device with post-processing procedures. (E) FEBio CFD modeling of the channel to visualize shear stress at the specified flow rates.

*3.3 Protocol and Timeline Considerations to Co-Culture hRPTEC-hTERT, hMEC-1, and hDFs in Gelatin-Fibrin Hydrogel*

In generating the protocol to co-culture hRPTEC-hTERT, hMEC-1, and hDFs, the media, hydrogel, and timeline were important considerations in developing the 3D PT tissue chip. Previous studies by our lab (not shown) and other groups indicate dense microvascular formations and confluent PT lumens starting at 7 and 5 days, respectively. A combination of working protocols was utilized to ensure that the cell seeding conditions resulted in optimized tubular structures and microvascular structures (Figure 3A). As discussed in the methods section, hMEC-1, and hDFs encapsulation within gelatin-fibrin incorporated the first two cell types to form the MV networks. Following 48 hours in culture, hRPTEC-hTERTs were introduced, and perfusion was initiated (Figure 3B). After at least 5 days with media perfusion of the PTs (8 days overall), the loops are removed and analyzed.

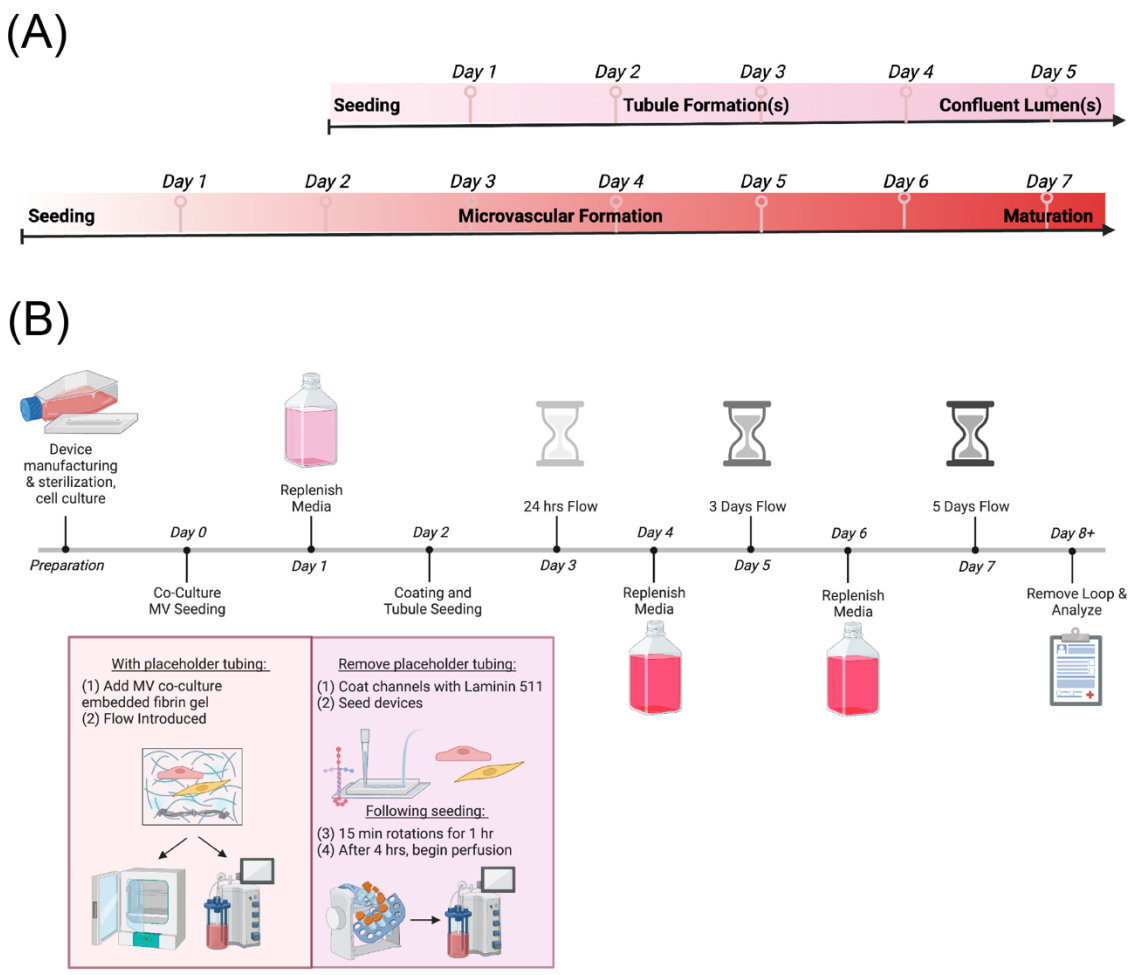


**Figure 3. Workflow to encapsulate hRPTEC-hTERT, hMEC-1, and hDFs in Gelatin-Fibrin Hydrogel.** (A) Timeline of confluent proximal tubule lumens and maturation of microvascular network over 5 and 7 days, respectively. (B) Cumulation of protocols to generate 3D proximal tubules with surrounding microvascular networks. Created with BioRender.com.

*3.4 Imaging Studies of Human Renal Proximal Tubule Tissue Chips Indicate Microvascular Networks and Confluent Lumens*

To optimize the naturally forming microvascular networks of hMEC-1 and hDFs, gelatin-fibrin formulations at varying fibrinogen concentrations between 10-25 mg/mL were investigated and evaluated after 10 days (Figure 4A). By only altering the fibrinogen

concentration, the microtubular network density formed in an inverse relationship. The final concentration of 10 mg/mL fibrinogen was determined superior to higher formulations. Other variables of the gelatin-fibrin hydrogel, such as gelatin concentration, cell number, endothelial-to-fibroblast cell ratios, incubation times, etc. were investigated to optimize network densities and fine-tune the protocol (not shown). To better visualize these networks, confocal microscopy z-stacks looking at F-actin, EGFP, and DAPI in the cell-laden hydrogel show dense microvascular networks in 7d (Figure 4B). Qualitatively, the model shows preliminary evidence that highly interconnected microvascular networks can be formed around a tubular structure seeded with hRPTECs-hTERTs mimicking the architecture seen in-vivo and maintained in culture under physiological shear stress (Figure 5A-B).

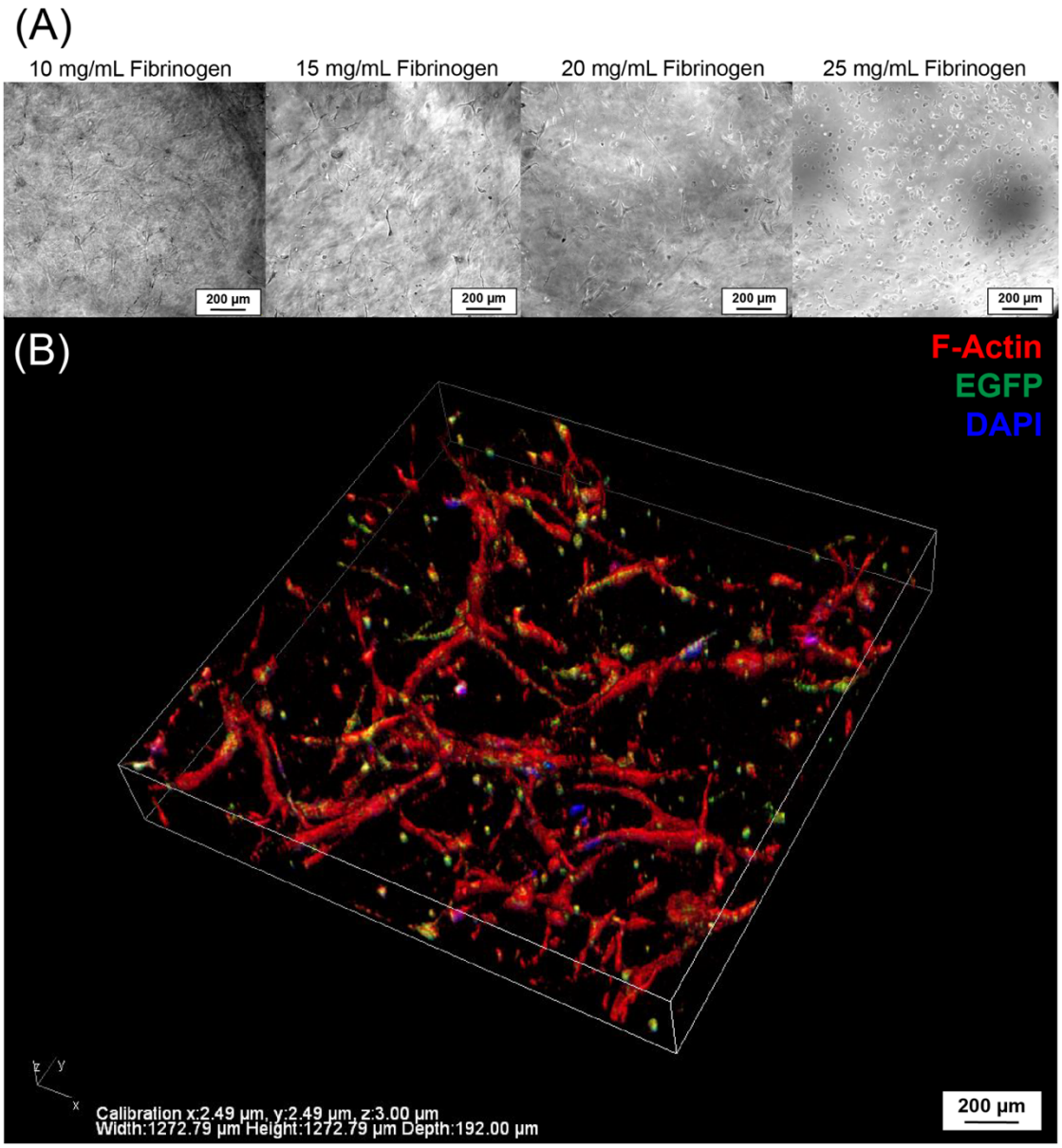


**Figure 4. Visualizations of microvascular peritubular networks in Gelatin-Fibrin Hydrogel consisting of a co-culture fluorescently labeled hMEC-1 and hDFs.** (A) Brightfield images of gelatin-fibrinogen hydrogel optimization using varying fibrinogen concentrations to assess network density after 7 days with the greatest density at 10 mg/mL of fibrinogen. (B) Confocal microscopy z-stack of dense hMEC-1-EGFP and hDFs co-culture networks after 7 days via cytoskeleton F-actin (both cell types), EGFP (of endothelial nuclei), and DAPI (both cell types).

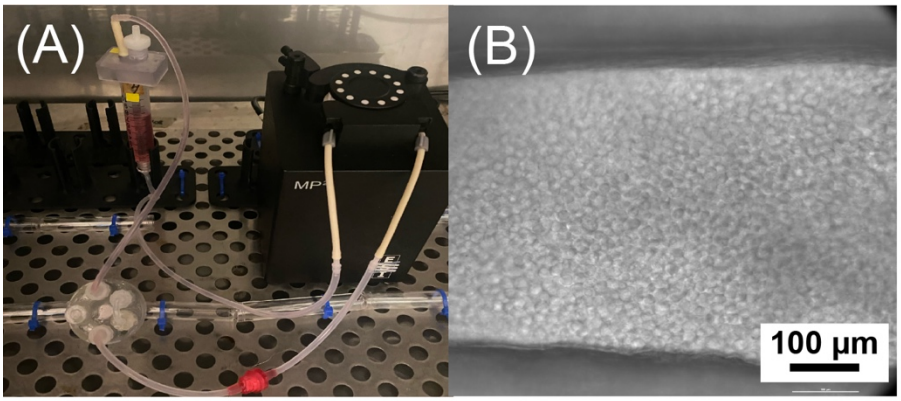


**Figure 5. hRPTEC-hTERTs Forming Confluent Tubules after Five Days of Fluidic Shear Stress.** (A) Example of a 3D perfusion system with media reservoir, microfluidic pump, and 3D printed devices containing hRPTEC-hTERTs encapsulated in hMEC-1-hDFs-gelatin-fibrin hydrogel. (B) Brightfield image of confluent hRPTEC-hTERTs after five days of perfusion.

## 4. Discussion and Conclusion

This chapter focuses on our efforts to generate a physiologically relevant model of the renal PT. Existing models of renal PTs fail to model the complex architecture associated with the PT and associated perivascular networks and replicate PT function. Construction of a model of the PT involves several challenges associated with organizing the multiple cell types into specific structures, visualizing different cells during and after construction and challenges associated with profiling live cells within complex tissue structures. The work presented in this chapter focuses on the preliminary work performed in terms of creating labeled cell lines and the design and fabrication of devices that allow for both replication of the complex architectures and their visualization and integration of the tubular structure and surrounding microvascular networks. The presented results provide proof that the proposed approach is feasible and PT models constructed using described

approaches can indeed be realized. Subsequent efforts are needed to characterize the function of the engineered PT extensively.

To enable visualization of microvascular networks and distinguish microvascular endothelial cells from cells associated with adjacent larger vessels, we generated fluorescently labeled endothelial cell lines. The results of this study demonstrate effective plasmid constructions and transfections to produce lentivirus, which were transduced into primary cells to generate stable cell lines containing fluorescent proteins EGFP or tdTomato. The choice to have two endothelial cell types fluorescently labeled was to differentiate individual cell types in the capillary network (ex. green) and the parental vascular channel (ex. red) to identify angiogenic sprouts and the formation of open lumens [4]. Utilizing these cells within renal tissue chips will help visualize different vascular components and study the development of interconnected microvascular networks.

Creating a PT chip involves addressing several challenges associated with enabling the construction of desired architectures and associated fluid flow, ensuring that cells and engineered tissues can be housed in an environment that protects the constructs from contamination, and finally, ensuring visualization of both tubular and microvascular components. Special design considerations ensured that a sealed compartment was created to house the ECM hydrogel to prevent contamination and leaks. Second, the transparency of the flow chamber was a major consideration and incorporating a thin coverslip at the bottom of the device enabled microscopic evaluation using a confocal microscope. Third, modular connectors with luer lock fittings were used to connect the inlet and outlets with the tubing associated with the perfusion loops. Finally, we ensured that all materials used to construct the device were biocompatible and potentially autoclavable to enhance

sterility. Lastly, the device is designed as a modular device with a compact size and the ability to fit into standard tissue culture plates for subsequent adaptation for higher throughput studies. Three-dimensional printing conducted in this study enabled relatively rapid construction of devices and extensive control of specific design elements such as the luer lock fitting and open transparent bottom. Most microfluidic devices are fabricated through photolithography to create silicon molds and make an impression on PDMS. Although useful for some research questions, there is a greater turnaround time from design, fabrication, testing, and validation using PDMS-silicon molds. The 3D printing drawing software and printing methods allowed several design iterations and higher throughout device manufacturing.

Endothelial cells, supporting cells, growth factors, ECM-mimicking biomaterials, and mechanical stresses are crucial for developing microvascular networks. These elements, when combined appropriately, create a perfusable and self-assembled microvasculature [15]. Protocols from renal-centric and microvascular-centric research groups were evaluated and optimized for the purpose of this aim (Figure 3) [8, 12, 16-19]. For example, adding human VEGF and aprotinin in the cell culture media assisted in self-maturation and inhibiting fibrin hydrogel degradation (Figure 4) [20, 21]. Originally, this project utilized gelatin methacryloyl (GelMA) as its hydrogel. The advantage of a GelMA, compared to others, such as fibrin, is the ability to fine-tune and optimize its mechanical properties by changing the GelMA and photo-initiator concentrations, polymer degree of functionalization, and 365 nm UV-A crosslinking intensity and time [22]. The elastic modulus of the renal cortex is approximately 4 kPa and could be more readily achieved using synthetic or hybrid (natural and synthetic) hydrogels such as GelMA [23]. After

numerous experiments, we found that the cellular attachment and proliferation rates of hRPTEC-hTERT on GelMA did not reach 100% confluency, especially in 3D space such as the engineered proximal tubule. This is likely due to the toxic nature of high concentrations of photoinitiators like Irgacure 2959 and lithium phenyl-2,4,6-trimethylbenzoylphosphinate (LAP) needed to crosslink GelMA to the appropriate elastic modulus [24]. Therefore, we proceeded with a modified gelatin-fibrin hydrogel that has demonstrated effectiveness (Figure 4). Fibrin is the desired scaffold for many tissue engineering labs for its ability to control the degradation [20]. Based on more extensive mechanical studies of different gelatin-fibrin formulations, we estimate that our hydrogel maintained a shear modulus and stiffness of approximately 5 kPa [8, 12, 16-19, 25]. Therefore, we do not foresee major mechanical property drawbacks in the gelatin-fibrin hydrogel compared to the GelMa that we have used previously.

Taken together, our efforts to engineer a 3D model of the proximal tubule are highly innovative for the following reasons: (A) Replication of 3D renal tubular architecture with peritubular vascular networks to potentially increase secretion and reabsorption functions of the proximal tubule, and (B) Perfused capillary networks through a natural maturation process that enables a more complex and physiologically relevant vascular co-culture with 3D PT epithelial tubules. We acknowledge that greater validation and experimentation of our tissue chip is necessary to validate our device, and our next steps are detailed in Chapter 5. However, we will continue to test our hypothesis that developing a 3D RPTC that combines a 3D proximal tubule and peritubular vascular will increase physiological relevance and selective transport seen in vivo for the faithful replication of normal and pathophysiology of the proximal tubule.

Reference:


1. Vermue, I.M., et al., *Renal Biology Driven Macro- and Microscale Design Strategies for Creating an Artificial Proximal Tubule Using Fiber-Based Technologies.* ACS Biomaterials Science & Engineering, 2021. **7**(10): p. 4679-4693.
2. Sobrino, A., et al., *3D microtumors in vitro supported by perfused vascular networks.* Scientific Reports, 2016. **6**(1): p. 31589.
3. Tronolone, J.J. and A. Jain, *Engineering New Microvascular Networks On-Chip: Ingredients, Assembly, and Best Practices.* Advanced Functional Materials, 2021. **31**(14): p. 2007199.
4. Lee, V.K., et al., *Generation of Multi-Scale Vascular Network System within 3D Hydrogel using 3D Bio-Printing Technology.* Cell Mol Bioeng, 2014. **7**(3): p. 460-472.
5. Eaton, D.C. and J. Pooler, *Vander's Renal Physiology, 9e*. 2018, McGraw-Hill Education LLC.: New York, N.Y.
6. Abdul-Ghani, M.A., L. Norton, and R.A. Defronzo, *Role of sodium-glucose cotransporter 2 (SGLT 2) inhibitors in the treatment of type 2 diabetes.* Endocr Rev, 2011. **32**(4): p. 515-31.
7. Wright, E.M., B.A. Hirayama, and D.F. Loo, *Active sugar transport in health and disease.* J Intern Med, 2007. **261**(1): p. 32-43.
8. Lin, N.Y.C., et al., *Renal reabsorption in 3D vascularized proximal tubule models.* Proceedings of the National Academy of Sciences, 2019. **116**(12): p. 5399-5404.
9. Geuzaine, C. and J.-F. Remacle, *Gmsh: A 3-D finite element mesh generator with built-in pre- and post-processing facilities.* International Journal for Numerical Methods in Engineering, 2009. **79**(11): p. 1309-1331.
10. Maas, S.A., et al., *FEBio: Finite Elements for Biomechanics.* Journal of Biomechanical Engineering, 2012. **134**(1).
11. Donoghue, L., C. Graham, and P. Sethu, *Acute Response of Engineered Cardiac Tissue to Pressure and Stretch.* Cells Tissues Organs, 2022.
12. Kolesky, D.B., et al., *Three-dimensional bioprinting of thick vascularized tissues.* Proceedings of the National Academy of Sciences, 2016. **113**(12): p. 3179-3184.
13. Zhang, H., et al., *The impact of extracellular matrix coatings on the performance of human renal cells applied in bioartificial kidneys.* Biomaterials, 2009. **30**(15): p. 2899-911.
14. Kircher, M. and J. Kelso, *High-throughput DNA sequencing – concepts and limitations.* BioEssays, 2010. **32**(6): p. 524-536.
15. Tsao, C.W., et al., *Heart Disease and Stroke Statistics—2022 Update: A Report From the American Heart Association.* Circulation, 2022. **145**(8): p. e153-e639.
16. Hiratsuka, K., et al., *Organoid-on-a-chip model of human ARPKD reveals mechanosensing pathomechanisms for drug discovery.* Science Advances, 2022. **8**(38): p. eabq0866.
17. Aceves, J.O., et al., *3D proximal tubule-on-chip model derived from kidney organoids with improved drug uptake.* Scientific Reports, 2022. **12**(1): p. 14997.
18. Homan, K.A., et al., *Flow-enhanced vascularization and maturation of kidney organoids in vitro.* Nature Methods, 2019. **16**(3): p. 255-262.

19. Homan, K.A., et al., *Bioprinting of 3D Convoluted Renal Proximal Tubules on Perfusable Chips.* Scientific Reports, 2016. **6**(1): p. 34845.
20. Ye, Q., et al., *Fibrin gel as a three dimensional matrix in cardiovascular tissue engineering.* Eur J Cardiothorac Surg, 2000. **17**(5): p. 587-91.
21. Boucard, E., et al., *The degradation of gelatin/alginate/fibrin hydrogels is cell type dependent and can be modulated by targeting fibrinolysis.* Front Bioeng Biotechnol, 2022. **10**: p. 920929.
22. Loessner, D., et al., *Functionalization, preparation and use of cell-laden gelatin methacryloyl-based hydrogels as modular tissue culture platforms.* Nat. Protoc. Nature Protocols, 2016. **11**(4): p. 727-746.
23. Bensamoun, S.F., et al., *Stiffness imaging of the kidney and adjacent abdominal tissues measured simultaneously using magnetic resonance elastography.* Clinical imaging, 2011. **35**(4).
24. Xu, H., et al., *Effects of Irgacure 2959 and lithium phenyl-2,4,6-trimethylbenzoylphosphinate on cell viability, physical properties, and microstructure in 3D bioprinting of vascular-like constructs.* Biomed Mater, 2020. **15**(5): p. 055021.
25. Mooney, R., B. Tawil, and M. Mahoney, *Specific Fibrinogen and Thrombin Concentrations Promote Neuronal Rather Than Glial Growth When Primary Neural Cells Are Seeded Within Plasma-Derived Fibrin Gels.* Tissue engineering. Part A, 2009. **16**: p. 1607-19.

# CHAPTER 5

# PUBLIC HEALTH RELEVANCE, FUTURE DIRECTIONS, & CONCLUSIONS

# 1. Greater Public Health Relevance

## *1.1 Impact of Organs-on-a-Chip on Legislation: Modernization Act 2.0*

In 1937, over one hundred patients died from renal failure after taking the sulfa antimicrobial drug, sulfanilamide, in a liquid "elixir" form, as it was dissolved in the diluent diethylene glycol [1]. Later known as the "Elixir Sulfanilamide disaster of 1937," it became one of the most significant mass poisonings of the 20$^{th}$ century. Yet its implications on the and modifications to the Food and Drug Administration (FDA)'s protocols and the pharmaceutical and research communities are unbeknownst to many. The disaster prompted the once stagnant (approx. since 1933) bill, titled the Federal Food, Drug, and Cosmetic Act, to quick action and passage in Congress by 1938 [2]. Its primary purpose was to make interstate commerce of adulterated and misbranded food, drug, medical devices, and cosmetics unlawful. The act intended to revise the 1906 regulations initiated in response to harmful practices in the meat packing industry. However, only after the Elixir Sulfanilamide disaster did the act include pharmaceutical manufacturers to disclose product safety before drug distribution [3]. Furthermore, and of greatest importance to this thesis, it mandated pharmaceutical companies submit a new drug application (NDA) report to the FDA indicating drug safety via animal testing. Although animal testing and efficacy standards were not standardized until later amendments (as late as the 1960s), the 1938 legislation drastically changed the drug discovery and approval process for years to come.

Since the Federal Food, Drug, and Cosmetic Act of 1938 was enacted, measures to ensure the safety of patients with novel therapeutics have made tremendous strides. But simultaneously, there is an increasing financial cost. Today's rising national healthcare cost can partially be attributed to the high expense and failure rates of screening therapeutics

prior to and during early clinical trials. The current pathway for drug discovery is associated with costs of $2.55 billion and between 10-15 years of development for a single drug to reach the market [4-6]. The current process that relies heavily on animal models is also susceptible to inaccurate predictions of human physiological responses, particularly those pertaining to age, sex, and patient-specific phenomena [7]. The challenges in predicting drug toxicities and efficacies are attributed to inherent interspecies differences in drug-metabolizing enzyme activities and cell-type-specific sensitivities to toxicants [8]. The financial burden alone to combat chronic and end-stage kidney disease through Medicare spending in 2019 was $124 billion [9]. In contrast, the entire NIH budget for the same fiscal year was $39 billion [10]. This staggering discrepancy between costs associated with treatment and research efforts focused on drug safety calls into question the efficiencies in the existing healthcare system. As the prevalence of kidney disease continues to rise, it is important to address the financial burden associated with disease management and drug development to ensure that all individuals have access to the necessary treatments and care.

The bipartisan FDA Modernization Act 2.0 seeks to address several issues currently affecting the country's healthcare system. President Joe Biden signed it into law in December 2022, and it is the first major change in FDA animal testing policies since 1938. Most notably, the bill allows for alternatives to animal testing for purposes of drug and biological product application [11]. The emergence of new technologies such as tissue chips, microphysiological systems, and organoids now provide viable alternatives to our reliance on animals and traditional cell culture models. The Modernization Act 2.0 reflects how other federal agencies, including the National Institutes of Health, Defense Advanced

Research Projects Agency, and the Food and Drug Administration, already endorse the development of Human Tissue Chips or Organs-on-Chips that maintain tissue/organ-level structure and function [12]. There are ongoing efforts to overcome the shortcomings of the existing drug discovery process and accelerate the translation of basic science discoveries into clinical practice with these models. Tissue Chips can be used to build disease models and test drugs or combined with other Tissue Chip Models to create Human Microphysiological Systems (MPS) or Human Body-on-a-Chip platforms. The integration of these chips will recreate critical system-level interactions to predict whether a drug or vaccine is effective and safe in humans [13]. Human Tissue Chip Models and MPS can be created using patient-derived cells and represent the future of personalized medicine. In summary, the legislative changes to the FDA drug development policies directly reflect the potential and validity of tissue chips in modern medicine and publicly acknowledge the emergence of these promising technologies.

*1.2 Impact of Organs-on-a-Chip and Mechanobiology: Pharmaceutical Perspectives*

During the past several decades, there has been tremendous growth in the study of mechanobiology, which focuses on the crucial role that physical forces play in controlling biological processes [14]. Several drugs in the drug development pipelines are increasingly moving beyond symptomatic control and toward preventing disease progression in both a patient-centric and disease-specific approach that require replication of physical stresses associated with the disease state [15]. Tissue chips incorporating mechanical stresses like shear, pressure, and stretch will increase the predictive power of pre-clinical studies to accurately model human physiology. Although systemic crosstalk is a major drawback of organ-on-a-chip technologies, these issues can be addressed via the integration of

additional complexity in the form of multi-organ chips and microphysiological systems to recreate critical interactions associated with the specific drug or disease state. These technologies have the financial backing of regulatory agencies and major pharmaceutical giants. Their widespread use for pre-clinical drug screening will validate these models as reliable predictors of drug toxicity and establish their legitimacy.

In 2017, thirteen pharmaceutical companies (AstraZeneca, Bristol-Myers Squibb, Pfizer, etc.) and partners at the NIH compiled a consensus view on the progression strategy to facilitate and accelerate the adoption of tissue chips [15]. Their impact statement addresses the technology's abilities to assess properties of disposition, efficacy, and safety and how they can support mechanistic studies which aim to resolve challenges later in development (e.g., assessing the human relevance of a liability identified in animal studies). Furthermore, providing roadmaps for more rapid unification between innovators and end users alike (Figure 1).

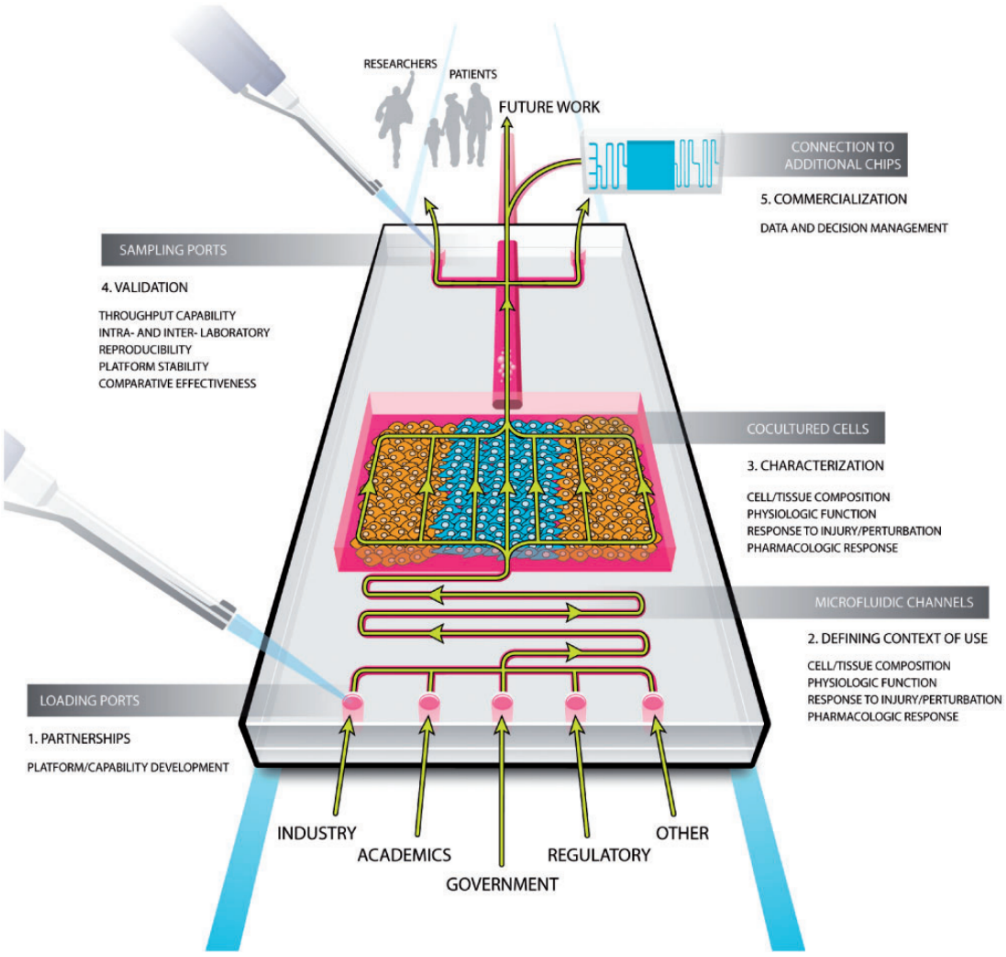


**Figure 1. Pictorial representation of the key aspects of the roadmap.** Reproduced with permission from the SAGE Publication [15].

The NIH and pharmaceutical companies agreed on the five major aspects: (a) partnerships, (b) the context of use, (c) characterization, (d) validation and commercialization to maximize efficiency, and (e) utilization. First was establishing successful partnerships as a crucial first step and a shared responsibility between the innovators and the end users, such as pharmaceutical scientists, in the form of multi-party frameworks (e.g., consortia). Context of use defines that said partnerships should provide examples of scenarios where these technologies may be used, technical standards, and methods for characterizing and validating products to promote quick adoption by end users,

generating near-term value, and developing industry confidence. This includes clear understanding of the best stage of drug development at which tissue chips models are best be utilized (Figure 2)

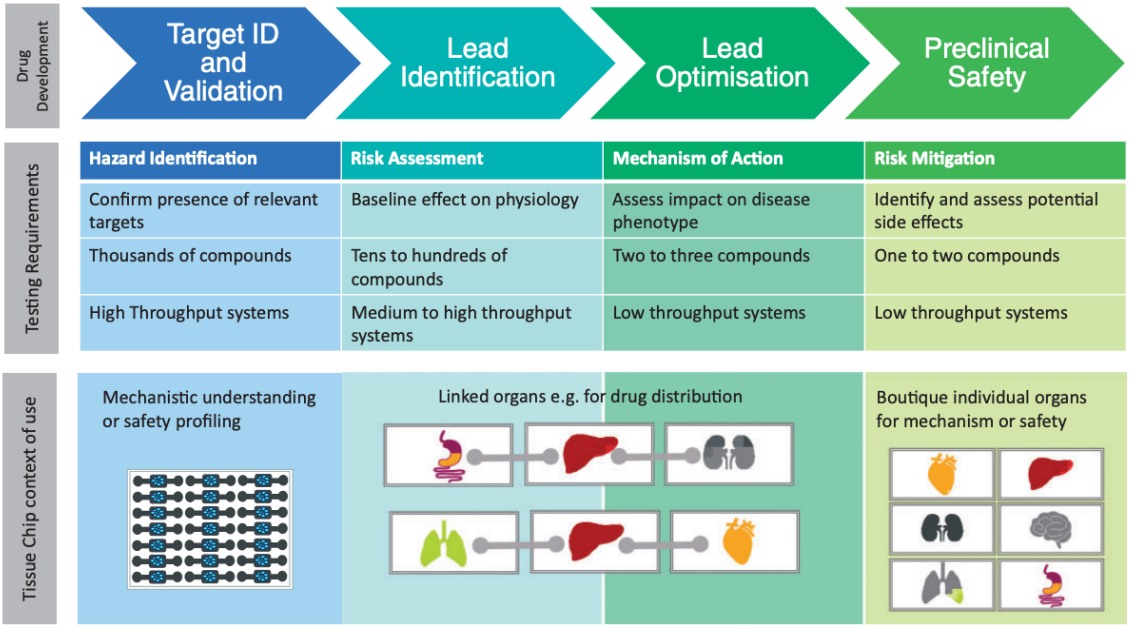


**Figure 2. Illustration of The Purpose Of Early Drug Development Phases and How The Context Of The Use of A Tissue Chip Will Vary Depending Upon The Phase In Which It Is Intended To Be Used.** Boutique assays and/or linked systems can be used in other phases, too, but at least in the first generation of these devices, the proposed deployment is preferred. Reproduced with permission from the SAGE Publication [15].

Characterization of tissue chips aims to increase confidence via representation of relevant in vivo biology, responses to injury, pharmacology, and a capacity to relate in vitro cellular and organ level biology to more integrated and phenotypic in vivo responses. Validation assesses analytical performance through throughput capability, biological platform stability, drug-device interactions, and inter- and intra-lab reproducibility. One solution to address this issue is the recently proposed and financed Third Party Testing

Centers by National Center for Advancing Translational Sciences (NCATS), which provides an opportunity for thorough analytical validation needed by the pharmaceutical sector without hindering academic innovators who are still improving their platforms. Lastly, the commercialization of tissue chips can be viewed in two contexts: a service that is outsourced to a provider or as a commodity available for purchase. Broader screening applications of TCs would likely appear as a product platform, whereas mechanistic applications could be financially viable under a fee-for-service model. Long-term development considerations for each of these approaches will vary based on the biological and analytical complexity of the system, throughput, cost, and engineering infrastructure required to support them. In closing, it is unlikely that a novel therapeutic discovered in the lab today will be expedited through the use of these novel drug discovery process in their current stage of development. Rather, in the coming decades, researchers and biopharma will continue technology development, standardize and validate different platforms and establish these platforms as an integral part of the drug discovery process in due course.

## 2. Future Directions

### *2.1 Acute Response of Engineered Cardiac Tissue to Pressure and Stretch*

Our current study evaluated bioengineered cardiac tissue constructs within the experimental hemodynamic systems subject to isolated pressure and stretch stimuli for ~ 24 hours. Results from this study suggest that exposure to acute pressure and stretch stimuli elicits injury responses; however, the type of responses activated were similar regardless of the type of stress. Moving forward, this study can be advanced in various directions: (A) Repeat this study over a more extended time period. Within 24 hours, we observed changes

in morphological, gene expression, and soluble factors; however, many were not statistically relevant. Furthermore, many cardiac phenotypes associated with PO and VO result from prolonged cardiovascular disease and may require prolonged exposure to stress to observe pathophysiological tissue remodeling. (B) PO and VO involve pathological levels of stress. Application of elevated levels of pressure and stretch to the engineered tissues would likely elicit more dramatic changes associated with pathophysiological tissue remodeling in-vivo. (C) To overcome the shortcomings associated with the use of h9c2 cells a rat myoblast cell line, the relevance to the human heart can be enhanced via the inclusion of human induced pluripotent derived cardiomyocytes. The shortcomings associated with the use of non-native extracellular matrix can potentially be addressed via (D) use of ex-vivo cardiac tissue (from porcine or rodent myocardial sections) or decellularized cardiac tissue re-seeded with human induced pluripotent derived cardiomyocytes or (E) the use of cardiac tissue constructs constructed using fused human induced pluripotent derived cardiomyocytes spheroids that spontaneously generate native ECM, thereby avoiding the need for non-native ECM. Several of these shortcomings are already addressed in ongoing projects with the Sethu research lab.

*3.2 Shear Stress 2D Renal Proximal Tubule Tissue Chip*

In chapter three, we demonstrated the use of both non-invasive (i.e., cytokine arrays) and invasive methods (i.e., Nanostring) to profile changes in renal proximal tubule epithelial cells within our renal proximal tubule chip model. We also for the first time performed our studies within the upper and lower limits of shear stress associated with the proximal tubule. Major shortcomings with prior studies include the relevance of the choice of proximal tubular cells (i.e., HK-2, MDCK canine cells), evaluation of cells under non-

physiological shear stress (single magnitude), and dosing with drugs in vitro studies at inappropriate levels. The renal proximal tubule chip was designed to address these shortcomings and conduct toxicity screenings at relatively high throughput. To achieve initial validation, we utilized drugs with known levels of nephrotoxicity (low, medium, and high). We categorized a drug's nephrotoxic effects based on its relative PT damage. "Low": drugs that are not harmful to the kidney; "Intermediate": drugs that are considered damaging to other parts of the kidney (glomerulus, distal tubule); "High"; direct PT toxicity or via a secondary mechanism such as crystal formation. Subsequent studies detailed in chapter 3 utilized only drugs associated with 'low' nephrotoxicity, dexamethasone (100 μM) and probenecid (100 μM) and high nephrotoxic drugs, cisplatin (39 μM) as this thesis's time frame, did not allow additional studies with drugs with 'intermediate' nephrotoxicity like amphotericin-B and lithium salts or high drug gentamicin. Therefore, suitable next steps for this project could potentially include expanding the list of drugs with known nephrotoxicity across a range of concentration levels. Furthermore, in partnership with the Biostatistics Core within the Center for Clinical and Translational Sciences (CCTS) and the inclusion of additional measurements, such as the evaluation of drug based on changes in TEER and cytokines, a Nephrotoxic Risk Score for each drug could be developed. Specifically, the data from the LDH assay can be combined with time-varying TEER measurements and quantitative evaluation of differences in pro-inflammatory cytokines normalized to controls (no drug vs. drug) at different time points to identify specific cytokines of interest and use the relative change to generate a weighted risk score.

*2.3 3D Renal Proximal Tubule Tissue Chip with Associated Microvascular*

With the model developed in chapter four, more extensive validation would strengthen our hypothesis that adding a 3D peritubular vascular network to the 3D RPTC enhances physiological relevance and selective transport within the proximal tubule. The model was subjected to perfusion under physiologic shear stress and pressure. However, additional studies that expand on the perfusion conditions and culture duration are necessary for more extensive characterization. Specifically, the extensive characterization needs to include evaluation of the cellular organization, tight junction formation, maintenance of barrier function, and selective transport as seen in vivo. We extensively characterized cells within our 2D model (chapter three); however, these protocols that exist in our lab need to be translated for the evaluation of 3D cellular structures.

In designing our 3D proximal tubule chip we hypothesized that microvascular beds will be formed between two larger vascular fluidic vessels and later connected to the vessels by angiogenic sprouting from the surface of the larger perfused vessels [16]. The sprouting and dense microvascular will enable communication between the vascular and renal networks through the permeable gelatin-fibrin ECM. Initially, we planned to use fluorescently labeled-Dextran permeability assay of varying molecular weights to test for molecular permeability. Following initial assessments, more rigorous validation of the 3D chip to replicate in-vivo tubular function can be accomplished via determination of time-dependent glucose transport, albumin reabsorption, and inulin clearance studies to assess the mass balance of the tissue chip. In vivo, hRPTECs reabsorb virtually all glucose from the glomerular filtrate by secondary active transport mechanisms; meanwhile, albumin and other low molecular weight proteins are reabsorbed through receptor-mediated endocytosis

[17]. The glucose concentration difference between vascular and PT perfusate can be measured with a commercially available glucometer to investigate glucose reabsorption. With existing vascular and proximal tubule tissue chip models, glucose reabsorption is estimated at 20% compared to 100% in a healthy kidney [18]. Fluorescently labeled human serum albumin from the media can be collected, stained for megalin expression, and quantified by flow cytometry. Furthermore, gene expression analysis of the isolated lysate of the PT in the presence of the capillary network can be evaluated to determine if there is an upregulation of sodium/glucose cotransporter 2 (SGLT2), the water transport channel, AQP1, and basal-lateral expression of $Na^+/K^+$ ATPase transporter compared to single cultured tubules without vascular networks. Adding inhibitors such as SGL2 inhibitors like empagliflozin and/or D-glucose in the media to 400 mg/dL (a four-fold increase) can be used to investigate the responsiveness of the proximal tubule transport of glucose [19]. In all potential studies, the glucose and albumin reabsorption efficiencies will be compared to in vivo studies (taking account of the tubule's length, diameter, and reabsorption) to establish physiological relevance.

Lastly, we must evaluate the model's capability to recreate physiologically relevant disease states. This can be accomplished in different ways, such as simulating renal tubular dysfunction or hypoxia. The effects of induced hyperglycemia can be evaluated via examination of both structural and functional changes to tubular and vascular structures. Using TEM, acute effects can be evaluated by characterizing epithelial and endothelial ultrastructure changes. Gene expression profiling and immunoblotting can measure VEGF, TGF-β1, SGLT2 transport, and augmented ECM protein deposition. Finally, hyperglycemia-induced endothelial and epithelial damage due to oxidative stress can be

measured through CellROX and nitrotyrosine fluorescence intensity and elevation in the pro-inflammatory cytokine production [18]. There are endless potential avenues for characterization, validation, and subsequent utilization of 3D proximal tubules and associated vascular tissue chips, and the specific directions will depend on the specific research question.

## 3. Discussion and Conclusions

This thesis explores and expands on the technological advancement of tissue chips and microphysiological systems with a special emphasis on cardiac tissue and the renal proximal tubule. Studies focused on cardiac tissue explored the effects of isolated pressure and stretch stimuli on engineered cardiac tissue. This study confirmed that short-term exposure to isolated pressure or stretch stimuli results in an acute response to the imposed stimuli; however, the responses appear similar regardless of the type of stimuli. A 2D renal proximal tubule model was developed to evaluate drug-induced nephrotoxicity under physiological shear conditions. Our results establish clear differences in the structure and function of renal proximal tubule epithelial cells cultured under static conditions and low and high shear conditions. More importantly, shear stimuli appear to be protective and alter the level of susceptibility of renal proximal tubule epithelial cells to different drugs. Finally, to create a model that more accurately mimics tubular and peritubular capillary networks, a 3D proximal tubule model and microvascular networks were successfully created.

Reference:


1. Paul, M.W.M.D., *Elixirs, Diluents, and the Passage of the 1938 Federal Food, Drug and Cosmetic Act.* Annals of Internal Medicine, 1995. **122**(6): p. 456-461.
2. Cavers, D.F., *The Food, Drug, and Cosmetic Act of 1938: Its Legislative History and Its Substantive Provisions.* Law and Contemporary Problems, 1939. **6**(1): p. 2-42.
3. Jackson, C.O., *Food and drug legislation in the New Deal*. 1970, Princeton, N.J.: Princeton University Press.
4. DiMasi, J.A., H.G. Grabowski, and R.W. Hansen, *Innovation in the pharmaceutical industry: New estimates of R&D costs.* J Health Econ, 2016. **47**: p. 20-33.
5. DiMasi, J.A., R.W. Hansen, and H.G. Grabowski, *The price of innovation: new estimates of drug development costs.* J Health Econ, 2003. **22**(2): p. 151-85.
6. Dickson, M. and J.P. Gagnon, *Key factors in the rising cost of new drug discovery and development.* Nat Rev Drug Discov, 2004. **3**(5): p. 417-29.
7. McGonigle, P. and B. Ruggeri, *Animal models of human disease: challenges in enabling translation.* Biochemical pharmacology, 2014. **87**(1): p. 162-171.
8. Ahmed, S., et al., *Pharmacogenomics of Drug Metabolizing Enzymes and Transporters: Relevance to Precision Medicine.* Genomics Proteomics Bioinformatics, 2016. **14**(5): p. 298-313.
9. *Chronic Kidney Disease Basics*. [
] February 28, 2022 [cited 2023; Available from: https://www.cdc.gov/kidneydisease/basics.html.
10. Kaiser, J. *NIH gets $2 billion boost in final 2019 spending bill*. 2018 [cited 2023; Available from: https://www.science.org/content/article/nih-gets-2-billion-boost-final-2019-spending-bill#:~:text=Congress%20has%20approved%20a%20%242,and%20Senate%20negotiators%20last%20night.v.
11. Han, J.J., *<scp>FDA</scp> Modernization Act 2.0 allows for alternatives to animal testing.* Artificial Organs, 2023.
12. S, N.N.C.f.A.o.T. *Tissue Chips*. 2018; Available from: https://ncats.nih.gov/tissuechip/about.
13. Fermini, B., et al., *A new perspective in the field of cardiac safety testing through the comprehensive in vitro proarrhythmia assay paradigm.* J. Biomol. Screen. Journal of Biomolecular Screening, 2016. **21**(1): p. 1-11.
14. Ingber, D.E., *From tensegrity to human organs-on-chips: implications for mechanobiology and mechanotherapeutics.* Biochemical Journal, 2023. **480**(4): p. 243-257.
15. Ewart, L., et al., *Navigating tissue chips from development to dissemination: A pharmaceutical industry perspective.* Exp Biol Med (Maywood), 2017. **242**(16): p. 1579-1585.
16. Lee, V.K., et al., *Generation of Multi-Scale Vascular Network System within 3D Hydrogel using 3D Bio-Printing Technology.* Cellular and molecular bioengineering, 2014. **7**(3): p. 460-472.
17. Koeppen, B.M. and B.A. Stanton, *Renal physiology.* 2019.

18. Lin, N.Y.C., et al., *Renal reabsorption in 3D vascularized proximal tubule models.* Proceedings of the National Academy of Sciences, 2019. **116**(12): p. 5399-5404.
19. Panchapakesan, U., et al., *Effects of SGLT2 inhibition in human kidney proximal tubular cells--renoprotection in diabetic nephropathy?* PLoS One, 2013. **8**(2): p. e54442.